UNIVERSITÀ DEGLI STUDI DI PADOVA

Department of Geoscience

Second Cycle Degree (MSc) in:
Geophysics for Natural Risks and Resources

GEOLOGICAL STRUCTURES EXTRACTION FROM SLOPE INSTABILITIES USING GB-SAR DATA

Supervisor:
Prof. Jacopo Boaga, PhD.
Co-Supervisor:
Alberto Michelini, IDS GeoRadar.

Submitted by:
Valentina Carmona Mongua

December, 2023

Abstract

Slope instabilities, whether occurring in natural or engineered slopes, are significant geo-hazards that carry substantial risks in terms of human safety, environmental impact, and economic costs. The relevance of studying this phenomenon has grown due to the influence of climate change, as increased rainfall patterns are expected to lead to a higher frequency of slope instability events. Also, in engineered scenarios such as open pit mines, the operative requirements have become stricter in recent years, focusing on the improvement of safety to decrease operational risks. Moreover, the use of remote sensing technology such as Ground Based Synthetic Aperture Radar (GB-SAR) has opened the possibility of monitoring in real-time, with very high resolution the deformation of the slopes, which provides the opportunity for timely decision-making in managing this hazard. Extracting geological structures from GB-SAR data can improve the geological and geotechnical characterization of the slopes, and can promptly provide an input to conduct a primary kinematic analysis for slope stability modeling. In this study, a semi-automatic algorithm was developed to detect geological structures from a velocity map obtained from GB-SAR data. This algorithm filters the 2D map and clusters the unstable area for posterior edge detection. Then, the extracted 3D edge serves as input for a newly developed 3D iterative plane-fitting algorithm which provides surfaces that are potentially related to the geological structures involved in the slope instability. The accuracy and effectiveness of this algorithm were tested in two cases of study with radar data provided by the company IDS GeoRadar. With this data, it was possible to compare the extracted planes with planes modeled using photogrammetry and to establish the limitations and some of the requirements to use this algorithm, such as a proper resolution of the Digital Terrain Model (DTM) and an accurate geocoding.

Keywords: *GB-SAR, plane-fitting, failure surfaces, slope, stability, semi-automatic.*

Acknowledgements

To do this project has been an effort that not only has involved its writer. Without the support and guidance of many people, this would have not been possible. Some actions were directly related to this thesis and others provided emotional reassurance. I want to give special thanks to Alberto Michelini who was a great co-supervisor and with his patience and time guided me on a topic that I knew nothing about, and also to the company IDS GeoRadar for providing the data and the time availability of Alberto. To Professor Boaga, who was always willing to help me and teach me even beyond his official responsibilities. To Professor Cassiani, who encouraged me to do this thesis and during classes shared all his knowledge and was patient with all my questions.

Finally, to my family and friends, they know what this means to me. Thank you.

Contents

1 Introduction

Slopes, whether natural or engineered, experience shear stress due to the force of gravity, and in unstable conditions this might lead to the movement of a mass of rock, soil, or a combination of material down-slope resulting in a failure event. This process is a consequence of two possible conditions: the increase in shear stress and the reduction of the material shear strength (Varnes 1978). These two factors can occur independently and simultaneously, and depend on the geological structures of the slope since they usually control its stability, the failure mechanism, and the hydro-geological conditions from the micro to the macro scale (Stead and Wolter 2015). Thus, it is of great relevance to characterize in detail the structures that are or may be associated with the slope instability. In the case of engineered slopes, the study of the geological structures should be part of the multiple stages of the development of the project such as the design, operation, and post-operation, since the human intervention itself modifies the stress field of a slope and hence it modifies the role of the present structures on its stability.

This geological phenomenon is a very relevant hazard since according to the report presented by the Centre for Research on the Epidemiology of Disasters (CRED) "*2022 Disaster on numbers*", during this year 403 deaths were caused by landslides, casualties which most of them could have been prevented with an appropriate risk assessment. Besides, on the data gathered by CRED (2023b) in the EM-DAT database, during the last ten years (2013-2023), natural slope instabilities have represented 4.72% of the total number of natural disaster events. In some regions of the world, this percentage is likely to increase in the future due to climate change. As mentioned in Jakob (2022) this is a complex relation that has to be studied thoroughly since it depends on many variables such as the type of slope instability, altitude, latitude, precipitation rates variability, etc. Nevertheless, it can be asserted that regions in high latitudes and high altitudes will be more prone to the increase in the frequency of slope failure events with climate change, being attributable to glacier retreat and other special conditions of these areas. Also, tropical and mountainous regions will be affected by high-intensity rainfalls which is one of the main triggers of slope instabilities. Because of the concern regarding the adaptability of the affected regions to climate change and landslides, the Sendai Partnerships 2015-2025 for Global Promotion of Understanding and

Reducing Landslide Disaster Risk was established . One of the areas of collaboration within this partnership involves the development of improved technologies for monitoring, testing, analyzing, and simulating slope instabilities, and the creation of effective early warning systems for this phenomenon.

Regarding engineered slopes, as mentioned above, during the excavation of rock or soil the vertical and horizontal stresses are modified, which might cause the opening of cracks and joints increasing the risk of a slope failure (Altiti, Alrawashdeh, and Alnawafleh 2021). Particularly, in the case of open pit mines, this hazard has the potential for economic losses ranging from millions to ten million dollars per site per year, including the costs of cleaning, disrupting the mining operations, damages to the equipment, and the abandonment of material due to the difficulties in remediation (Young, Robotham, and Virk 2020). Moreover, the main motivation to mitigate the slope instabilities is the protection of the workers, since according to the Mine Health and Safety Inspectorate of South Africa (2018) slope failures are one the main causes of accidents in open-pit mines. Additionally, as the world population increases and the energy transition demands more production of raw minerals, about 17% of the existing open-pit mines will become deeper, reaching more than 1000 m of depth. This large increase in depth creates a complex scenario regarding the slope stability of the rock mass, because of the variability of the mechanical properties of the rocks with depth (Rimmelin and Vallejos 2020). Thus, considering the current state of the world development model regarding climate change, energy transition, and world population, the study of slope instabilities is currently a very relevant field for both natural and engineered slopes.

One of the main techniques to analyze slope instabilities is the application of remote sensing methods, which allow safe conditions for the characterization of this hazard. Currently, there is a wide diversity of options for remote sensing techniques with different applications according to multiple parameters such as their spatial and temporal resolution, spatial coverage, operative distance, etc (Casagli et al. 2023). The Ground Based Synthetic Aperture Radar (GB-SAR) is a relatively new technique that emits electromagnetic waves in the microwave spectrum to detect the deformation of a slope with sub-millimeter sensitivity and a practical operative range since it is possible to take measurements some kilometers away from the target surface. It provides information about the rate and distribution of surface

displacement, which makes it a very useful tool for early warning and monitoring of slope instabilities. GB-SAR can be used in many scenarios and it is especially useful in complex weather conditions when other remote sensing techniques would not be able to perform a reliable measurement. However, the usage of the GB-SAR data to extract information about the geological structures involved in the deformation is limited, and it usually refers to the satellite-based SAR counterpart (Roccheggiani et al. 2018;Libert, Wuite, and Nagler 2022). Therefore, in this study, a data processing algorithm is proposed to extract the geological structures involved in the deformation of a slope using this remote sensing technique. These extracted planes are useful to improve the slope characterization during the risk analysis stage, and they could be used to do estimations about the volume of material involved in a potential failure event. They also have great potential to be used as input for the kinematic and stability analysis of the slope. All of this allows a prompt response to this hazard and therefore this algorithm could optimize the mitigation plans for this geological risk.

2 Generalities of slope instabilities studies

2.1 Risk management

As previously mentioned, a slope instability is a geological hazard that has the potential to cause minor or severe damages. Therefore, it is important to give a risk definition in this context. In general, risk is defined as the combination of hazard, vulnerability, and exposure:

$$Risk = hazard \times vulnerability \times exposure \tag{1}$$

According to the definitions given by Glade, Anderson, and Crozier (2005), hazard refers to a physical condition that has the potential to cause damage. It is defined according to its probability of occurrence and expected magnitude within a given time-frame. The interplay between frequency and magnitude is particularly relevant since smaller-scale events tend to occur more frequently. Furthermore, vulnerability is understood as the expected level of damage caused by an event of a certain magnitude and it depends on the human conditions and how these interact with the hazard and how they react to an event. An example of this is provided by Glade (2003) and it relates the level of damage of a mass movement with the probability of the presence of people during different times of the day. Meanwhile, exposure relates the level of damage with the expected losses for a given event. It considers elements in different classifications such as the number of human lives at risk, the damage to the infrastructure, the potential direct or derived economic losses, the effects on the environment, and the mental health of the affected people, etc, including quantifiable and unquantifiable effects.

Following the framework established by the Australian Geomechanics Society (2002), the definition of risk given above would be part of the risks analysis stage of the risk management process, summarized in Figure 1. In this case, the term *landslide* can be interchangeable with the term *slope failure*, however, these terminologies must be used with caution. According to this flow chart, the management of a slope instability hazard comprises analysis and studies in several areas besides the geology-related fields, such as the economic and social aspects affected by this phenomenon. However, in this study, only the geological conditions of the

risk management will be considered. In this regard, slope instability studies have three main stages, detection, monitoring, and hazard prediction (Casagli et al. 2023; Metternicht, Hurni, and Gogu 2005).

During the detection stage, the goal is to characterize the physical features of an area such as the geological, geotechnical, hydrological parameters, etc., that allow the identification of active or inactive slope instabilities or the potential of an area to become one. In terms of management, this corresponds to the risk analysis stage, where the magnitude and the likelihood of the slope failure are defined during the hazard identification according to its physical conditions (Macciotta and Hendry 2021). The magnitude is associated with the volume of the material that would be potentially involved in the failure, while the likelihood depends on the stability conditions of the slope.

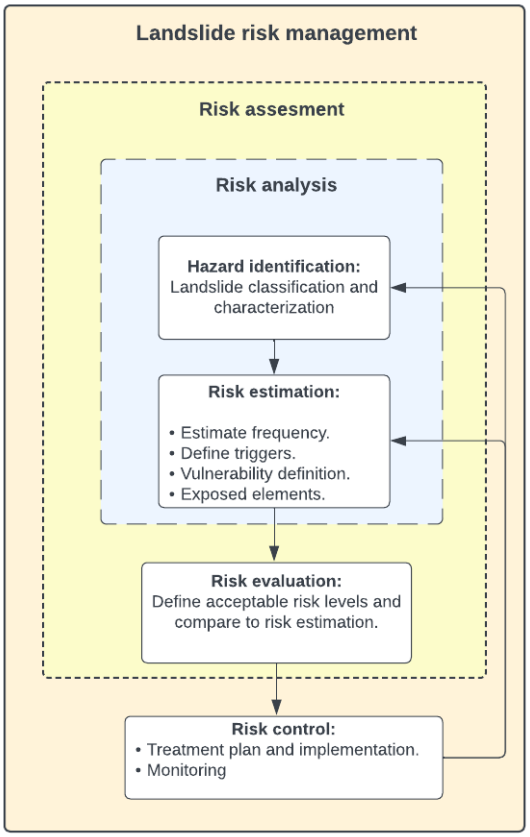

Figure 1: Stages of landslide risk management. Summarized and modified from Australian Geomechanics Society (2002).

After detecting and characterizing the slope instability, it is necessary to monitor its behavior

including the velocity and magnitude of deformation. Considering the framework of risk management (Figure 1) the monitoring stage is required in the risk control step, but it also gives additional information about the physical conditions of the slope instability, and therefore it provides feedback to the risk analysis, making these process an iterative analysis. In this stage, it is very important to use adequate spatial and temporal resolutions to monitor accurately the kinematic behavior of the hazard. Lastly, prediction is part of the risk control step and during this stage, the parameters that are involved in the slope failure, that were estimated and correlated in the risk analysis step, such as the pore pressure, the rainfall rates, and the velocity of displacement, can be used as input for an alarm or monitoring system, to forecast failure events and therefore reducing the vulnerability of the studied area.

The methods to develop each stage are chosen, according to the particularities of a given area, considering multiple factors like the required temporal resolution, the scale of the slope instability, and the general risk related to it. For example, the methods required for a slope in an open-pit mine, where workers and machinery are present, are different from the ones required in a large-scale landslide in a remote area. Considering the scale of the slope instability, multiple techniques can be chosen according to their type of acquisition. In this regard, from the available methods, two main branches can be identified, the ones that require in-situ tests and the remote sensing techniques. Evidently, the main difference between these two is the need for direct contact with the slope, however, another important distinction is the spatial coverage.

In-situ methods cannot cover a large area, and are usually limited to local-scale studies, since they are usually based on point-to-point measurements, such as boreholes and penetration tests, or have a complex acquisition like some of the geophysical methods. In contrast, remote sensing methods have the advantages of covering larger areas, ensuring safe conditions in high-risk instabilities, and facilitating the acquisition in inaccessible areas. However, in any slope instability study, both types of methods are required to have a complete and accurate characterization of the hazard. Thus, these two types of techniques should be integrated into the three stages of the study of slope instability risk analysis and must be considered as complementary independently of the scale of the area and the temporal resolution required.

2.2 Geological structures in slope instabilities

The term *geological structure* is a broad term related to the three-dimensional arrangement of geological materials on the earth's crust. The diversity of the geological process also produces diverse types of geological structures, some related to the tectonic setting such as faults and folds, others to the sedimentary nature of a rock like the bedding planes, or to metamorphic processes as the foliation. However, in this study, this term is rigorously used to describe the planes related to the failure or potential failure surface in a slope instability. This distinction is relevant since, depending on the mechanical properties of the material, a slope movement can have strong or weak structural control, related to the geological processes and structures mentioned above. To distinguish between these two usages of this term, and as suggested by Wyllie and Mah (2004), the structures related to the "naturally occurring breaks" which are studied in structural geology such as the ones mentioned (faults, fold, bedding, joints, etc.) will be referred to as *discontinuities*, while the planes related to the failure surface (or potential surface) are the *geological structures* that will be referred to in the proposed methodology. Thus, the aim of this study is to extract the structures that provide the lateral surfaces present in a slope instability, that may or may not be caused by discontinuities.

The slope movements caused by the presence of discontinuities are referred to as structurally controlled slope instabilities. The degree of structural control is one of the many parameters that are used to classify the slope instabilities (Smith and Hungr, 1992 as cited in Glastonbury 2002) and their failure mechanisms (Norrish and Wyllie 1996;Wyllie and Mah 2004). Nevertheless, there are many other classification parameters such as the type of material, kinematic behavior, and state of activity. Hence, many classification schemes have been proposed for this geological process, some of them are summarized in Glastonbury (2002). One of the most widely used is the one proposed by Varnes (1958) and updated in Cruden and Varnes (1996). In this last classification two types of materials are defined, *rock* as the "hard or firm mass that was intact and in its natural place before the initiation of movement", and *soil* as an aggregate of particles that have been transported or formed by rock weathering. From these two types of material, five types of movement are classified: fall, topple, slide, spread, and flow. There is also an additional category, the complex slope movements which include a combination of the kinematic behaviours mentioned.

In engineering, one of the most relevant classifications is one done according to the failure modes or mechanisms (Nichol, Shaker, and Wong 2006;Wyllie and Mah 2004;Mercer 2006). In this classification, there are four failure modes: planar, wedge, topple, and circular (Figure 2). These, are related to the degree of structural control as follows:

- Planar failures: These are caused by a single discontinuity dipping towards the slope causing a single failure plane.
- Wedge failures: In this case, two discontinuity planes cross in an intersection dipping out of the slope face, causing the sliding of a block.
- Topple failure: Involves a group of discontinuities that dip vertically with a moderate to close distance causing an arrangement of unstable slabs or columns.
- Circular failure: This failure mode occurs in soil masses and in highly fractured or weathered rock, or when the face of the slope has a high dip angle. It is not necessarily related to discontinuities.

This classification can be correlated to the classification made by Cruden and Varnes (1996) since the planar, wedge, and circular failure mechanisms are enclosed in the *slide* category. Planar and wedge failures are classified as translational slides, while the circular failure mode is considered a rotational slide. The topple failure mechanism has the same nomenclature in Cruden and Varnes (1996) classification.

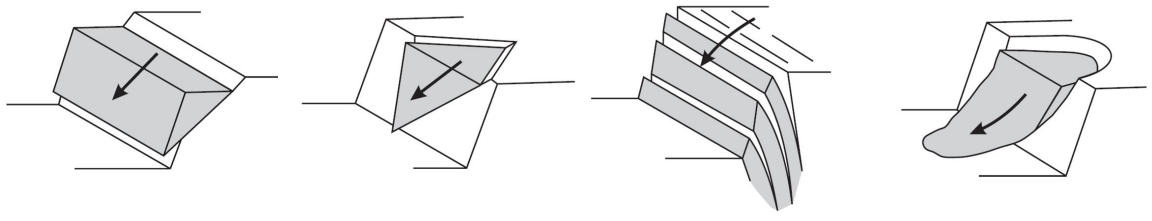

(a) (b) (c) (d)

Figure 2: Failure mechanisms. (a) Planar, (b) Wedge, (c) Topple, and (d) Circular. Taken from Wyllie and Mah (2004).

The accurate classification of a slope movement is very relevant since the selection of the methods for the stability analysis depends on the failure mechanisms involved in the defor-

mation. For instance, for a planar failure, the infinite slope analysis can be used, while in the case of circular failures, the circular arc method is suggested (Abramson et al. 2001). As stated in Piteau and Peckover (1978), to perform the stability analysis, it is necessary to test the planes or combination of planes that would be related to the failure surface. A simple example of this is the wedge failure mechanism, in which the location and orientation of five bounding surfaces are required in the stability analysis (Norrish and Wyllie 1996). Also, in the case of using the infinite slope method, where the slip surface is parallel to the ground surface, the boundaries extracted from the deformation would be directly related to the volume of the moving mass, if the depth is known. Therefore, the early extraction of the planes involved in a slope movement would be very useful to perform early estimations about its stability.

Besides being useful for the stability analysis, the planes given by the lateral margins have been used to extract information about the depth, volume, and kinematics of a slope instability (Jaboyedoff et al. 2020; Dewitte and Demoulin 2005;Hu et al. 2020; Bunn, Leshchinsky, and Olsen 2020; Nikolaeva et al. 2014). Also, not only the planes related to the failure are useful for characterizing the deformation, but the superficial extent and geometry of the unstable area have been used to estimate the classification of the slope movement (Parise and Jibson 2000) and even to obtain information about the mobility of the instability (Tian et al. 2017).

In summary, the geometrical description of the planes involved in the slope movement is of great relevance in its characterization, being an input for the slope stability analysis, volume estimation, and kinematic description, and therefore an input for the risk mitigation strategies. As stated in Martha et al. (2010) " A comprehensive characterization [of a slope movement] from an automatic detection perspective is required for the extraction of fast and accurate results that will help decision-makers in implementing disaster management strategies". Additionally, the early extraction of the geological structures involved in the deformation would provide valuable information to decide the location and depth of other investigation techniques such as boreholes, geophysical surveys, or other in-situ measurements, representing a cost reduction in further slope instability studies.

2.3 Remote sensing in slope instabilities

Remote sensing techniques are used in the three stages of slope instability studies, detection, monitoring, and prediction (Metternicht, Hurni, and Gogu 2005; Casagli et al. 2023) and are fundamental for the characterization and mitigation of this geological risk. These techniques can also be divided into three main types according to their acquisition, as airborne, satellite-based, or ground-based, and each of them has a range of operability, which according to Casagli et al. (2023) is described with six parameters: the spatial resolution, spatial coverage, operative range, temporal resolution, accuracy and range of velocity detection. Of the three main types of techniques, the satellite acquisitions are the ones with the largest spatial coverage, with footprints from 10s of kilometers to about 300 kilometers, while the ground-based methods can only reach up to 10 squared kilometers (Casagli et al. 2023). It is relevant to mention that selecting the optimal method requires a careful consideration of the trade-off between coverage and resolution, considering that a larger coverage would result in a lower spatial resolution. However, with recent developments, it is becoming more common to improve this trade-off, by increasing the spatial resolution of the measurement even in a large area of acquisition using satellites with sub-meter resolution (WorldView, QuickBird, IKONOS, GeoEye, SPOT, etc.), and also processing the images to improve their resolution (Mei et al. 2020).

Regarding the temporal resolution, it has a large variation between methods, as the acquisition frequency, in the same area, can vary from several days (satellite-based) to a few minutes (ground-based). The requirement of the temporal resolution is dependent on the velocity of the deformation of the slope instability; if the displacement is very fast a method with a high temporal resolution is required to track properly the kinematic behavior of the deformation, while during a slow deformation, a method with larger periods of acquisition is able to characterize the displacement. Choosing a proper method according to this parameter is a very important task, especially during the monitoring and prediction stages, because the velocity of deformation can vary between orders of magnitude, as classified by Cruden and Varnes (1996) from extremely slow ($0.5 \times 10^{-6}\,\mathrm{mm\,s^{-1}}$) to extremely rapid movements ($5 \times 10^{3}\,\mathrm{mm\,s^{-1}}$). Also, it is relevant to consider that this velocity can vary during the development of the slope movement, which can have a quasi-stable condition with minor

displacements that can occur during years or centuries without failure, or it can develop as a minor displacement followed by a rapid acceleration preceding the failure (Wyllie and Mah 2004). Therefore, multiple techniques could be used in the same area during different stages of the slope instability evolution.

Another important distinction between the remote sensing techniques is the type of acquisition, which can be passive or active. All remote sensing techniques are based on the use of electromagnetic (EM) waves for the detection of multiple characteristics of the observed phenomenon, in the passive methods the instrument works only as a receiver of the EM signal, while the active techniques work as a transmitter and receiver of EM waves. Passive methods can include optical and thermal cameras and optical satellites; these can be used in photogrammetry when they work in the visible range of the EM spectrum and in radiometry when they work in the entire optical radiation spectrum. The main drawback of these methods is the attenuation caused by the interaction with the atmosphere since clouds and rain can attenuate or entirely obscure the signal (Long and Ulaby 2015). This can be very inconvenient in the case of slope instability studies since the high precipitation rate is one of the main triggers for this geological hazard. Passive methods are mostly used for landslide inventorying, detection and mapping, and change detection (Casagli et al. 2023;Tofani et al. 2013)

Moreover, the active methods can be classified according to the frequency range of the EM wave that is being transmitted. In the case of slope instability studies, two main sensors are used (Metternicht, Hurni, and Gogu 2005), the microwave radar sensors which work in the range of 0.3 GHz to 300 GHz, and the light sensors (LiDAR) which use higher frequencies in the visible range (4.3×10^{14} Hz - 7.5×10^{14} Hz) and near-infrared range (214 THz - 400 THz). In general, these two types of sensors can be used in all the acquisition types (satellite-, air-,ground-based), however, for slope instability studies radar sensors are usually used in satellite and ground-based acquisitions, while LiDAR techniques are usually set on air and ground-based surveys. Since LiDAR works in higher frequencies, this method has a higher spatial resolution than the radar methods, but it also makes it more susceptible to atmosphere attenuation, therefore it has a lower operative distance than radar methods and is less effective in complex weather conditions (Casagli et al. (2023)).

In remote sensing, radar sensors are used in multiple types of studies, and they are classified into different categories such as non-imaging radar, for instance, the scatterometers and altimeters, and imaging radars like GB-SAR (Long and Ulaby 2015).

3 GB-SAR principles

GB-SAR is an active remote sensing technique that emits electromagnetic waves in the microwave frequency range and uses an imaging radar. In general, a radar sensor can be classified according to the type of imaging formation method, which can use an antenna with a real aperture or a synthetic aperture. The antenna is the device that converts a guided wave propagating through a transmission line to an EM wave propagating through the free space and conversely (Long and Ulaby 2015). Hence, an antenna works as a transmitter and receiver of EM waves. When working as a receiver, the antenna converts the energy of an incident signal from power density ($\mathrm{W\,m^{-2}}$) to intercepted power (W), the ratio of this conversion gives the concept of *effective aperture*. In the case of Real Aperture Radars (RAR) the effective aperture is directly related to the physical aperture of the antenna. During transmission, a wider physical aperture would represent a narrower beam that illuminates a smaller area on the ground (target), this concentration of energy would increase the power density that, when it gets backscattered, increases the power during the reception. Therefore, the physical aperture of the antenna determines the quality of the measured data (Long and Ulaby 2015). For the Synthetic Aperture Radars (SAR), the size of the effective aperture is not dependent on the physical aperture of the antenna, instead, a longer aperture is synthesized by moving the sensor along a path, in the case of ground-based systems along a rail (for linear scanning mode) or a rotating arm (for ArcSAR). Then, it records a signal for each position of the antenna, processing them to combine them as if they were simultaneously collected, generating a high-resolution radar image.

The signal that is backscattered from the illuminated area depends on the physical properties of the target such as roughness and geometry, and on the electrical properties of its material (i.e. permittivity) since EM waves penetrate on its volume. As mentioned in Rödelsperger (2011), the typical bands used in SAR acquisitions are between the L-band to the K_u-

band. However, the newest GB-SAR devices can also work in the K, K_a, V, and W bands, which improves the accuracy of measurement by being able to detect the sub-millimetre deformation of a mass movement. Additionally, thanks to the use of these wavelengths, the atmosphere attenuation is minimal, and as a result, GB-SAR can be used even in adverse weather. This also means that the sensor can be placed at a large distance from the measured surface, reaching some kilometers of operative range. Furthermore, as it does not depend on the visible spectrum it can provide measurements in every light condition.

Band name	**Wavelength (cm)**	**Frequency (GHz)**
L	15 – 30	2 – 1
S	7.5 – 15	4 – 2
C	3.7 – 7.5	8 – 4
X	2.5 – 3.75	12 – 8
K_u	1.67 – 2.5	18 – 12
K	1.11 – 1.67	27 – 18
K_a	0.75 – 1.11	40 – 27
V	0.4 – 0.75	75 – 40
W	0.27 – 0.4	110 – 75

Table 1: microwaves bands used in SAR. Taken from Bruder et al. (2003).

In general, radar data acquisition can work in different ways according to the type of signal emitted. A way to understand the general radar functioning is by first explaining how the Pulse Radar works. This type of radar transmits a signal with a time duration τ, then stops and receives the return signal during the intervals between pulses. For a point target, the received signal is the same as the emitted one with a time delay that depends on its distance from the sensor. However, if there are multiple targets and they are too close together, or if the target is very complex, the time between pulses would not be enough to resolve the different time delays of their responses, as shown in Figure 3. Here, a pulse of length τ is emitted, and then it is reflected by target 1 and target 2 producing the signals $S1$ and $S2$. Depending on the separation of the targets, the received signal can be resolved or not, in example (b) the targets have a small separation that does not allow to distinguish the signals backscattered by each target. Consequently, when the acquisition is done using Pulse Radars, the resolution in the direction of the emitted EM signal depends on the length of the pulse τ.

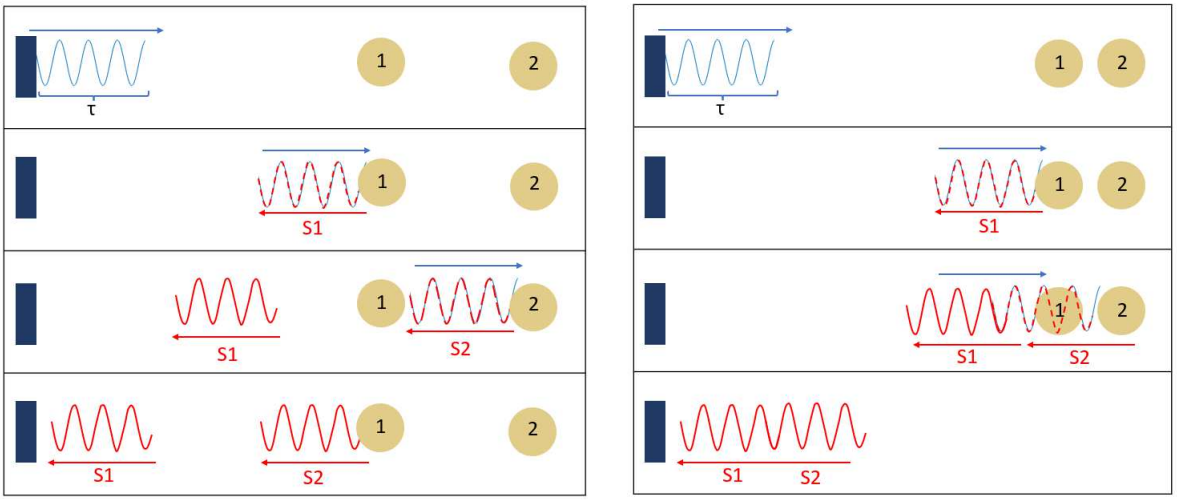

Figure 3: Pluse radar scheme. Response of a pulse with length τ of two targets with a large distance (a) and close together (b).

This resolution can be improved by reducing τ, this way the targets that are close together can be resolved. However, this means that less energy would be transmitted in a shorter signal, thus it would decrease the signal-to-noise ratio (SNR), decreasing also the radar capability to measure at long distances. Therefore, in SAR measurements, a continuous wave (CW) with no time intervals is used, this allows to have a high-energy signal with a better SNR. However, since there is no time interval between pulses it is not possible to distinguish the signal of each target. Because of this, a frequency-modulated continuous wave (FMCW) is used, where the frequency varies in time within a certain bandwidth (B). A filter is derived from the waveform of the echo of this transmitted signal, which is applied to the received one, increasing the SNR and resolving the reflections of each target (Long and Ulaby 2015).

For the newest GB-SAR instruments, the frequency modulation used is linear (LFMCW) as a function of time in a bandwidth B over a sweep period of time T as shown in Figure 4a. The central frequency of B is called the carrier frequency (f_c) and it is the one used to describe the system. The shape in terms of the amplitude of the transmitted and received waves would be similar to the representation in Figure 4b. Being the received signal an attenuated copy of the emitted one, with added noise and a time-delay.

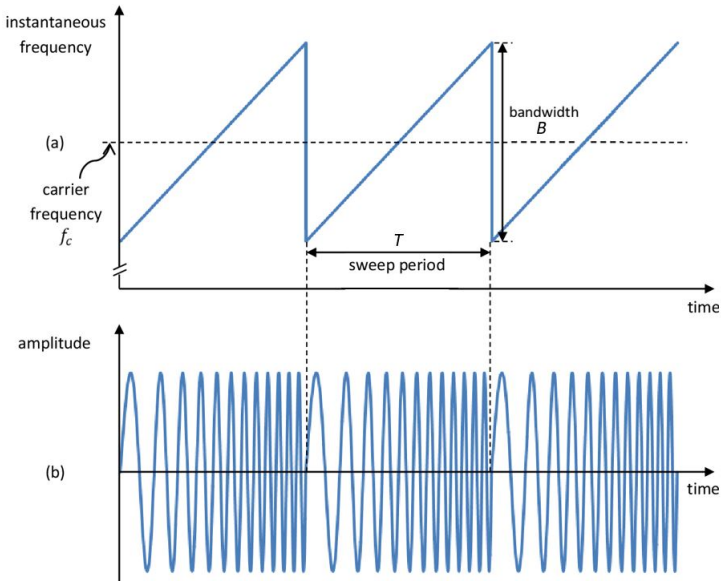

Figure 4: Scheme of linear frequency modulation. (a) Time-frequency plot and (b) time-amplitude plot. Modified from Peek (2011).

The resolution of the system depends on both the frequency modulation and the length of the synthetic aperture. As the two conditions work in different directions, two resolutions are derived. One is related to the horizontal movement that generates the synthetic aperture of the radar, and the other is related to the bandwidth used in the frequency modulation. The direction in which the FM signal is emitted and received is defined as the *Line of Sight* (LOS), and the distance in this direction from the sensor to the target is called the *range* distance (r) (Figure 5). The configuration of the system is done in such a way, that the LOS is as parallel as possible to the deformation vector of the target surface. This way, the values of displacement registered in this direction would be as close as possible to the real deformation. However, this setting is not usually feasible, and as a result, the measurement is limited to a component of the deformation vector (Figure 5). Along the LOS direction, the *range resolution* (δ_r) determines the minimum spatial dimension from which displacement can be detected. The range resolution cell on the LOS direction does not correspond to an equal dimension on the ground, since this cell must be projected on the surface, and depending on the topography it will correspond to a ground range resolution cell as shown in Figure 7. The range resolution depends on the bandwidth used in the frequency modulation and the velocity of the EM wave (c) as shown in the following equation:

$$\delta_r = \frac{c}{2B} \tag{2}$$

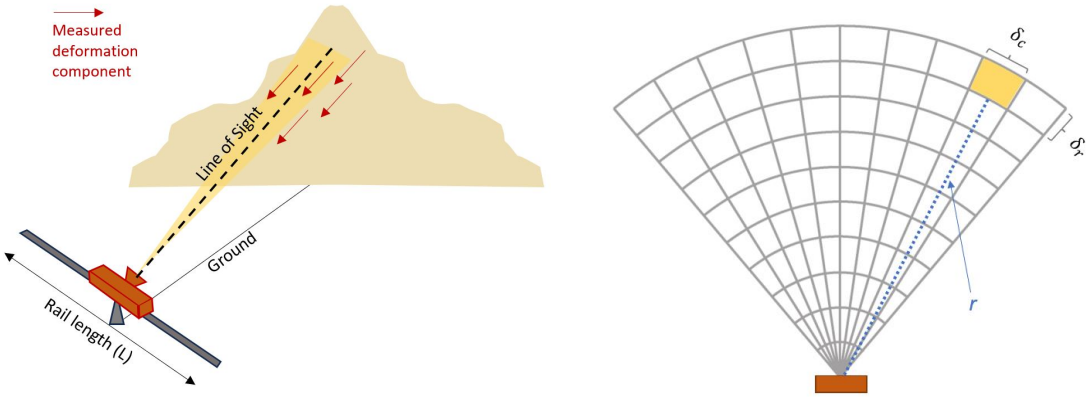

(a) (b)

Figure 5: Scheme of GB-SAR acquisition. System scheme (a) and resolutions grid (b).

The horizontal movement of the sensor on a path of length L, that generates the synthetic aperture, will give a second dimension to the radar measurement, and thus a second resolution, the *azimuth resolution* (δ_φ), which is given in the perpendicular direction to δ_r. Considering a single target on the surface, the emitted beam will overlap on the same point for every position on L, thus a different phase value is recorded on every step. The phase variation will depend on λ since it determines how fast the phase varies while the sensor changes its position on L. This relation between the phase variation and the displacement on the sensor path determines the azimuth resolution as follows:

$$\delta_\varphi = \frac{\lambda}{2L} \tag{3}$$

This expression is given in degrees, but it can also be expressed as a distance considering that the range distance (r) will change for every position on L, for a single target. Thus, δ_a can also be named as *cross-range* resolution (δ_c) given in units of distance as follows:

$$\delta_c = \frac{\lambda}{2L} r \tag{4}$$

These resolutions define both ground- and satellite-based systems. Some of the differences between these methods are, as mentioned before, the acquisition frequency which in satellite-based systems can take several days while in Ground-based (GB-SAR) it takes a few minutes. Also, in GB-SAR the rail or the rotating arm, that gives the synthetic aperture path remains in the same location for every acquisition, while the relative position of a satellite to a single target can vary depending on the orbit. The differences in time and position between acquisitions are referenced as *temporal baseline* and *spatial baseline*, the latter is usually zero in the case of GB-SAR.

In GB-SAR, for all the positions on the rail, a single target will backscatter all the frequencies contained in the bandwidth and multiple targets will have different time-delays and amplitudes. Thus, a raw radar image is registered in these two dimensions, frequency and position on L. To translate this to spatial dimensions, the radar image must be "focused". This *focusing* process applies a Fourier transform on each dimension, converting the image to the range and azimuth directions, being the azimuth the angle from the center of the rail. Lastly, the range and azimuth resolution values are used to do the conversion to planar x and y coordinates from the location of the radar sensor, as shown in Figure 6.

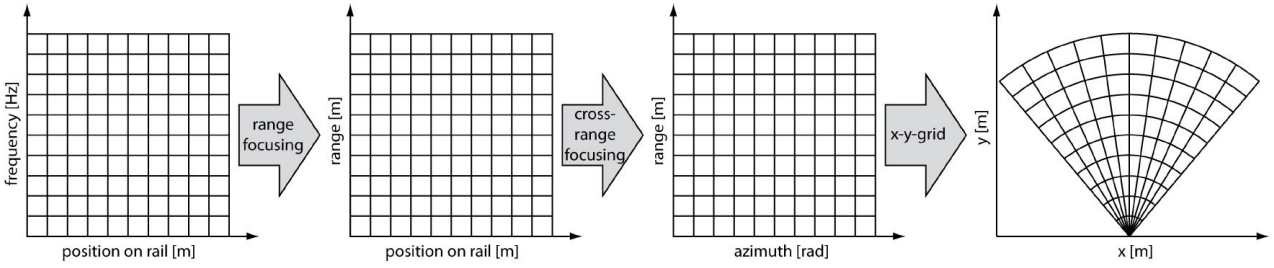

Figure 6: Focusing process. Taken from Rödelsperger (2011).

Each radar pixel will store a complex value with the amplitude and phase information of the received signal and will have a resolution given by δ_r and δ_c. One of the limitations of GB-SAR is that the geometry of the measured area is not truly represented in the final radar image. This happens because the true ground resolution is the projection of the range resolution on the surface, and depending on the angle between the LOS and the surface, the ground features can be overlayed or shadowed. Overlaying happens when two surfaces at different heights but at the same range distance (r) get recorded in the same pixel, and shadowing when the angle between the surface and the LOS is such, that no signal gets

backscattered by the surface. As exemplified by Rödelsperger (2011) in the following figure:

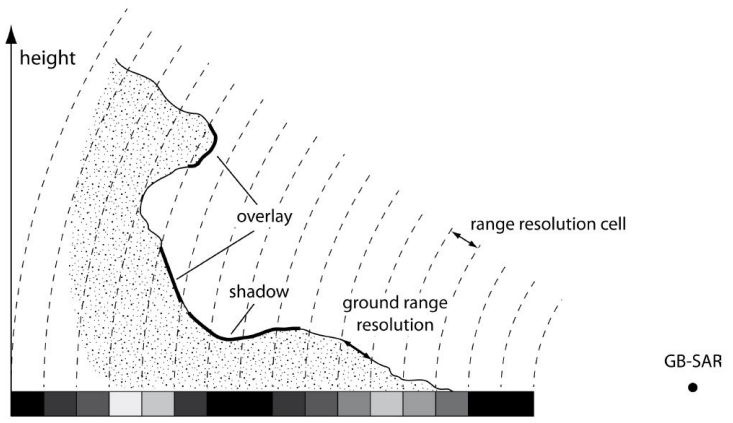

Figure 7: Overlaying and shadowing. Taken from Rödelsperger (2011). The row pixels at the bottom in grayscale exemplify the intensity response of the sensor.

Regarding the phase measurement, as it is derived from the time-delay received signal, it gives information on the range distance (r), following equation 5. However, the phase value is affected by a random term (ϕ_{ran}) which is related to the scattering characteristics of a distributed target. Because of this term, is it not possible to compute the distance information from a single radar image. But, one advantage is that this term remains constant between acquisitions, therefore by subtracting two radar images from different acquisition times, this term can be canceled. This process is called *interferometry* and gives the phase difference between two acquisitions, thus it can provide the distance variations which in other words would be the deformation that occurred between two acquisition times.

$$\phi = -\frac{4\pi}{\lambda} r + \phi_{ran} \tag{5}$$

The phase difference between two acquisitions is calculated by using the conjugate of the complex measurements of each radar image as follows:

$$z_1 z_2^* = a_1 a_2 \cdot e^{i(\phi_1 - \phi_2)} \tag{6}$$

Where z_1 and z_2 are the complex values of each radar pixel on acquisition times 1 and 2, containing the amplitudes a_1 and a_2, and the phase values ϕ_1 and ϕ_2. In equation 6 the

subtraction between phases gives the wrapped differential phase ($\Delta\phi_w$). The term "wrapped" is used since this value is limited to the interval of $[-\pi, \pi)$ which means that different values of r can generate the same measured phase value but in different wave cycles (n). The wrapped differential phase is related to the real differential phase value ($\Delta\phi$) as:

$$\Delta\phi_w = \Delta\phi - 2\pi n \tag{7}$$

Using $\Delta\phi_w$ the information about the relative changes between two acquisitions can be extracted. However, the interferometric phase value is not only affected by changes in the range distance (i.e. surface displacement), other temporal and spatial changes between the two acquisitions can affect its value, causing temporal and spatial decorrelation between two radar images. The contributions to the interferometric phase values are given by:

$$\Delta\phi_w = \Delta\phi_{topo} + \Delta\phi_{disp} + \Delta\phi_{atm} + \Delta\phi_{noise} - 2\pi n \tag{8}$$

The topography phase component is related to the changes in the position of the sensor and, as mentioned previously, in GB-SAR the spatial baseline is usually zero, hence this component is not considered. The displacement component is the target value of this process since it contains the surface deformation measurement, however, it is masked by the contribution of the atmosphere changes between acquisitions and the recorded noise. Radar measurements are not as strongly affected by the atmosphere as other remote sensing methods, however, microwaves do interact with the atmosphere depending on the humidity, temperature, and pressure, which affect the refractive index of the propagation medium. Thus, to extract the displacement component the following expression must be computed:

$$\Delta\phi_{disp} = \Delta\phi_w - \Delta\phi_{atm} - \Delta\phi_{noise} + 2\pi n \tag{9}$$

The integer number related to the wave cycles n must be calculated in order to find the continuous differential phase measurement and not only the values contained in the wrapped interval, this process is called *unwrapping*, and it is based on complex algorithms that will

not be addressed. The atmosphere contribution is corrected using a diverse number of atmospheric-phase correction algorithms (Chao et al. 2019). Currently, one of the most used methods is based on Permanent Scatterers (PS) which are targets on the surveyed surface that are relatively stable, meaning that between a number of acquisitions, they will be located in the same relative position from the sensor. Therefore, the pixels that record the back-scattered signal of the PS do not have a strong variation in their amplitude or phase value, which means a high spatial and temporal coherence. Using these stable pixels, the changes in the measurements that are not related to the deformation can be identified and corrected.

After unwrapping and phase correction, the real component of the interferometric phase related to the displacement is extracted. The final deformation in the direction of the LOS (ΔR) is given by:

$$\Delta R = -\frac{\lambda \, \Delta\phi_{disp}}{4\pi} \tag{10}$$

As summarized by Rödelsperger (2011), the processing for both satellite-based SAR and GB-SAR is very similar, and it is based on the steps explained above and shown in the following figure:

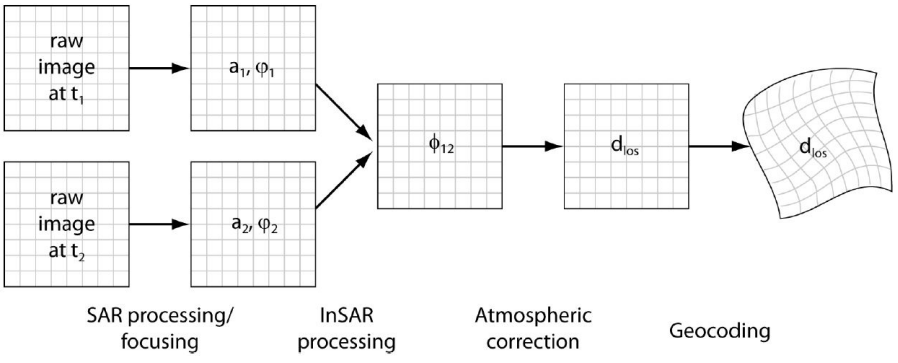

Figure 8: General steps for SAR processing. Taken from Rödelsperger (2011)

In Figure 8 the main processing steps are consolidated. Starting from the raw radar images in different acquisition times t_1 and t_2, these are focused to convert them to spatial coordinates. Then, the differential phase between acquisition is extracted during Interferometry, this

process is usually referred to as *InSAR* processing or *DInSAR* processing. Later, unwrapping, and atmospheric correction are performed to derive the displacement phase component in the direction of the LOS. Using equation (10) the deformation during the time interval of the two acquisitions is calculated. However, this result is still in 2D coordinates, and as mentioned previously the resolution of the radar cell is not true ground resolution, as shown in Figure 7. Thus, using a Digital Terrain Model (DTM), the 2D image can be projected to the real coordinates of the 3D space in a process called *Geocoding*, which relates the radar pixels to the DTM cells. This process will be explained in the methodology chapter (4).

3.1 Automatic extraction of structures using inSAR and other remote sensing techniques

As mentioned in chapter 2.2, having information about the geological structures and discontinuities that are involved in a mass movement is essential to perform the risk evaluation and mitigation of a potential slope failure. The traditional method to obtain information about these structures is the in-situ measurement made by an expert, however, this technique has some drawbacks since it requires a large number of measurements to have a representative sample of the discontinuities, and also the description of multiple features such as orientation, spacing, persistence, roughness, aperture, infilling, block size, wall strength, and seepage (Wyllie and Mah 2004). Besides, describing these features is sometimes not viable due to the risk level of the area under study. Therefore, in-situ measurements require a great amount of time, are limited by the possibility of accessing the area, and depend on the criteria of the expert. Hence, the use of remote sensing techniques to extract information about the structures of a slope instability has become a common practice in the hazard identification procedure, since as mentioned by Buyer and Schubert (2017) it has multiple benefits including the reproducible results, time optimization, a great level of detail, safe conditions during the investigation and the possibility to automatize the mapping and analysis of the collected data.

According to Battulwar et al. (2021), the main two remote sensing methods that have been used to characterize discontinuities are terrestrial or airborne LiDAR and photogrammetry using an unmanned aerial vehicle (UAV) to perform the *Structure from Motion* (SfM) pro-

cess. Both methods provide a 3D representation of the surface geometry and therefore they can be used to construct a high-resolution Digital Terrain Model (DTM). The difference between these two methods is related to their accuracy and the cost of the acquisition and data processing. LiDAR requires more expensive equipment and has more complex processing than the SfM from UAV (Cawood et al. 2017), however, this last method has a strong dependence on the image resolution, light conditions, and angle distortion (Chen et al. 2023). In Cawood et al. (2017) a comparison was done between these two methods and the time required to acquire and process the data with the traditional fieldwork method. Considering acquisition and processing, the areal SfM (ASfM) takes 8.5 hours being the fasted method, while LiDAR adds up to 40 hours from which 35 hours are related to the processing. Meanwhile, in the fieldwork measurements, acquisition and processing represent 11 hours in total. In this study, the accuracy of these methods was also confronted by comparing the virtual outcrops derived from these two remote sensing methods, and the planes measured in fieldwork using the compass-clinometer, the result showed that LiDAR had a maximum of 5° of deviation from the mean principal orientation of control planes, while ASfM had a maximum deviation of 42°. Thus LiDAR can be considered a high-accuracy method but with higher costs of implementation.

Many commercial software have been developed to extract automatically or semi-automatically the discontinuities and their features from the 3D point cloud or the derived surface, as listed in Alptekin and Yakar (2022). Also, many authors have developed their own algorithms for this end using a wide diversity of methods (Gigli and Casagli 2011; Lato and Vöge 2012; Kong, Wu, and Saroglou 2020; Chale, Joboyedoff, and Derron 2023; Chale, Joboyedoff, and Derron 2023) including the Random Sample Consensus (RANSAC) algorithm (Ferrero et al. 2009; Voyat et al. 2006; Roncella, Forlani, and Remondino 2005) which will be explained in the methodology chapter (4) since the construction of the proposed algorithm is based on it. These methods are focused on the description of discontinuities for the rock mass characterization for the stability analysis using exclusively the geometrical information derived from the imagined surface. According to Chen et al. (2023), the plane extraction process from the surface point cloud is based on three steps, the clustering of the 3D point cloud, the segmentation of the points that belong to the same structural group, and the calculation

of the occurrence of each discontinuity surface. Nevertheless, most of these algorithms have three main drawbacks, they require to set manually a threshold to consider a linear feature as a discontinuity, a manual selection is required during plane fitting, and when the methods are based on clustering the results are very sensitive to the initial position of the centers and setting of the number of clusters.

Few methods have been developed to extract structures using satellite-based Interferometric synthetic-aperture radar (InSAR) and thus the structures detected are related to large-scale discontinuities such as the method proposed by Roccheggiani et al. (2018) which uses the slope gradient derived from vertical displacements to extract the ground ruptures associated to an earthquake. Another example is the method described by Libert, Wuite, and Nagler (2022) to delineate cracks in an ice shelf using the Canny Edge Detection algorithm on a phase gradient map. However, no method has been proposed for GB-SAR data which has a higher temporal frequency, is used for smaller areas.

Since GB-SAR provides displacement maps from the phase information, and not optical images or surface geometry information, the structures extracted from this data are different than the discontinuities mapped with the methods mentioned previously (LiDAR and SfM). The potential to use GB-SAR for geological structures is entirely related to the boundaries of the displacement of the slope instability. Meanwhile, LiDAR and SfM can map the stable discontinuities but do not give direct information about their role in the deformation. Another difference between these methods would be the acquisition of data, since GB-SAR can be used in continuous monitoring mode, giving radar images every few minutes for monitoring and early warning purposes, while LiDAR and SfM point clouds are usually acquired to retrieve a high-resolution DTM or if they are used for monitoring changes, the time-span of their acquisition can be some days or even months. In summary, the extraction of structures using GB-SAR could be used during the monitoring of a slope instability and it would provide information about the structures involved in the deformation for early warning, while the utilization of LiDAR and SfM for extracting discontinuities is primarily associated with the physical characterization of the slope. Therefore, the methods mentioned can be used as complementary during the different stages of a slope investigation campaign.

4 Methodology

The development of the algorithm was done using MATLAB R2023a. It comprises multiple subroutines that are required to extract the 3D planes related to the geological structures that are involved in the displacement of the rock or soil mass causing a slope instability. The general algorithm is structured with the following steps:

1. 2D velocity map creation.
2. 2D velocity map filtering.
3. Velocity threshold clustering of the area selected by the user.
4. Binary 2D edge detection.
5. Geocoding of 2D velocity map and Edge point set.
6. Clustering of the 3D edge point cloud.
7. Seed selection.
8. Iterative plane fitting.

Each step and its required inputs are described in the following chapters, detailing some of the MATLAB functions used, from which some are included in the MATLAB packages, others were developed by different authors and are found in the online Mathworks *File Exchange*, and some were developed by the authors of this thesis. The structure of the general algorithm with the required inputs for each step is also detailed in the following flowchart of Figure 9.

From these processes, one of the main contributions of this study is the velocity threshold clustering since this process allows extracting semi-automatically the deformation velocity limit to consider an area as unstable. This has been a challenge for the GB-SAR data processing, considering the noise in the data and the smooth transition between stable and unstable pixels, which makes it difficult to set a boundary between these two areas, a process that is currently done manually. Also, the new method for 3D plane fitting is an important contribution since it is developed specifically with the aim of extracting planes that "cut" the surface of the slope, while other methods extract planes without considering a desired direction.

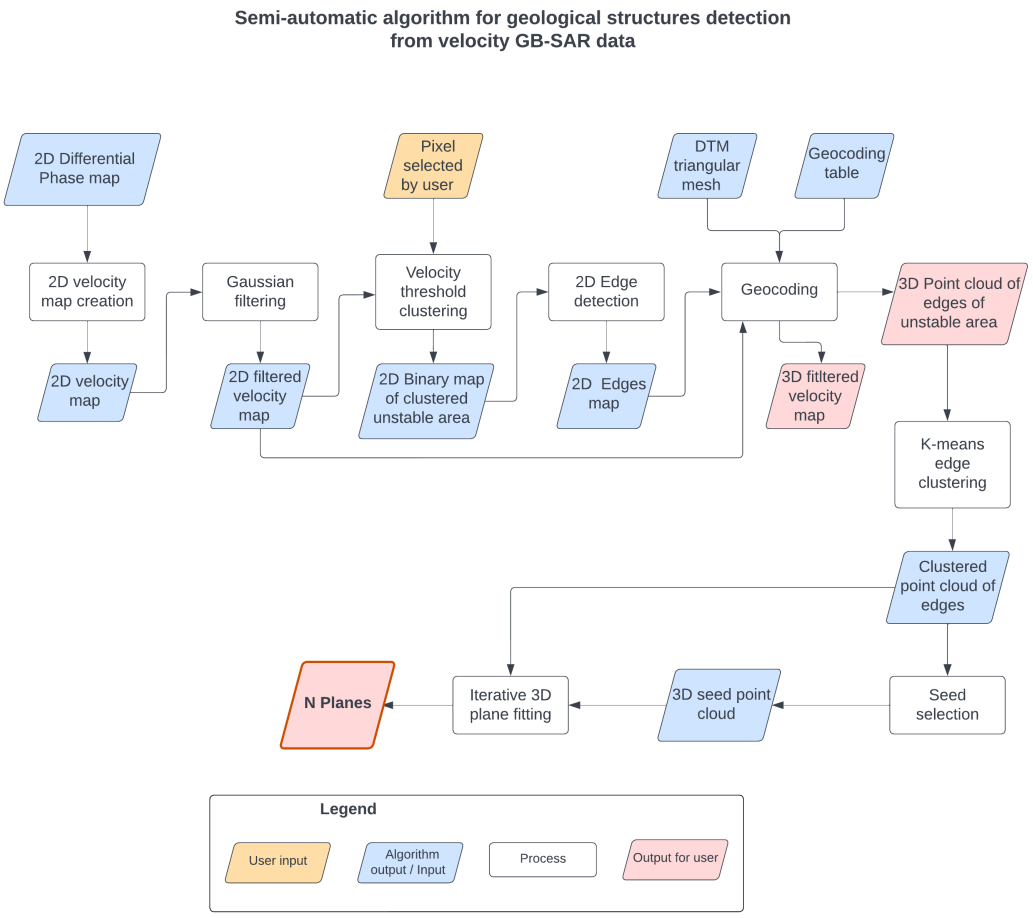

Figure 9: Flow chart describing the general steps of the developed algorithm

The first step of this algorithm is the creation of the 2D velocity map from the pre-processed data of the GB-SAR acquisition. The velocity is chosen as the parameter to perform this process since it gives a reference both on the magnitude and the time scale of the hazard, which is relevant for its mitigation. While, if only the displacement is considered, there would be no information about the time-scale of the deformation, and in terms of geological risks this is a very relevant factor to be considered.

4.1 2D velocity map creation

To extract the velocity map, it is required to have the phase information of a differential map after atmosphere removal, noise reduction, and phase unwrapping. As mentioned in the previous chapter, these steps are done in the pre-processing of the GB-SAR data after its acquisition and are not discussed in this study. After extracting the interferometric phase

($\Delta\phi$) in a desired time period, and using the equation (10) with a λ value of 17.43 mm corresponding to the Ku-band, the total displacement (ΔR) in mm can be calculated. To find the velocity map, the time difference in hours (Δt) between the selected acquisition times is calculated, then the following equation is used:

$$V = \frac{\Delta R}{\Delta t} \tag{11}$$

The velocity of the slope displacement (V) is not necessarily constant during the selected time interval, so the value used for this processing is the average velocity of the deformation since only the final displacement is considered. After this step, the 2D velocity map of the area is acquired. Nevertheless, the resultant map still contains a high noise level, which represents an issue for edge detection processing. An example of the resultant 2D velocity map is shown in Figure 10:

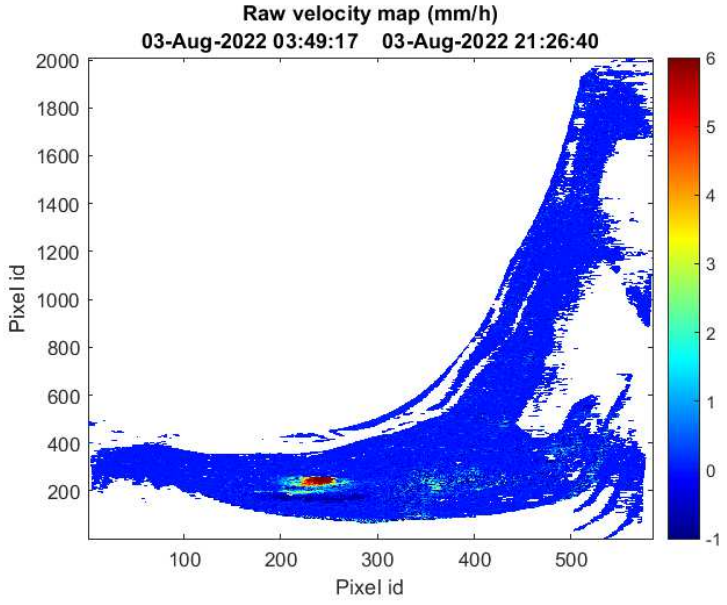

Figure 10: Velocity map example. Positive values are approaching the sensor.

As mentioned above, even after the phase unwrapping and atmospheric correction, the noise level can be very high. In this example it can be visualized especially in the lower part of the image, and near the unstable area, which would affect the detection of its edges. Hence, before doing this process is important to filter the velocity map before performing other processes.

4.2 2D velocity map filtering

The aim of this step is to decrease the noise level while preserving, as closely as possible, the original boundaries of the unstable areas. For this, four types of filters were used to test the effects on the 2D velocity maps:

1. **Median Filtering**

   This filter works by calculating the median in a $m \times n$ moving window (m and n are odd). Then, in the filtered map, this value is assigned to the central pixel of the window. The MATLAB function used to perform the median filtering was developed by Voronov (2013) which is very suitable for this case since it is able to omit "Not a number" (NaN) values, and therefore it calculates the mean even if there are NaN pixels in the window. This is common in this case, especially at the boundaries, but it can also occur in the central areas of the map. After several tests with different window sizes, a 5×5 window was chosen to apply this filter to the 2D velocity map.

2. **Kuwuhara-type Filter**

   This filter is also performed using a moving window, that was originally designed as a 3×3 window with four 2×2 sub-windows. In each sub-window, the variance and the mean are calculated, and finally, the mean of the sub-window with the lowest variance would be assigned as the value of the central pixel (Kuwuhara et al.,1976 as cited in Burger and Burge (2022)). In this algorithm, and as suggested by Tomita and Tsuji (1977) (as cited in Burger and Burge (2022)) a fifth central region is added. As in the case of the median filter, a 5×5 window was chosen. In Figure 11 the sub-window scheme is exemplified, where the central pixel (red) is the pixel that takes the mean value of the sub-window (blue) with the lowest variance.

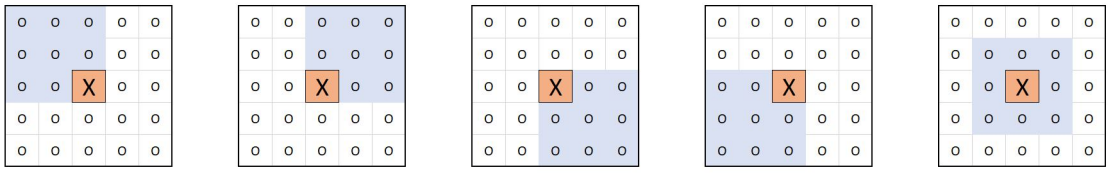

Figure 11: Scheme of kuhuwara type filter

3. **Nagao-Matsuyama filter**

According to Burger and Burge (2022) the square sub-windows in the Kuwuhara-type filter could generate artifacts in the final image, therefore a modification of the sub-window geometry is proposed. In a 5×5 window, the sub-windows are designed as follows:

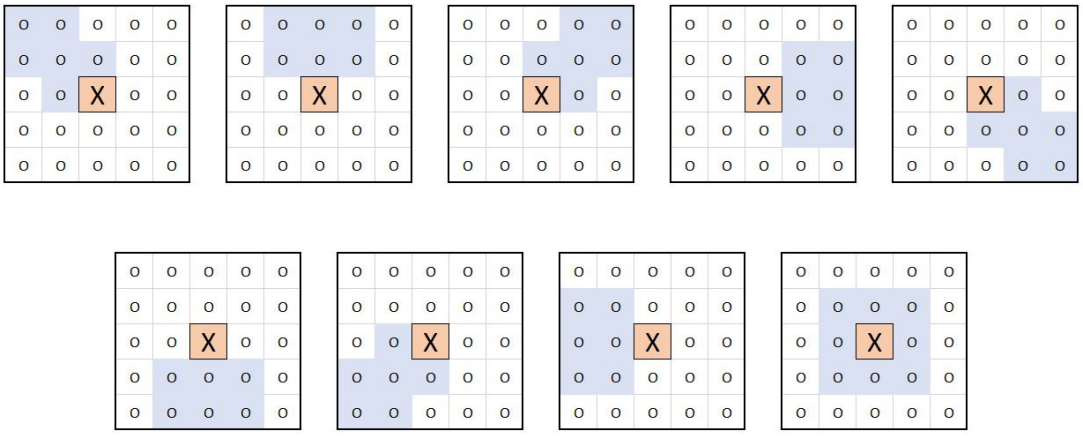

Figure 12: Scheme of Nagao-Matsuyama filter

The procedure to calculate the value of the central pixel is the same as in the Kuwuhara-type filter, but in this case, the selection of the mean is done considering the variance of nine sub-windows shown in Figure 12. Again, the mean of the sub-window with the lowest variance would be assigned as the value of the central pixel.

4. **Gaussian filter**

In contrast to the previous filters, a Gaussian filter is convolution-based, which means that it does not use calculations on a moving window of the 2D velocity map. To perform the convolution, a 2D Gaussian distribution is modeled using a 2D kernel, that should represent a distribution given by the discrete equation (12).

$$H(x,y) = \frac{1}{2\pi\sigma^2} exp(-\frac{x^2+y^2}{2\sigma^2}) \tag{12}$$

According to this equation, the Gaussian filter would have its maximum in the center, and it would decrease following a width that depends on the assigned standard devia-

tion (σ). For the filtering of the 2D velocity map, a 5×5 kernel was used, modeling a Gaussian distribution with a $\sigma = 1.4$, as shown in Figure 13.

$$\frac{1}{159}\begin{bmatrix} 2 & 4 & 5 & 4 & 2 \\ 4 & 9 & 12 & 9 & 4 \\ 5 & 12 & 15 & 12 & 5 \\ 4 & 9 & 12 & 9 & 4 \\ 2 & 4 & 5 & 4 & 2 \end{bmatrix}$$

Figure 13: Kernel used for the velocity map filtering

Having the modeled kernel, a 2D convolution is performed on the 2D velocity map. In this case, since there are pixels with NaN value, the MATLAB function *nanconv* developed by Benjamin Kraus (2013) is used. This function has the ability to ignore the NaN values, so if this type of pixel is found at the convolution, it will continue the calculation and assign the calculated value. Meanwhile, using the regular MATLAB function *conv2* if during the convolution a NaN value is found, the resulting value would be also NaN, thus increasing the number of NaN pixels in the final filtered map.

4.2.1 Filter comparison

To decide which filter is most suitable a qualitative analysis of the resulting filtered maps is done. For this, a comparison between the different filtered maps, using a case study as an example. The zoomed area displayed in Figure 14a is chosen to demonstrate the efficiency of each filter; this area is problematic in the raw map since it contains many noisy pixels, near the unstable area. These noisy pixels could complicate the delimitation of this area, representing a problem for further steps, such as velocity clustering and edge detection.

Comparing the filtered maps, the variations of the noise reduction and the edge blurring are noticeable. The Nagao-Matsuyama (Figure 14e) and the Kuwuhara-type (Figure 14c) filters seem to be accurate at conserving the original edges of the raw velocity map, displaying a low blurring. However, the noise is incremented at the boundary of the unstable area, and this is not desired. Meanwhile, the Median (Figure 14b) and Gaussian (Figure 14d) filters have a greater blurring effect on the edges, but the Gaussian filter seems to have a better effect on the noisy pixels than the Median filter.

In traditional edge detection methods on regular image processing, it is essential to conserve the original edges, therefore the development of complex filters to perform noise reduction while conserving the edges is a crucial task. Considering this, in the traditional image scenario the Kuwuhara-type and Nagao-Matsuyama filters have a better performance. However, in this study, the development of velocity threshold clustering and the method of binary edge detection simplify this problem. Therefore, the main goal of the filter application is noise reduction, while the blurring of the edge is tolerable. Hence, the chosen method is the Gaussian filter, which performs the best on noisy pixels but still conserves a nice delimitation of the unstable area even after a slight blurring.

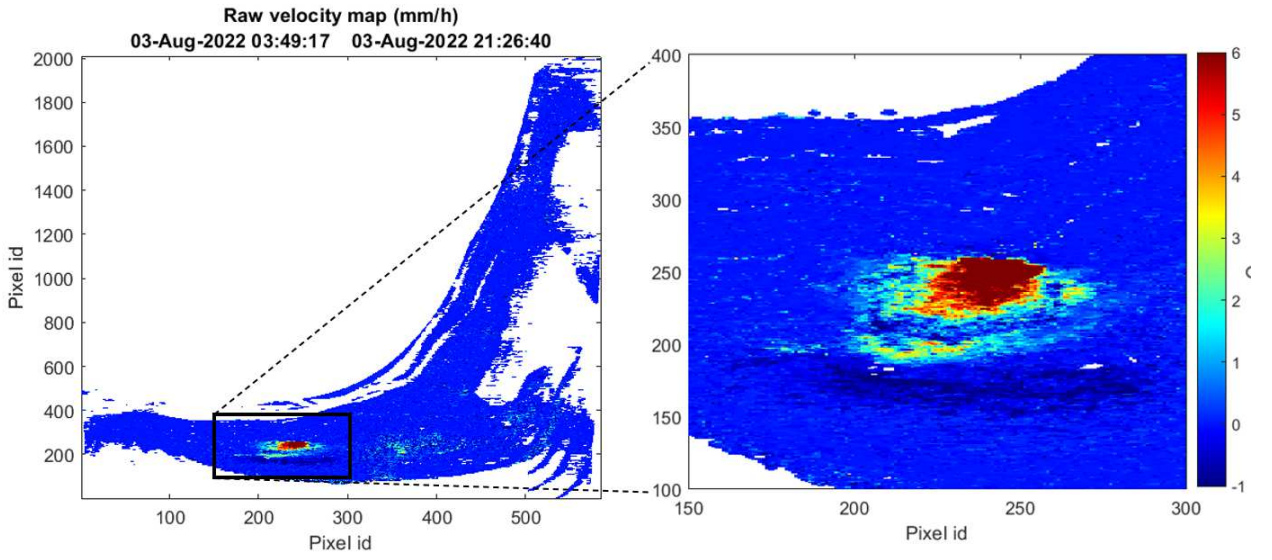

(a)

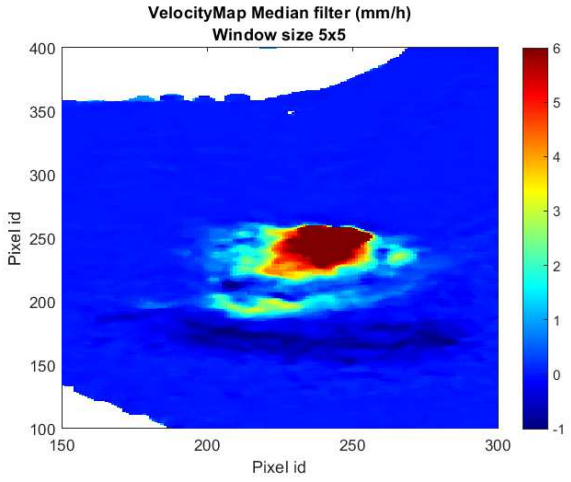

(b)

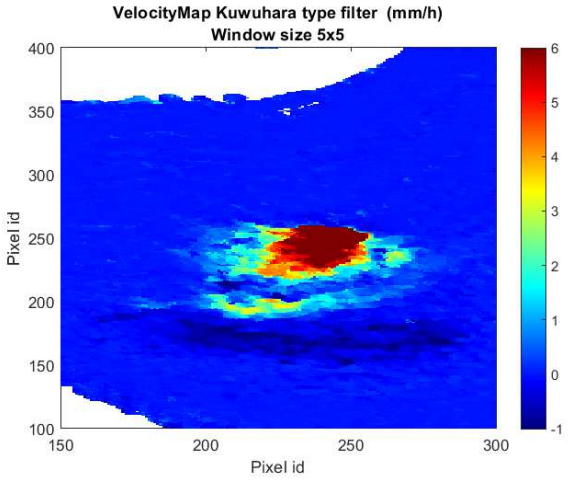

(c)

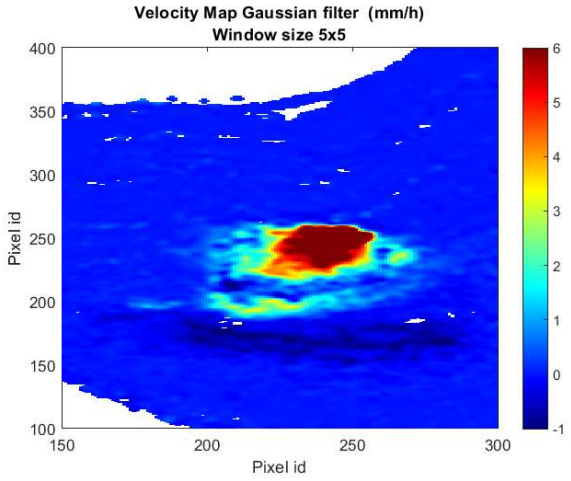

(d)

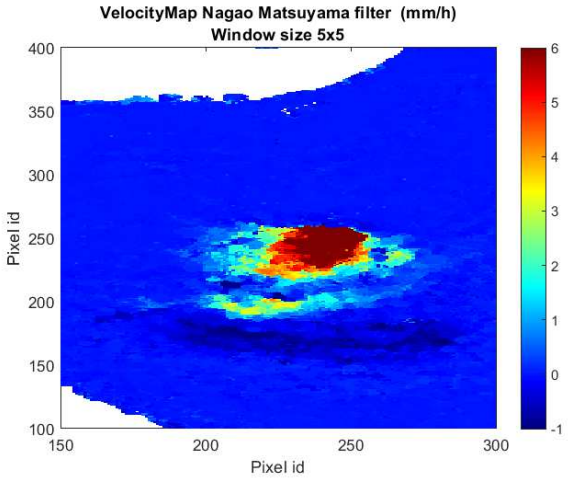

(e)

Figure 14: (a) Zoomed area of raw velocity map. (b) After median filter, (c) after Kuwuhara type filter, (d) after gaussian filter and (e) after Nagao filter. Positive velocity values are approaching the sensor.

4.3 Velocity threshold clustering

Depending on the acquisition mode, GB-SAR can cover about 60° to 360° of the field of view, which means that many unstable areas may be detected in a single acquisition. To develop this algorithm, it was decided that the user should select the area of interest to extract the geological structures. Considering this, the algorithm would be semi-automatic, since the user has to provide input of the desired area, this is done by a single click on the 2D velocity map to select a pixel contained in the unstable area.

The next step is to define the extent of the selected unstable area, and to this end, a velocity threshold must be set to fix the minimum velocity for a pixel to be considered not stable. This is done since the stable pixels do not necessarily have a velocity equal to zero due to the noise in the data, and because usually, the transition between a stable and a moving area is not a sharp limit. Hence, defining the limit between the two areas requires defining a velocity limit.

In Figure 15 the processes of the velocity clustering algorithm (white boxes) are enumerated to be referenced in the explanation of the method, which is mainly divided into two sections, the definition of the cluster size (S) as a function of the velocity of displacement (deformation) (V_d) and the velocity threshold selection. From this, the expected output is a binary map with a single cluster of pixels that represent the unstable area selected by the user. Also, the final velocity threshold itself could be considered an output, since this value could be the input for the early warning estimation. Thus, this process is not only valuable for the extraction of the geological structures but also, could be useful for the alarm system involved in risk mitigation.

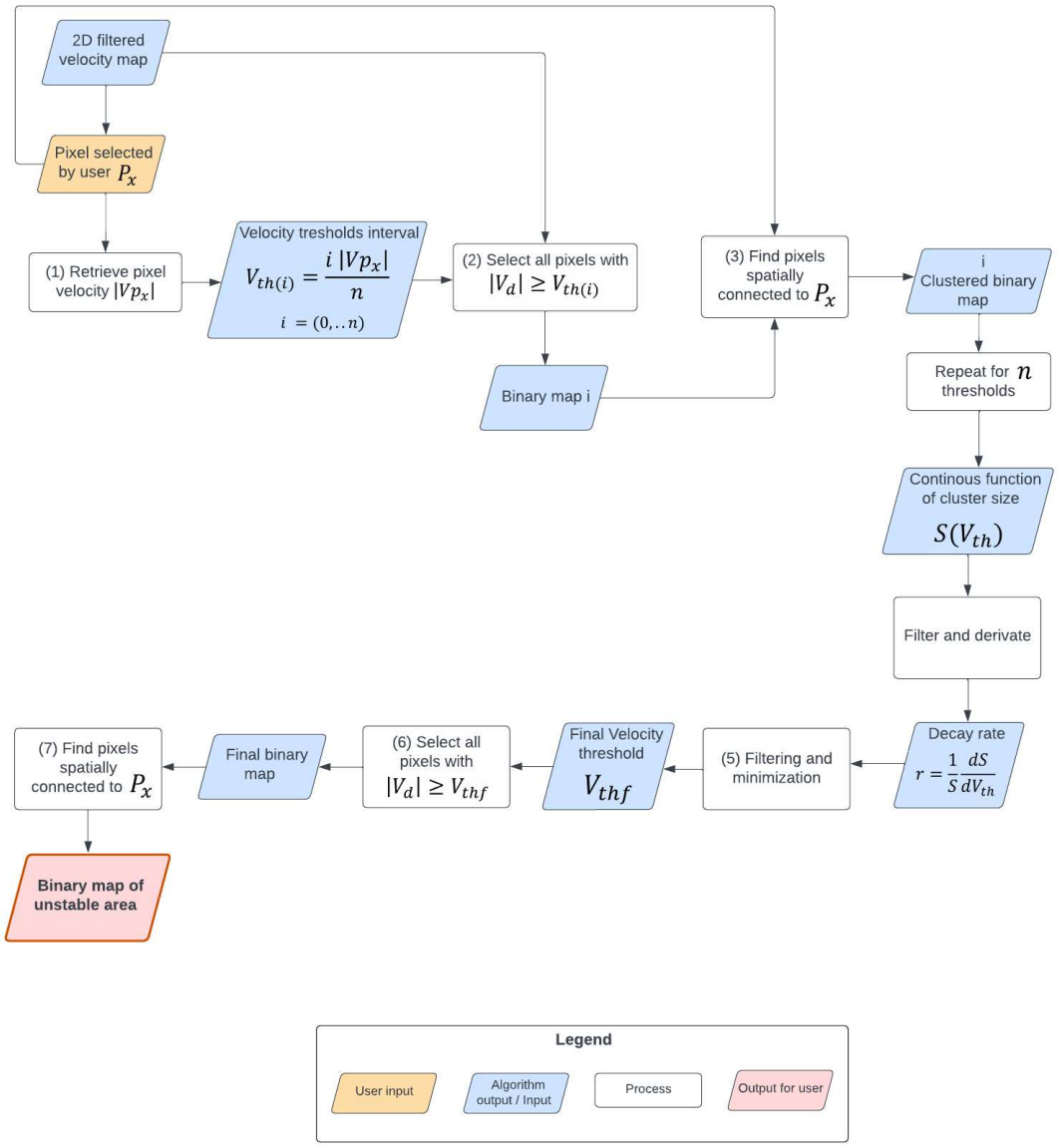

Figure 15: Flow chart of velocity threshold clustering

4.3.1 Cluster size as a function of velocity

In the first part of the algorithm, a range of velocities is tested in order to define a function that describes the relationship between the size of the unstable area (S) and the velocity thresholds (V_{th}). For this, the pixel that the user selects (P_x) on the 2D filtered velocity map, works as the input that defines an interval of velocity thresholds ($V_{th(i)}$), the absolute velocity of P_x ($|Vp_x|$) defines the upper limit of the range, while, the lower limit of the interval is 0. The total number of thresholds contained in $V_{th(i)}$

are n velocities, with the index $i = 0, ...n$, being this interval the output of the process (1) in Figure 15.

$$V_{th(i)} = \frac{i\ |Vp_x|}{n} \tag{13}$$

To exemplify this process, Figure 16 shows the pixel selection made by the user:

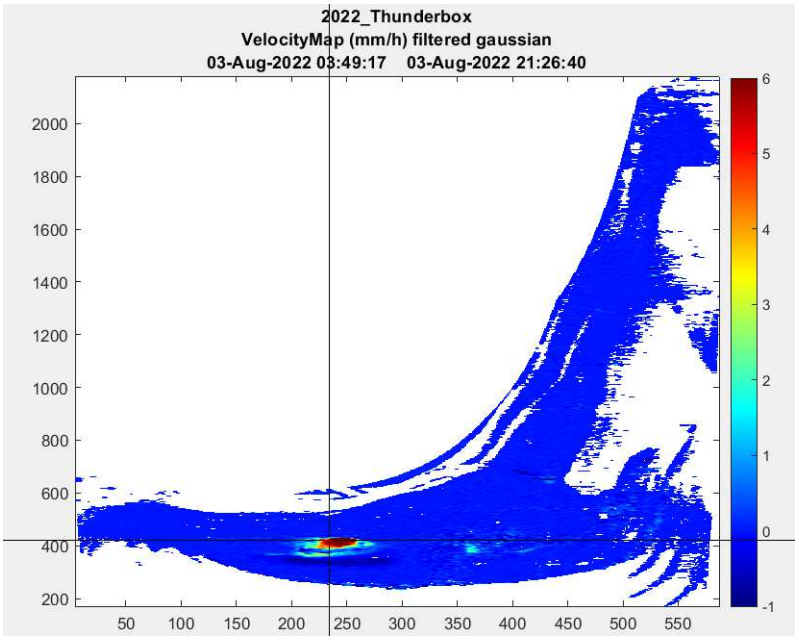

Figure 16: Example of pixel selection in the area of interest.

After the definition of this interval, an iterative process starts from $V_{th(i)} = 0$, testing all the velocity values inside $V_{th(i)}$. During this loop, each threshold is compared against the displacement velocity of all the pixels contained in the 2D map, if a pixel has a higher or equal velocity than $V_{th(i)}$ it is included on a binary map. So at the end of the process, n binary maps are created, one for each threshold, including the pixels that exceeded the correspondent velocity. Taking as an example the velocity map in Figure 16, the resulting maps after three iterations are:

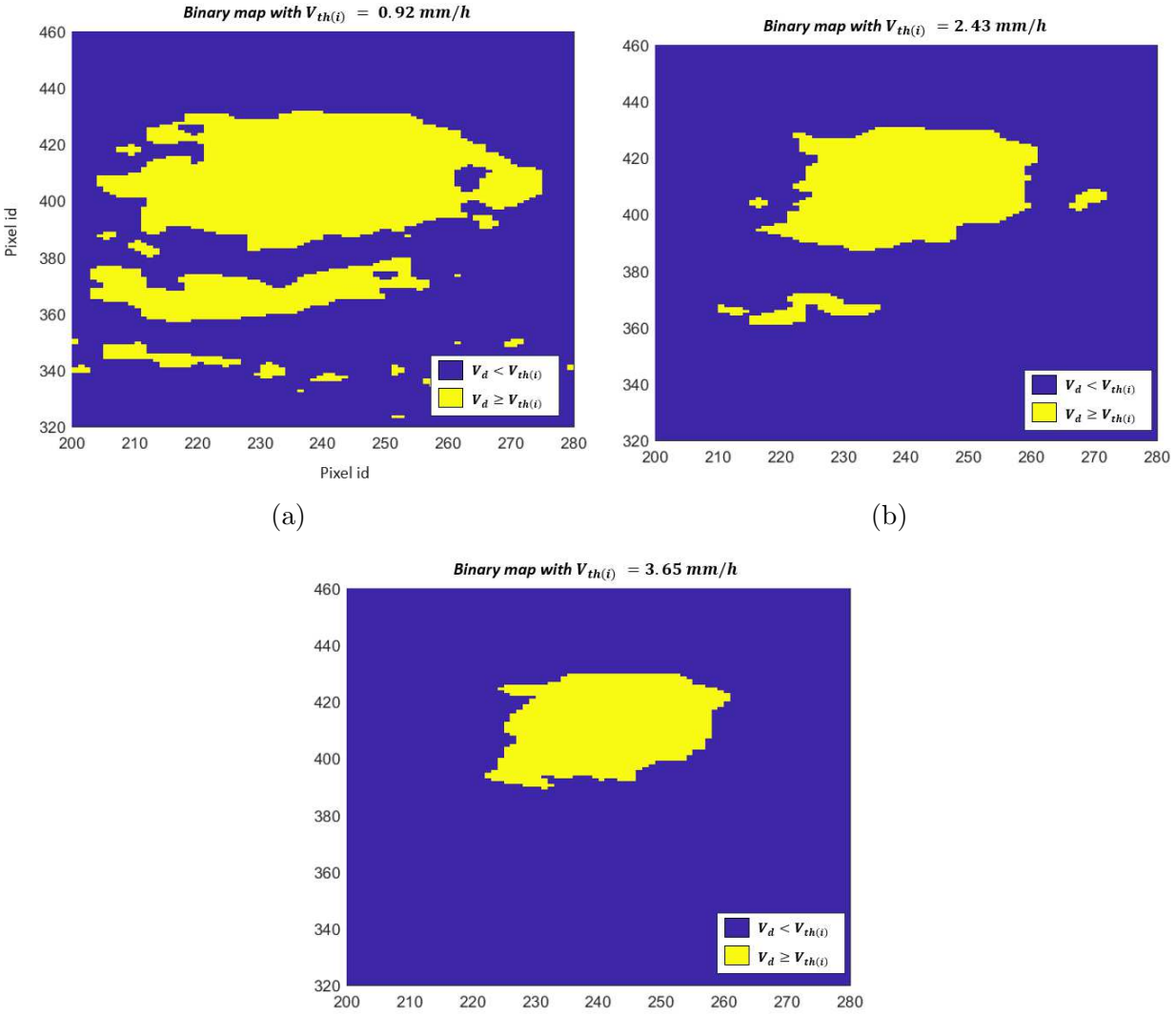

Figure 17: Binary maps of pixels with absolute velocity values (mm/h) greater than 0.92 (a), 2.43 (b), and 3.65 (c) in yellow.

With this example, the outputs of the process (2) are visualized, showing how the number of pixels that exceed $V_{th(i)}$ on each binary map starts to decrease with the increase of the velocity threshold value. However, in this step, the pixel selection considers all the pixels of the 2D velocity map and not only the ones connected to the area selected by the user. For this, in process (3), it is necessary to isolate the pixels spatially connected to P_x in each binary map, this will create a single velocity cluster of the area of interest for every map. If the user selects the pixel shown in Figure 16, the resulting maps would be clustered as exemplified in the following figure:

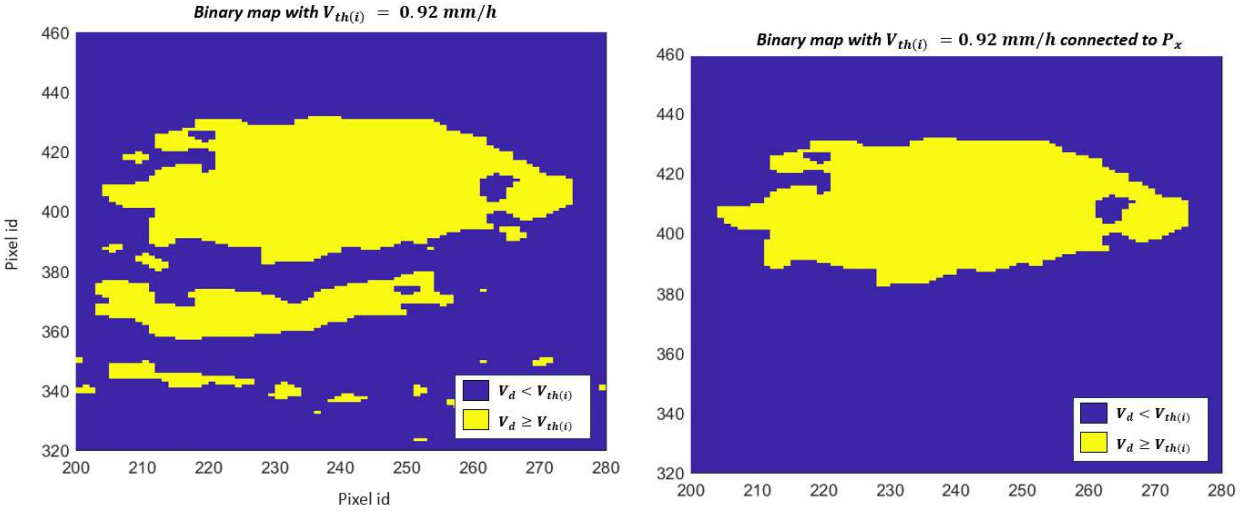

(a) (b)

Figure 18: Binary maps of pixels with velocities greater than 0.92 mm/h for all the pixels in the 2D map (a) and the clustered pixels (b).

The output for each iteration i in the process (3) would be a connected cluster for each threshold $V_{th(i)}$, such as the one in Figure 18b. The total number of clustered pixels is extracted from each binary map, resulting in n cluster size values. With this, the relation between the size of the cluster (S_i) and the velocity threshold ($V_{th(i)}$) is obtained. As a result, the final output of the loop would be the continuous function $S(V_{th})$ in the interval $[0, Vp_x]$.

4.3.2 Velocity threshold selection

The aim of this step is to find a single velocity value that allows to isolate the unstable area selected by the user using the output of $S(V_{th})$. As shown in Figure 19b the cluster size can have multiple behaviors.

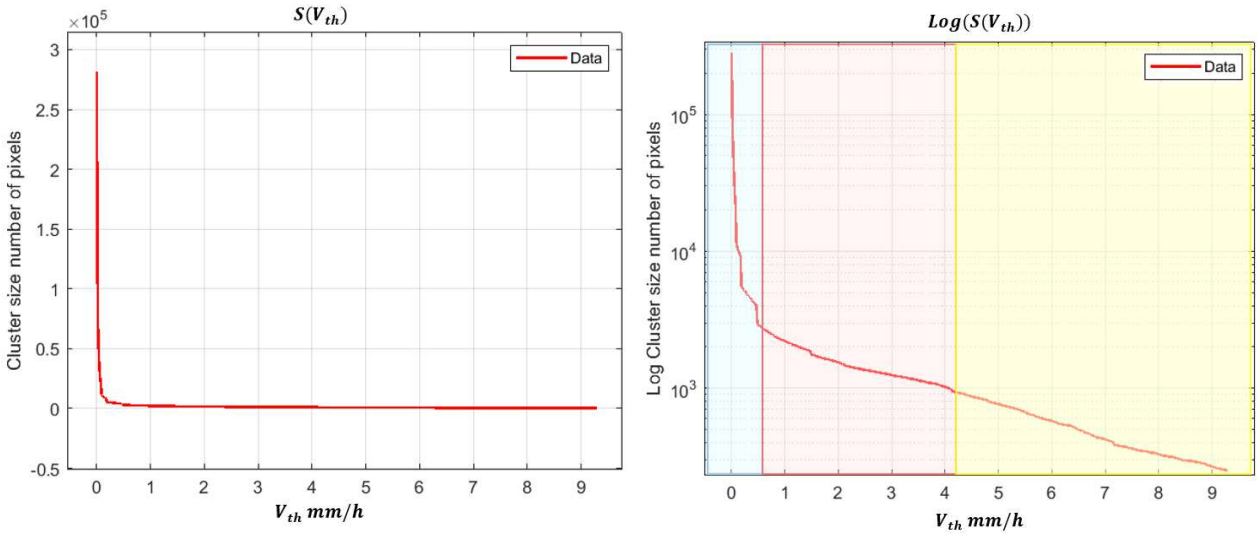

(a) (b)

Figure 19: Cluster size (number of pixels) as a function of the velocity thresholds (a) and its logarithmic graph (b).

The cluster size tends to 0 for most of the velocity values since the unstable area is very small compared to the total number of pixels in the 2D velocity map as illustrated by Figure 19a. Therefore, to visualize the variations of the cluster size the logarithmic graph (Figure 19b) will be used as a reference, where three main slope changes can be differentiated. The first part of the graph in blue, shows how the cluster size reaches its maximum value after taking all the pixels that have an absolute velocity higher than 0. In this part of the graph, the rate at which the cluster area increases is very fast, hence the cluster size is not stable. The area of interest for extracting the possible velocity threshold is the red area. Here, the velocity values are not that high and the cluster size is not that small, so the unstable cluster can be extracted without underestimating the area of the instability. The yellow area is where the fastest deformations could be extracted, but it would be very limited to relatively fast displacements and very small areas, underestimating the implications of medium velocities on the deformation.

The final velocity threshold should be related to a stable cluster size, this means that it must allow to cluster the moving pixels without including velocity values that do not represent the general behavior of the unstable area. This means that the rate of change in the function $S(v_{th})$ must be low around that value. Thus, minimizing the

first derivative of this function could be an effective estimation of the final velocity threshold. Nevertheless, after some tests, it was proved that using the derivative of $S(V_{th})$ is not a good method to find the velocity threshold, since its value is dependent only on the velocity at which the area grows but it does not consider that the size of the cluster must also be representative. To explain this, the derivative graph Figure 20 is used:

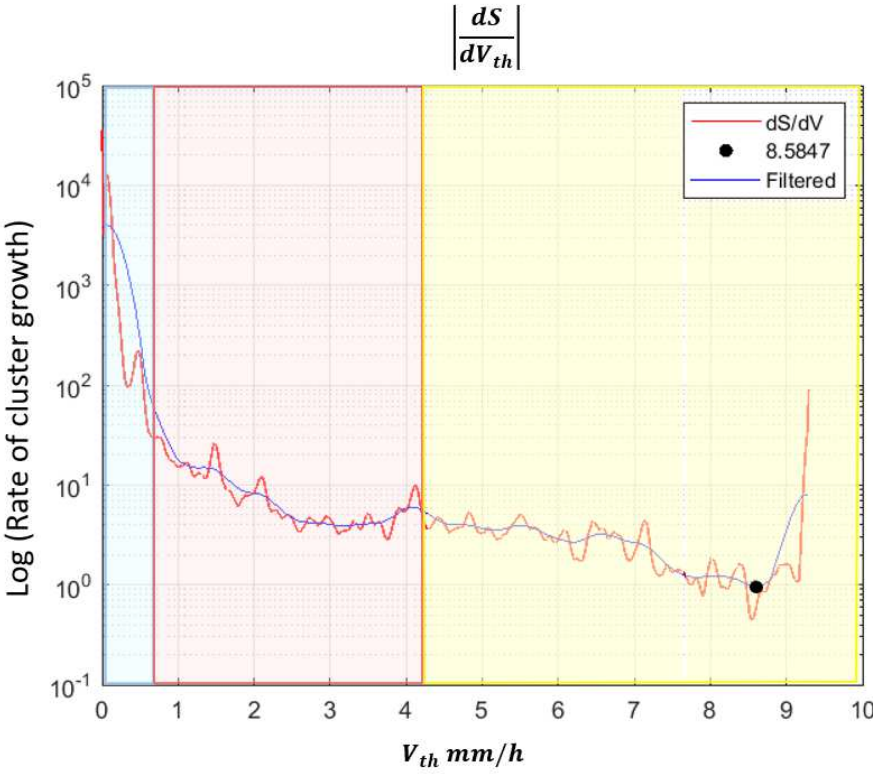

Figure 20: Example of the derivative of cluster size as a function of velocity, in blue is the filtered curve. The point represents the minimum value.

In this figure, the minimum value of the derivative is located in the yellow area, where the rate of growth of the cluster is low because it considers very few pixels, the ones with a very high velocity of displacement. Choosing this threshold would restrict the cluster to very fast movements, neglecting areas with relevant deformation. This happens because the derivative considers only the velocity at which it changes, but not the number of pixels that are involved in the variation. In the yellow area, as very few pixels are considered, the magnitude of the size variation is very low.

In Figure 21 is proven that an exponential decay function can be fitted to $S(V_{th})$, which

shows that the rate of change of the cluster size depends directly on its current value. This behavior helps to overcome the challenge of choosing a very high velocity as the final threshold.

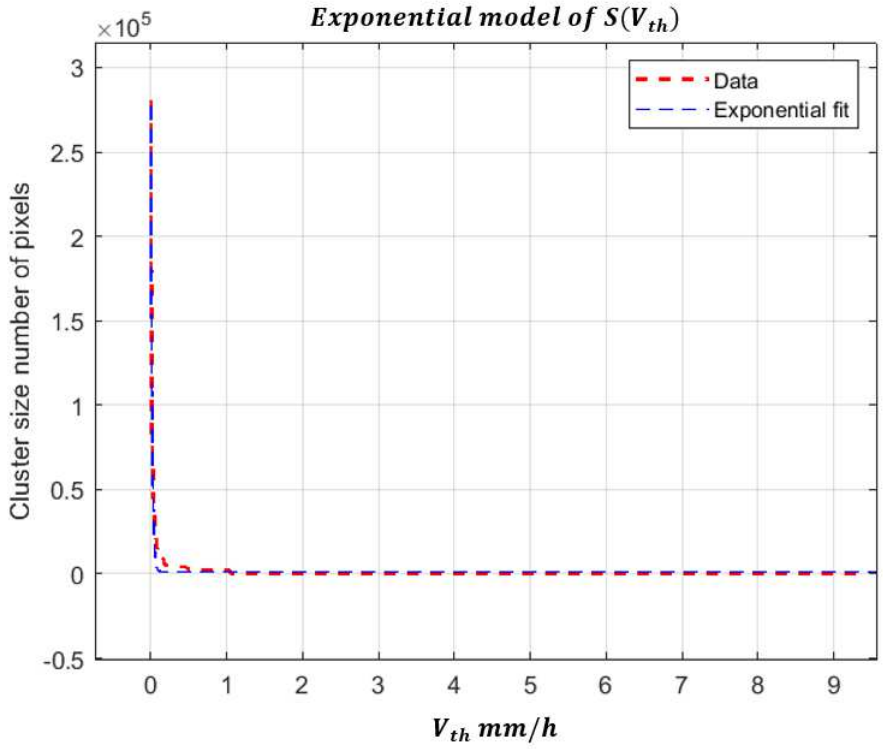

Figure 21: Exponential decay fitted to $S(V_{th})$

The exponential decay, in this case, can be described with the following differential equation:

$$\frac{dS}{dV_{th}} = -rS \tag{14}$$

Where r is the exponential decay constant or the rate of decay. This value gives information about how the current cluster size contributes to its own decrease, meaning how quickly the cluster size shrinks *per pixel* that is already in the cluster. This constant behaves as follows:

- If r is positive, the cluster size is decreasing.
- If r is negative, the cluster size is increasing.
- If r is zero then the cluster size is stable.

Since r is the parameter that determines if the cluster size is stable, the target equation 14 is:

$$|r| = \left| \frac{dS}{dV_{th}} \frac{1}{S} \right| \tag{15}$$

This way it is easier to observe that r gives information about the rate at which the cluster size grows and that it also depends on the current size of the cluster itself. This means, that for the high velocities found in the yellow area of Figure 20, which result in very small clusters (low S), r will have a larger value, compared to the mid-size clusters in the red area, where r would be closer to zero. Finally, the minimum value of r is found, thus, the corresponding velocity threshold would be the final velocity threshold V_{thf}.

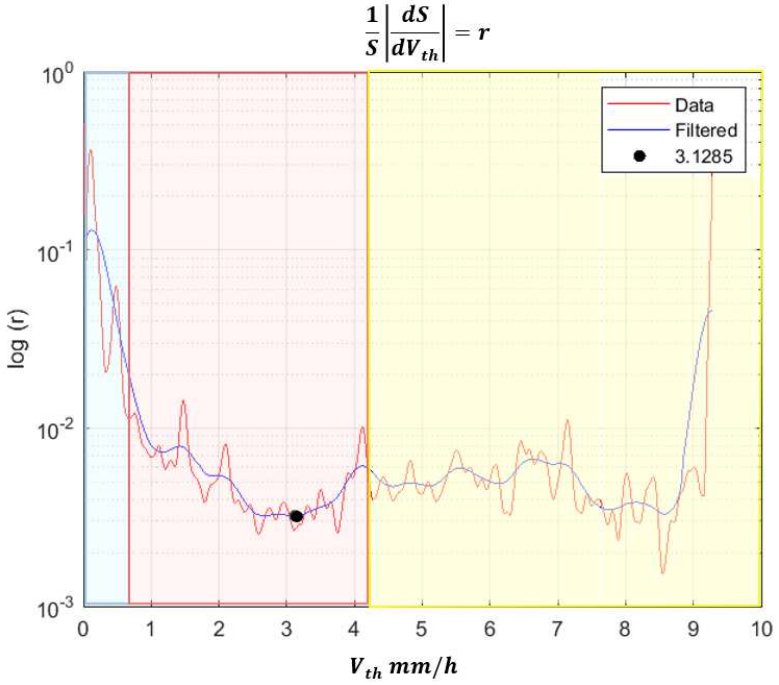

Figure 22: Rate of decay r of the cluster size growth in logarithmic scale with the final velocity threshold

It is important to highlight that the noise in the data causes the velocity threshold selection to be not entirely accurate even after filtering. However, this is not relevant since the idea of using r to find the velocity threshold is to select it from a velocity interval where the size of the cluster is stable, thus even though the velocity threshold value could slightly vary, it would not cause a relevant change in the size of the final

cluster. This would give us the output of the process (5) in the flow chart of Figure 15.

After finding the final velocity threshold (V_{thf}), the final binary map is defined with the pixels that have a displacement velocity greater or equal to this value ($V_d \geq V_{thf}$). Finally, the output of the process (7) would be a cluster with the pixels that are spatially connected to P_x, resulting in the final clustered binary map that will be used to extract the geological structures. An example of the final binary map, according to the pixel selection shown in Figure 16, is:

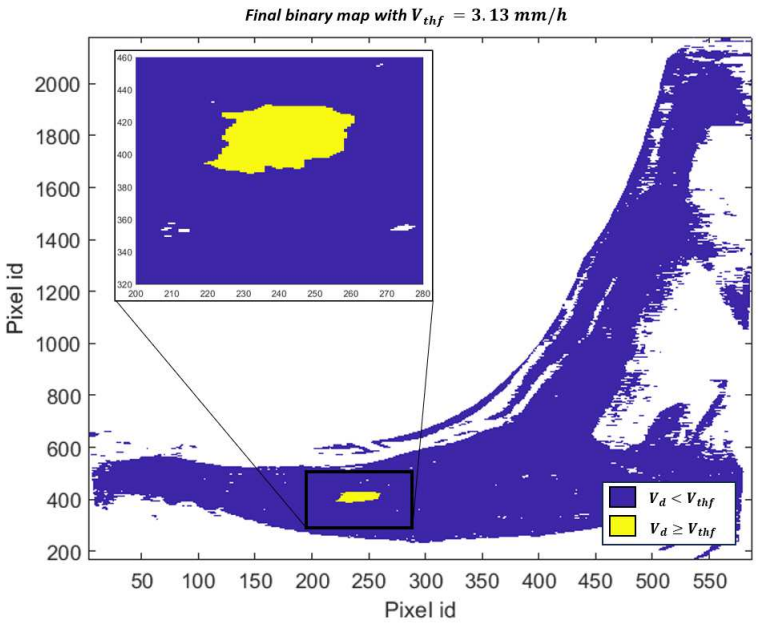

Figure 23: Example of the final binary map that will be used to extract the geological structures

In this case, the final velocity threshold that clusters the pixels in yellow is 3.13 mm/h, which could also be used in the early warning system. The area clustered with this velocity would be considered as the unstable zone in the area of interest selected by the user. According to the general algorithm in Figure 9, the following step after extracting the final binary map output is the 2D edge detection of this area, which would allow the delineation of the planes related to the geological structures.

4.4 Binary 2D edge Detection

The final clustered map will be a binary map, where the pixels that are part of the cluster that represents the unstable area will have a value of 1 while the value of the pixels that are outside the cluster is 0. This binary output simplifies the edge extraction since in the usual algorithms for image processing, the detection is done in smooth transitions, so the complexity of the algorithm increases. In this case, the boundary is already defined by the velocity threshold clustering, and therefore the edge detection problem is reduced to a binary identification.

The developed algorithm is based on a 3×3 moving window with 4 pairs of pixels. Each pixel pair is located opposite from each other, as shown in Figure 24 :

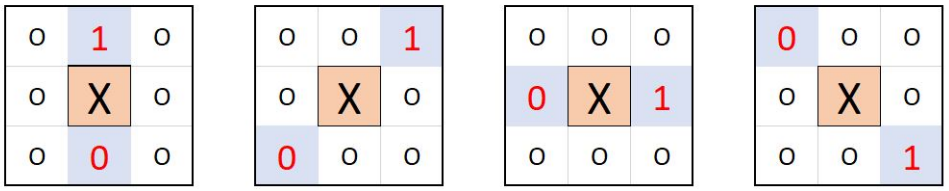

Figure 24: Scheme of moving window for edge detection.

The value of each pixel pair is compared, and in case they have different values, the central pixel (red) would be classified as an edge. Moreover, it is only necessary for a single pair to have different values to consider the central pixel as an edge. This process could be skipped in two cases: first, to avoid the creation of edges in areas with NaN values, when there is a pixel with a NaN value in the window. Second, if in the window there is a pixel that is already considered an edge, this will avoid the creation of a thick edge, which means that the border is defined for more than one consecutive pixel as illustrated in Figure 25a:

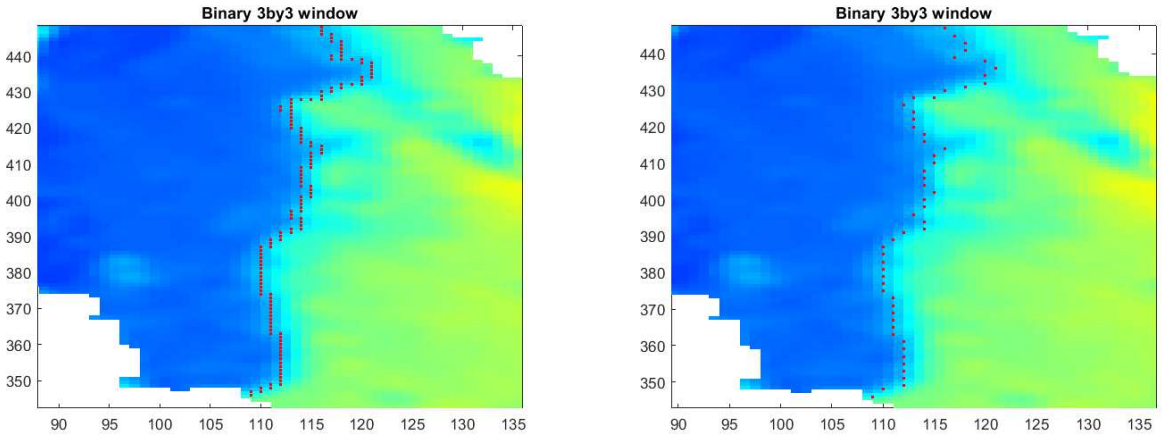

(a) (b)

Figure 25: Pixels detected as an edge in red. Thick edge (a) and thin edge (b).

Generating a thin edge as in Figure 25b is important because, during the 3D plane fitting, the dispersion of pixels in the width of the border affects the direction of the extracted plane. But, if the border is defined by a thin edge, the direction of the plane will depend only on the direction of the edge itself not on its width. The final result is a 2D pointset, the following image represents an example of the final edge extraction for the selected area on the velocity map:

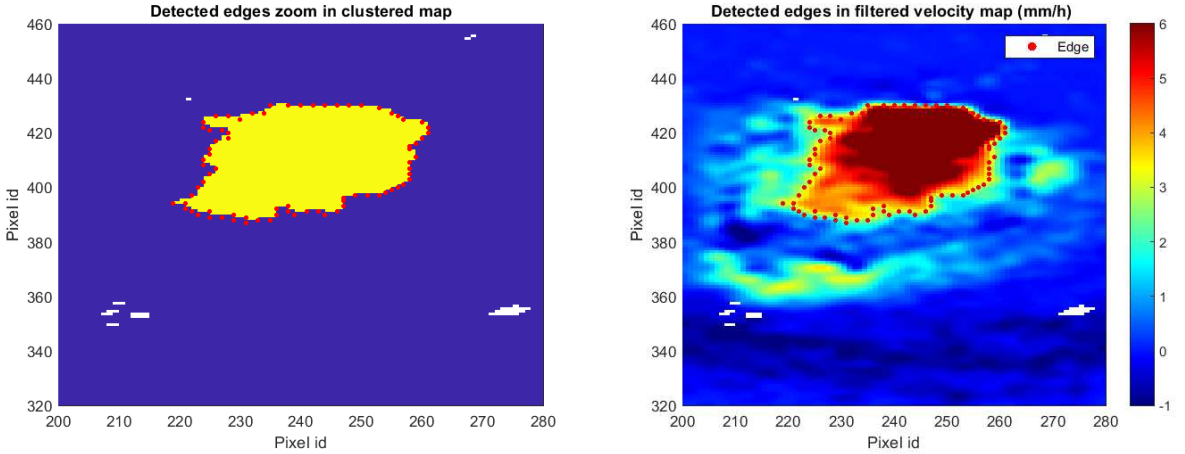

(a) (b)

Figure 26: zoom of the detected edge 2D point set displayed on the binary map (a) and on the filtered velocity map (b). Positive velocity values are approaching the sensor.

4.5 Geocoding of 2D velocity map and edges

Geocoding is the process in which the 2D maps in x and y coordinates, are translated to the Digital Terrain Model (DTM) in 3D (Monserrat, Crosetto, and Luzi 2014). This is a fundamental step since, as mentioned before, the dimensions of the radar cells do not correspond to the ground dimensions, and they record the three-dimensional measurements projected on the range and azimuth range coordinates causing distortions as overlay and shadowing (Moreira et al. 2013) as depicted in Figure 7.

The DTMs can be represented in a rectangular grid, where each pixel has an *x,y,z* coordinate, or a triangular mesh, where each vertex and face centroid, has an *x,y,z* coordinate. The resolution of the DTMs should be higher than the radar map, which means that one radar cell corresponds to several cells or faces in the DTM, this way, the resolution of the radar data is not lost after the geocoding. In the general algorithm, as shown in the flow chart of Figure 9, the required DTM input is a triangular mesh, in which one triangular face, that can have different dimensions, has a centroid, three vertex, and three edges (Figure 27a).

The second required input is the Geocoding Table, a matrix that relates each face ID with the radar pixel IDs that overlap with it. It also contains information on the overlap percentage which is required to assign the radar value to a triangular face. This process is schematized in Figure 27b:

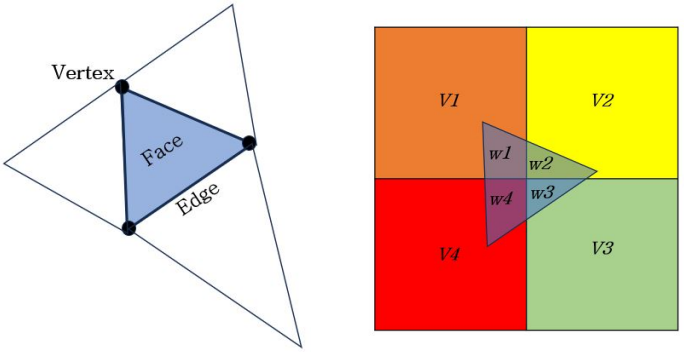

(a) (b)

Figure 27: Triangular mesh scheme (a) and radar values to triangular face scheme, each color represents a pixel value (b).

This scheme shows how the value of the triangular face is assigned. In this example, one face of the triangular mesh overlaps with four radar pixels, however, the overlapping can happen with a single pixel or with more than four pixels. The velocity of the radar pixels is represented by a different color. Depending on the percentage of overlap, the weight of each pixel value is assigned considering that the sum of the weights must represent 100% of the face area. In the case of a face overlapping four pixels:

$$w_{total} = w_1 + w_2 + w_3 + w_4 = 1 \tag{16}$$

Therefore, the velocity value assigned to the triangular mesh face would be given by:

$$V_{face} = V_1 w_1 + V_2 w_2 + V_3 w_3 + V_4 w_4 \tag{17}$$

The method for assigning the radar values to the triangular faces is also used for the edge values, however as multiple faces would overlap with a pixel labeled as an edge, multiple faces would represent the edge. As mentioned before, this is not desired, since this would create a wider edge, and the aim is to generate the edge as thin as possible. For this, only the face with the largest overlap is selected. Then, the centroid of each edge face would give the 3D coordinates *(x,y,z)* to a point. Lastly, at the end of the Geocoding, the two outputs would be, the 3D velocity map projected in the DTM and the 3D point cloud of the edge extracted from the boundary of the unstable area selected by the user.

4.6 Iterative plane fitting

This is the main process of the algorithm since it gives the final output of the planes that could characterize the geological structures involved in the deformation of the slope. The method used in this algorithm is based on the iterative method "Random Sample Consensus" (RANSAC) introduced by Fischler and Bolles (1981) which is a fitting model for data with a large dispersion and number of outliers. The conventional methods such as Least Squares, use the entire set of data to fit a model, instead, RANSAC starts fitting the model to a random small sample, and extends the model to the compatible data points. This method allows fitting planes in linear features in 3D point clouds, and therefore, with some modifications, it allows us to find the linear structures from the 3D edge point cloud extracted from the unstable area selected by the user. It is expected that after running this algorithm, some of the extracted planes will characterize the geological structures involved in the deformation of the slope instability.

The general paradigm of RANSAC, which help us to understand the functioning of the algorithm used in this study is explained by Fischler and Bolles (1981) as follows:

"Given a model that requires a minimum of n data points to instantiate its free parameters and a set of data points P such that the number of points in P is greater than n [$\#(P) \geq n$], randomly select a subset $S1$ of n data points from P and instantiate the model. Use the instantiated model $M1$ to determine the subset $S1*$ of points in P that are within some error tolerance (ϵ) of $M1$. The set $S1*$ is called the consensus set of $S1$.

If # ($S1*$) is greater than some threshold τ, which is a function of the estimate of the number of gross errors in P, use $S1*$ to compute (possibly using least squares) a new model $M1*$.

If # ($S1*$) is less than τ, randomly select a new subset $S2$ and repeat the above process. If, after some predetermined number of trials, no consensus set with τ or more members have been found, either solve the model with the largest consensus set found or terminate in failure."

The main variation done to this method is the selection of the random sample. In this case, the seed is chosen from the spatially pre-clustered 3D edge point cloud, and its selection depends on the relation between the plane extracted for each cluster and the DTM. Therefore the method used is not a random consensus, since the seeds are chosen based on a quantitative assessment.

Fischler and Bolles (1981) define three parameters that must be set to run RANSAC:

- The error tolerance (ϵ) to include a point in $S1*$.
- The maximum number of iterations (m) to select a new subset.
- The threshold (τ). Which sets the minimum points to define a new model $M1*$.

The selection of these parameters and the modification of the RANSAC algorithm for the seed selection will be explained in the following sub-chapters.

4.6.1 Edge K-mean clustering and seed selection

As mentioned above, the selection of the sample of the data i.e. the seed, to initiate the model is not done randomly in this case. This was decided since it is desired to fit the planes in the direction of the edges, not across them. If a random sample is chosen, there is the possibility of selecting points of the 3D point cloud that are on opposite edges of the unstable area, and this would generate a plane almost parallel to the slope of the surface. This is contrary to the scope of this study, which is to model planes that simulate the geological structures that cut the slope of the rock or soil. In terms of plane directions, the normal vector of the plane should be perpendicular to the normal vector of the slope; this can be visualized in Figure 28 where (a) represents a plane extracted from a random seed with points in the opposite edge, while (b) a plane extracted from a seed with its points located in the "same" edge. To solve this problem, the points of the seed should be part of the same edge. Hence, the solution proposed is to cluster the 3D point cloud in k clusters based on their spatial coordinates using the K-means clustering method.

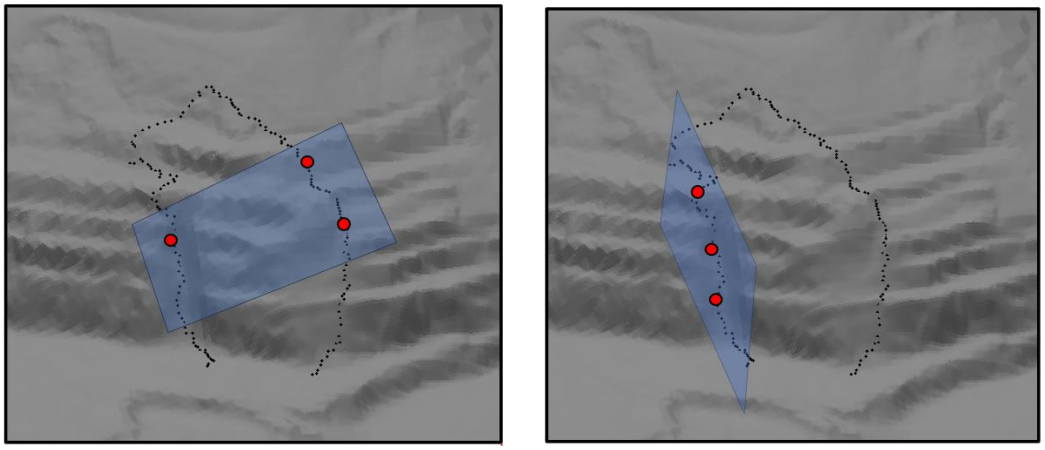

(a) (b)

Figure 28: Scheme of plane extracted from random and opposite points (red points) (a) and extracted from points located in the "same" edge(b).

K-means is a clustering algorithm first introduced by Lloyd (1982). The aim of this method is to partition the members of a given set of observables into k different clusters according to their proximity measured using a certain distance metric (euclidean in this case). The inputs necessary to run this algorithm are the data that will be clustered, the number of desired clusters (k), their respective initial centroids, and the maximum number of iterations. The method proceeds as follows:

1. Each point gets its distance calculated to each cluster centroid.
2. Each point gets assigned to the cluster with the closest centroid.
3. Centroids are re-computed using the new members of the respective cluster.
4. Repeat the previous steps until the positions of the centroids do not change or the maximum number of iterations is reached.

In this case, the Matlab k-means method is employed. To run this method, the number of clusters to segment the point cloud is 10 ($k = 10$). This was decided since it is ideal to divide the edges into small point clouds with ideally no curvature and mostly a linear structure. After some trials, it was tested that if the number of clusters is greater than $k = 10$ the segments would be too small to extract a representative first model i.e. plane, and if k is smaller than 10 the points in the cluster will be more curved in the

space. Additionally, the number of maximum iterations set is 1000. As an example, the K-means clustering with $k = 10$ would result as following:

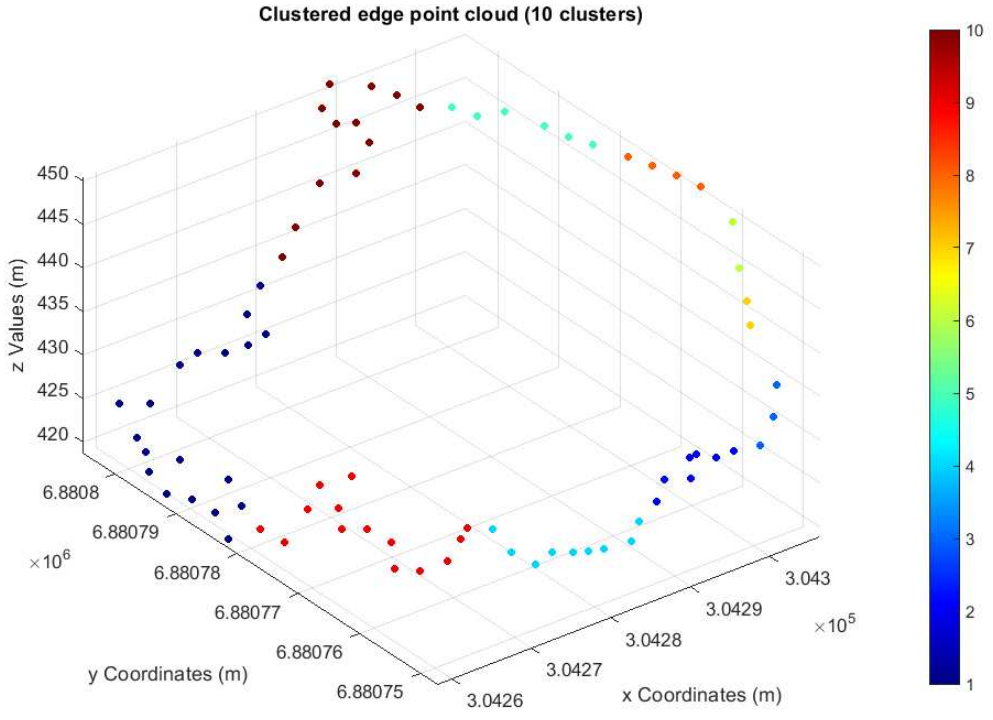

Figure 29: Edge 3D point cloud segmented in $k = 10$ clusters.

After the edge segmentation, the seed can be chosen, however, the seed selection is not random. As the aim of the algorithm is to extract planes that cut the topography, the process of choosing the first seed to initiate the model is very relevant. The method to decide quantitatively which seed is the best one to start the model begins using Least Squares to fit a plane for each cluster with a modified function based on *affine_fit* developed by Adrien Leygue (2014); thus, 10 planes would be created. The idea is to force the model to start with a plane that "cuts" the surface, this means that the normal vector of the plane should be as perpendicular as possible to the normal vector of the slope, to simulate the geological structures that cut the slope such as fractures and faults. The normal vector to the slope is calculated by selecting, for each k cluster, the triangular faces of the DTM that were used to extract the 3D coordinates of the points of the cluster, thus for a k cluster a total of l faces is taken. Then, the normal

vector of each face is extracted to finally average their components (x, y, z) on the total number of faces (l). Thus, the resultant vector would be the average normal unitary vector of the topography for each k cluster as follows:

$$\hat{n}_{ktopo} = \left(\frac{\sum_{i=1}^{l} x_{ki}}{l}, \frac{\sum_{i=1}^{l} y_{ki}}{l}, \frac{\sum_{i=1}^{l} z_{ki}}{l} \right) \tag{18}$$

Then, the plane whose normal vector ($\hat{n}_{kplane}$) has the smallest dot product with the normal vector of its correspondent topography average normal vector is the ideal seed:

$$Seed = Cluster_k = min(\hat{n}_{ktopo} \cdot \hat{n}_{kplane}) \tag{19}$$

This would be the point set that generates the plane with the most perpendicular direction possible to the surface. In the case of the example of Figure 29, the least suitable plane would be the one generated in Figure 30a while the best plane is generated in Figure 30b:

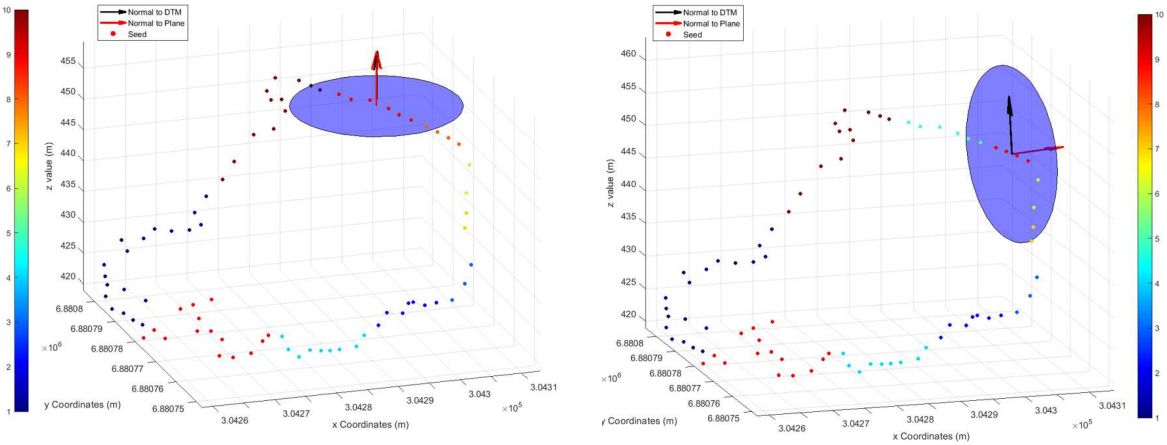

(a) (b)

Figure 30: Example of a bad seed (a) and ideal seed (b).

This process is the main difference from the traditional RANSAC method since the seed selection is not random and it depends quantitatively on the characteristics of the edge point cloud and its relation with the topography. After the seed is selected, the first model of the linear fitting can be initiated.

4.6.2 Model parameters

Using a modified version of the MATLAB function *affine_fit* (Adrien Leygue 2014), which is based on the Least Square method, the following parameters of the plane extracted from the first seed are obtained:

- The three eigenvectors ($\hat{\lambda}_1$, $\hat{\lambda}_2$, $\hat{\lambda}_3$) that represent the three principal components of the 3D coordinates of the selected point cloud. These unit vectors are given according to the variance, and with them, the plane can be extracted. The direction with the smaller variance will define the vector normal to the plane ($\hat{\lambda}_3$), while the other two components give the direction of the axis of the plane growth (in-plane vectors), where $\hat{\lambda}_1$ defines the direction of the largest variance, and $\hat{\lambda}_2$ gives the second direction for the growth of the plane.

- The mean of each direction of the 3D coordinates of the seed (μ_x, μ_y, μ_z), defining the central point of the plane (p).

$$\vec{p} = (\mu_x, \mu_y, \mu_z)$$

- The standard deviation, of the points included in the plane model, in the direction of the three eigenvectors: normal to the plane (σ_3), principal axis (σ_1) and secondary axis (σ_2).

Using these parameters the iterative model can be initiated. Following the analogy with RANSAC, and as mentioned previously and defined by Fischler and Bolles (1981), the model parameters would be:

- The error tolerance (ϵ) to include a point in the model. It depends on the three directions of the plane and it is defined as:

$$\epsilon_1 = 4\ \sigma_1, \quad \epsilon_2 = 3\ \sigma_2, \quad \epsilon_3 = 3\ \sigma_3$$

  The coefficient in the principal axis (σ_1) is greater than in the other directions because it represents the largest variance of the data, which means that is the direction that follows the edge, and therefore it should be able to include more points to the model.

- The maximum number of iterations (m) to select a new subset is set to 100.
- The threshold τ which sets the minimum points to define a new model, is $\tau = 3$. If the seed contains less than this value it is not considered and another sample would be chosen, following the same quantitative selection done for the first seed.
- An extra parameter β is added to this fitting model. It refers to the minimum number of points left to continue the seed selection. Which is defined as the 5% of the total number (N) of points in P ($\beta = 0.05N$). If the number of remaining points that have not been assigned to a model is smaller than β the entire process will stop.

4.6.3 General algorithm

After the explanation of the seed selection and the parameters used in the model, the general algorithm can be described. A summary of it is shown in the flowchart shown in Figure 31. In general, two loops are used to extract the final planes, the main loop with iterations j and the inner loop with iterations i. In i multiple plane models are tested for a single seed S_j. , then in j the final stable plane extracted in i will be stored and a new seed will be selected until all the points in the point cloud are used or until the condition β is met.

The model begins with two inputs, the first seed selected with the procedure mentioned in the previous chapter ($S_{j=1}$), and the 3D point cloud of the extracted edge (P). It is worth highlighting that P includes S_1 and it contains the total number (N) of the points labeled as edges. Thus, the model starts with a matrix of 3D points $P = (P_{nf})$, where n is defined by the total number of points as $n = 1, 2, 3, ...N$ and each direction in space is represented by $f = 1, 2, 3$. A single 3D point in the matrix is represented by P_n. Using the two inputs, the process can be initiated with the following steps, starting with $j = 1$ and $i = 1$:

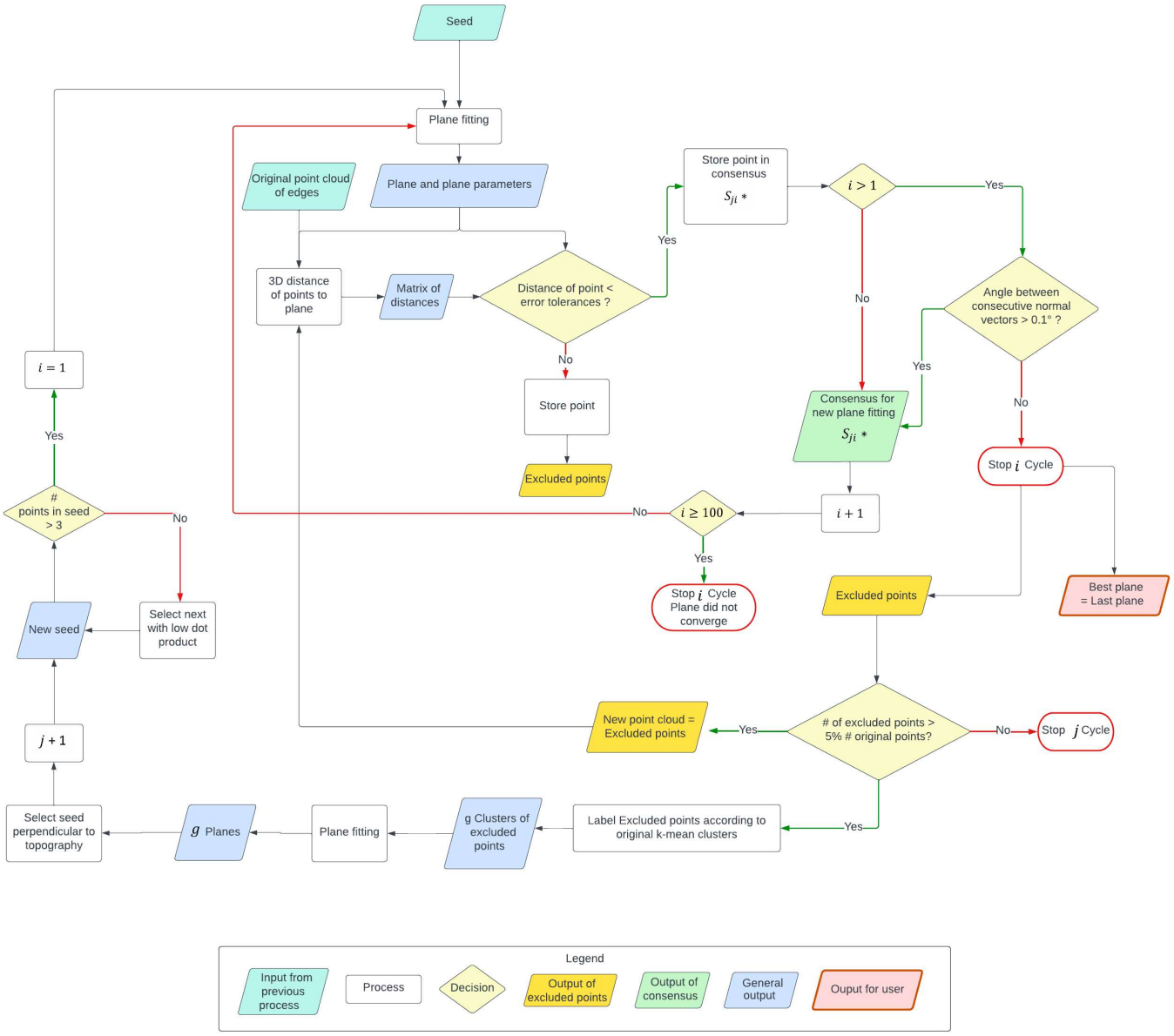

Figure 31: Flow chart of the iterative algorithm for plane fitting.

1. A plane (M_i) is modeled from the points in the seed $S_j = 1$ using Least squares (*affine_fit*) . The plane parameters are extracted, including the error tolerance in each direction (ϵ_{fi}), the eigenvectors ($\hat{\lambda}_{fi}$), and the centroid of the plane $\vec{pi}$.

2. Using these parameters, the distances in each direction of the point cloud P to the plane M_i are calculated ($\vec{d_{fni}}$).

3. The distance of each point P_n ($\vec{d_{fni}}$) is compared against the error tolerance (ϵ_{fi}). If the distance ($\vec{d_{fni}}$) is smaller or equal to the tolerance, the point P_n will be

included in the consensus of S_j, thus stored in $S_{ji}*$. This consensus $S_{ji}*$ will contain all the points P_n that fit inside the error tolerance of the modeled plane (M_i) and will exclude all the points that exceed this value in each iteration i. Meanwhile, the excluded points in each iteration will be stored in D_{ji}.

4. Steps 1 to 3 are repeated for every consensus S_{ji*}, increasing i in each iteration and adding points to $S_{ji}*$ and to the excluded set D_{ji}.

5. Iterations i will finalize if the condition of the maximum number of iterations (m) is met. However, another condition is also used to stop the model. It is expected, that after a number of iterations i, the plane becomes stable, which means that the normal vector stops changing ($\hat{\lambda}_3$), this vector is compared between consecutive planes using the dot product. The model stops when the angle between the normal vectors falls below 0.1°, following this condition:

$$\hat{\lambda}_{3i} \cdot \hat{\lambda}_{3(i-1)} \geq \cos(0.1) \tag{20}$$

6. When i stops, the final plane M_i is the most suitable model for the final consensus S_{j*}, thus in the outer cycle j the final plane would be stored as $H_j = M_i$, and the final set of excluded points as $E_j = D_{ji}$ where the total number of points in E_j is X.

7. After using the points of the consensus S_{j*} to build a plane, the available points to fit a new model would be the previously excluded points E_j, with a number of points X and from them a new seed is chosen. The selection of the new seed uses the same procedure as the selection of S_1. The k clusters extracted using the K-means method are related to E_j, which means these points will be labeled according to the k cluster to which they originally belonged. As the number of available points X is less than the number of original points N, some of the original clusters, labeled from 1 to 10, do not exist anymore. For example, if all the points in cluster 3 were included in the previous consensus S_j*, the label $k = 3$ will not be related to the points in E_j. Thus, the remaining number of clusters that will be related to the excluded points E_j will be g clusters, and after

each cycle j it is expected that $g < k$. A plane is fitted to each cluster related to the available points E_j resulting in g planes.

8. As in the selection of the first seed S_1, the cluster g that generated the most perpendicular plane to the topography will be selected as the new seed S_j. Considering the parameter τ, the new seed should have more than 3 points to be chosen, if it contains fewer points the next-best seed is selected, which means the cluster with the next lowest dot product of the mentioned vectors.

9. With the new seed S_j the iterations in i will start again from step 1 to step 4. But instead of using the original point cloud P to calculate the distance to generated planes, the excluded points in the previous cycle E_{j-1} will be used. Thus a point P_n will belong to E_{j-1} and $n = 1, 2, ..X$. Iterations j will stop in step 4 if, according to the parameter β, the condition $X < 0.1N$ is met.

At the end of this iterative process, j planes will be extracted from the edges of the unstable area selected by the user. The ideal scenario is that these planes follow the linear features of the edges and represent, as closely as possible, the geological structures such as the fractures or faults, that are causing the displacement of the mass.

5 Cases of study

5.1 Cumba Slope Failure

The following information summarizes the findings reported in the study by Bar et al. (2023) or were provided directly by the authors. The Cumba Slope Failure occurred in the Pueblo Viejo gold mine located in Santo Domingo, Republica Dominicana, in September 2019 when the northern wall failed progressively over a period of three weeks. The material of the mass movement was andesite in a slope with a dip and dip direction of 41°/ 205° (pre-failure). The rocks of this area are affected by the Hatillo Thrust Fault (HTF), a regional structure with dip directions ranging from 200° to 225° and a dip angle of about 30°.

Figure 32: Photograph of Cumba Failure (Looking North-West, October 2019). Taken from: Bar et al. (2023)

A back-analysis was conducted using aerial photogrammetry, GB-SAR, 3D limit-equilibrium (LEM) and finite element modeling (FEM). The photogrammetry was done using multiple historical (pre-failure) aerial images taken with a single direction

from a nadir look at a high altitude, with a resolution of 8 cm per pixel (medium resolution). From this, several 3D models were generated and later used to map discontinuities from which only the ones with a length greater than 10 m were selected, a threshold set manually by the experts. Consequently, six faults (Figure 33) were extracted from the resultant 3D models with the following directions:

Fault	Dip	Dip direction	Color
190916-a	51°	225°	Purple
190916-b	82°	259°	Black
190916-c	50°	164°	Orange
190923-a	42°	215°	Blue
190923-d	62°	167°	Red
190923-e	64°	177°	Yellow
Slope (pre-failure)	41°	205°	

Table 2: Average dip and dip direction of the extracted faults from the 3D model. The slope values are written for reference.

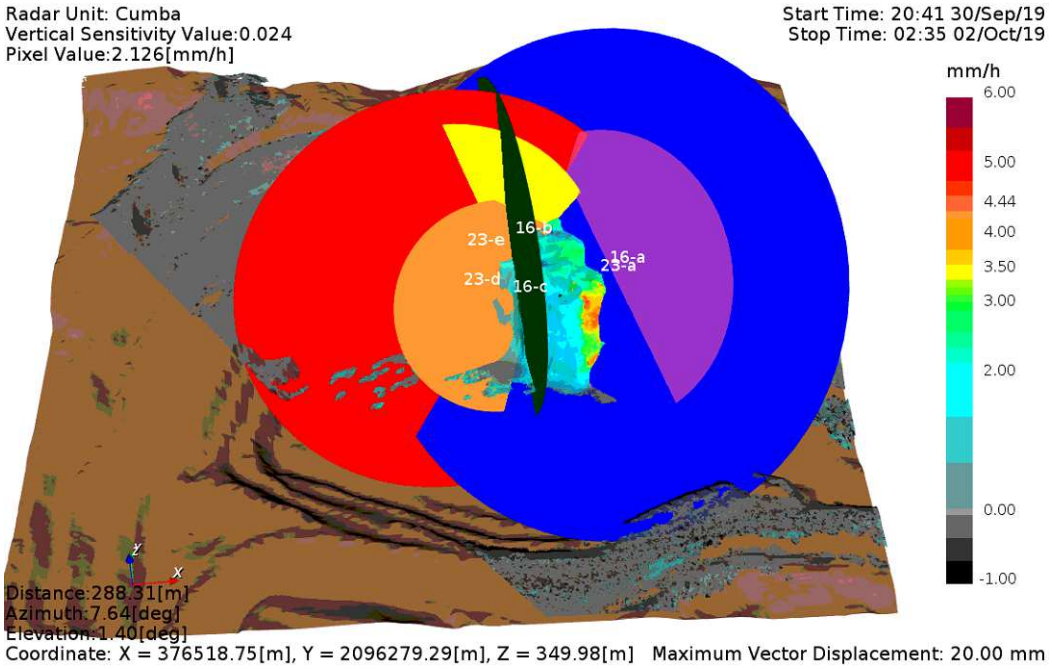

Figure 33: Faults extracted from the 3D photogrammetry model overlapping the velocity map. Positive velocity values are approaching the sensor.

From the mapped faults, the yellow, blue and red faults are considered the main structures involved in the slope instability:

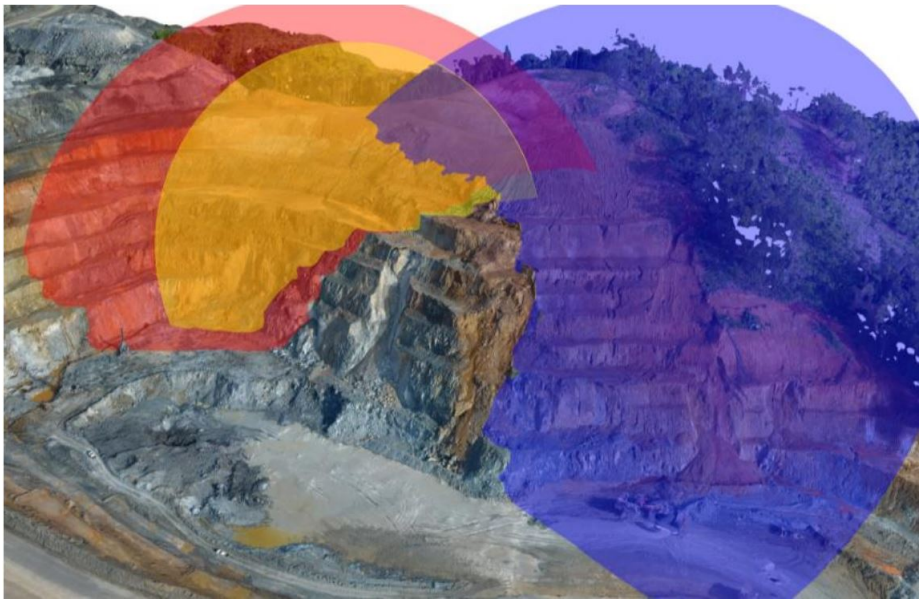

Figure 34: Faults extracted from the 3D photogrammetry model. Taken from: Bar et al. (2023)

According to the results reported, the blue fault is the principal structure in the slope instability since it determines the sliding mechanism. It has a similar direction as the regional HTF feature, but it is intersected by the yellow and the red faults. A kinematic analysis was conducted using these three faults and the slope information, obtaining the classification of the failure mechanism as a planar sliding on the blue fault with a non-daylighting condition (the dip of the fault has a greater or equal angle than the dip of the slope). It can also possibly form a non-daylighting wedge considering the truncation of the red and yellow fault.

After classifying the failure mechanism, the mapped structures found in Table 2, were used as input for the 3D LEM analysis. From this, the Factor of Safety (FoS) along the multiple slip surfaces was estimated, and as shown in Figure 35, it was determined that the main slip occurred in the blue and red faults, with the lowest FoS (in yellow):

Figure 35: FoS from 3D LEM back-analysis. Taken from: Bar et al. (2023)

The results from the 3D LEM analysis were used to extract the shear strength of the red and blue faults to be used in the 3D FEM analysis along with other mechanical properties of the andesite. The resultant model of the 3D FEM analysis validated that the displacement was bounded by the red and blue faults, as shown in Figure 36:

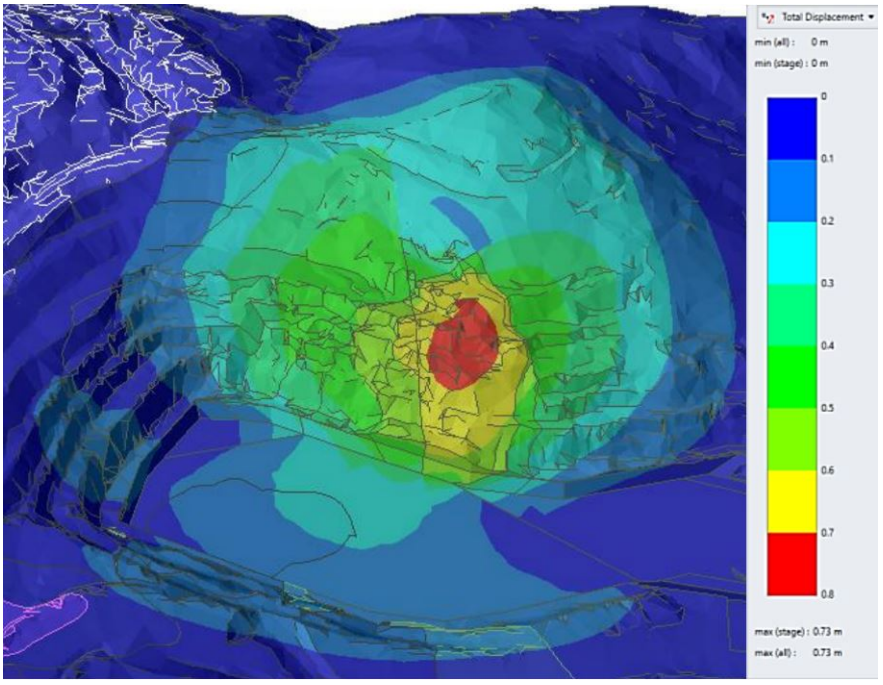

Figure 36: Displacement from 3D FEM analysis. Taken from: Bar et al. (2023)

These results were verified using the displacement calculated from the ArcSAR interferometry in which, during failure, a displacement of about 9 meters was recorded along the blue fault in the direction of the LoS:

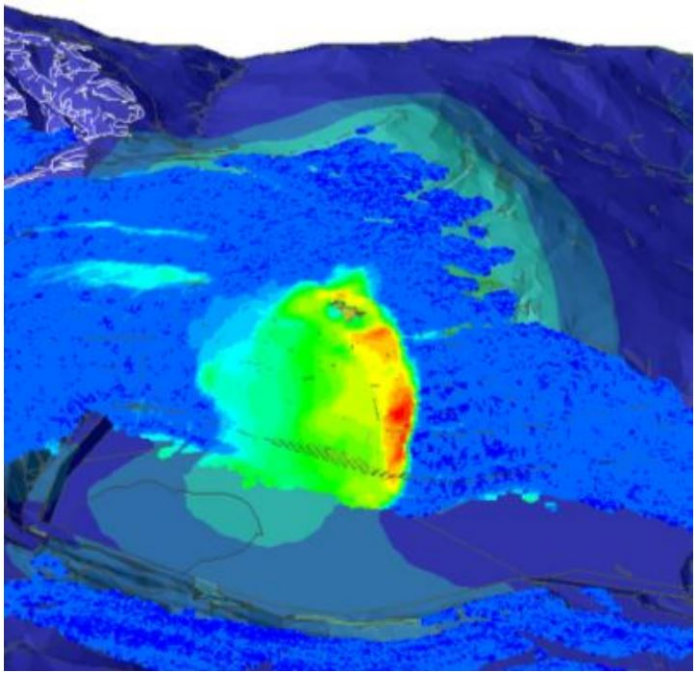

Figure 37: Displacement from ArcSAR interferometry (blue indicates < 100 mm displacement and red indicates $> 9,000$ mm displacement). Taken from: Bar et al. (2023)

5.1.1 Acquisition of radar images and extraction of velocity map

The Cumba pit was monitored using the ArcSAR radar and the software Guardian of the company IDSGeoradar. The device was set on the southern wall at a distance of about 277.5 m from the slope instability face with a LoS direction of 345.89° (from the North) as shown in Figure 38, where the amplitude of the signal received by the radar is overlapping the DTM. The band used was the K_u band with a central wavelength (λ) of 17.43 mm. The two radar images selected for the extraction of the geological structures were acquired with a time difference of *33* hours, starting from the 30-September-2019 at 20:41:11 (hh:mm:ss) to the 02-October-2019 at 05:40:58. This is a post-failure period and it was selected due to the availability of data.

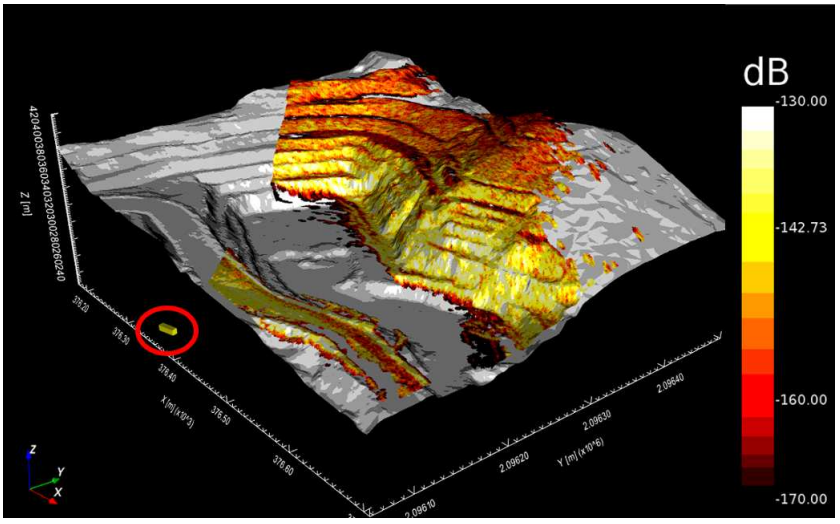

Figure 38: Map of radar amplitude overlapping the DTM (white) of the area of study. The ArcSAR instrument is highlighted in red.

A radar image of the start date and one of the end date were used as input for the interferometry process to extract the differential unwrapped phase. Using the equation 10 the displacement map was calculated from the differential phase map to finally extract the 2D velocity map. The filtered velocity map shown in Figure 39d, was used as the input for the velocity threshold clustering.

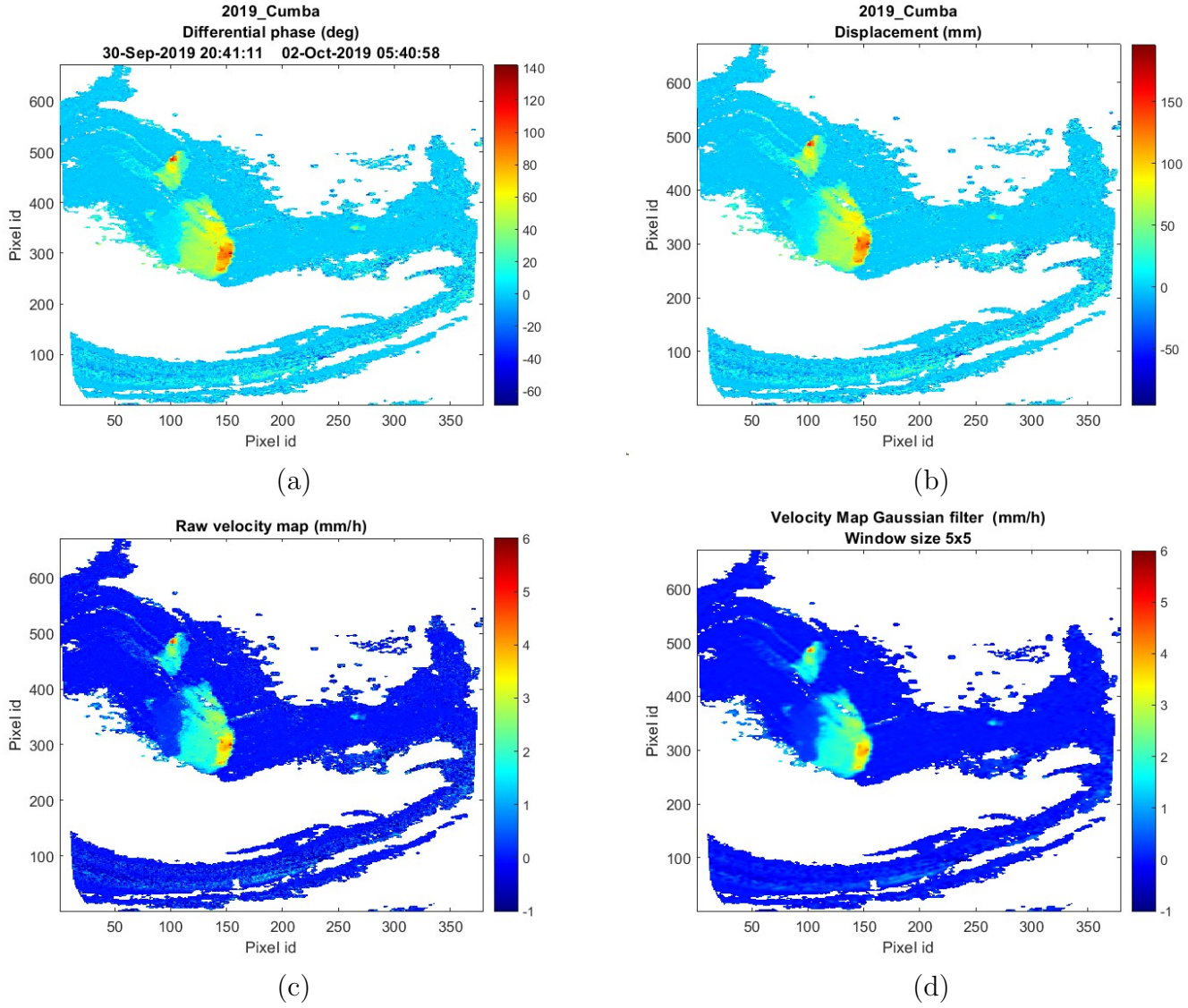

Figure 39: (a) Differential Phase map in degrees. (b) Displacement map (c) Raw velocity map and (d) velocity map after Gaussian filtering. Positive values are approaching the sensor.

5.1.2 Velocity threshold clustering and edge detection

In this case, the area between the planes shown in Figure 34 was selected with a click to perform the velocity threshold clustering. The selection was done as displayed in Figure 40a. From this, the final velocity threshold (V_{thf}) was computed, resulting in a velocity of $0.658\,91\,\mathrm{mm\,h^{-1}}$. Using this value the unstable area shown in Figure 40c was clustered. After this, the clustered 2D map was used as input for the binary edge detection algorithm. The output of this process is the 2D point-set of the unstable

area shown in red in Figure 40d.

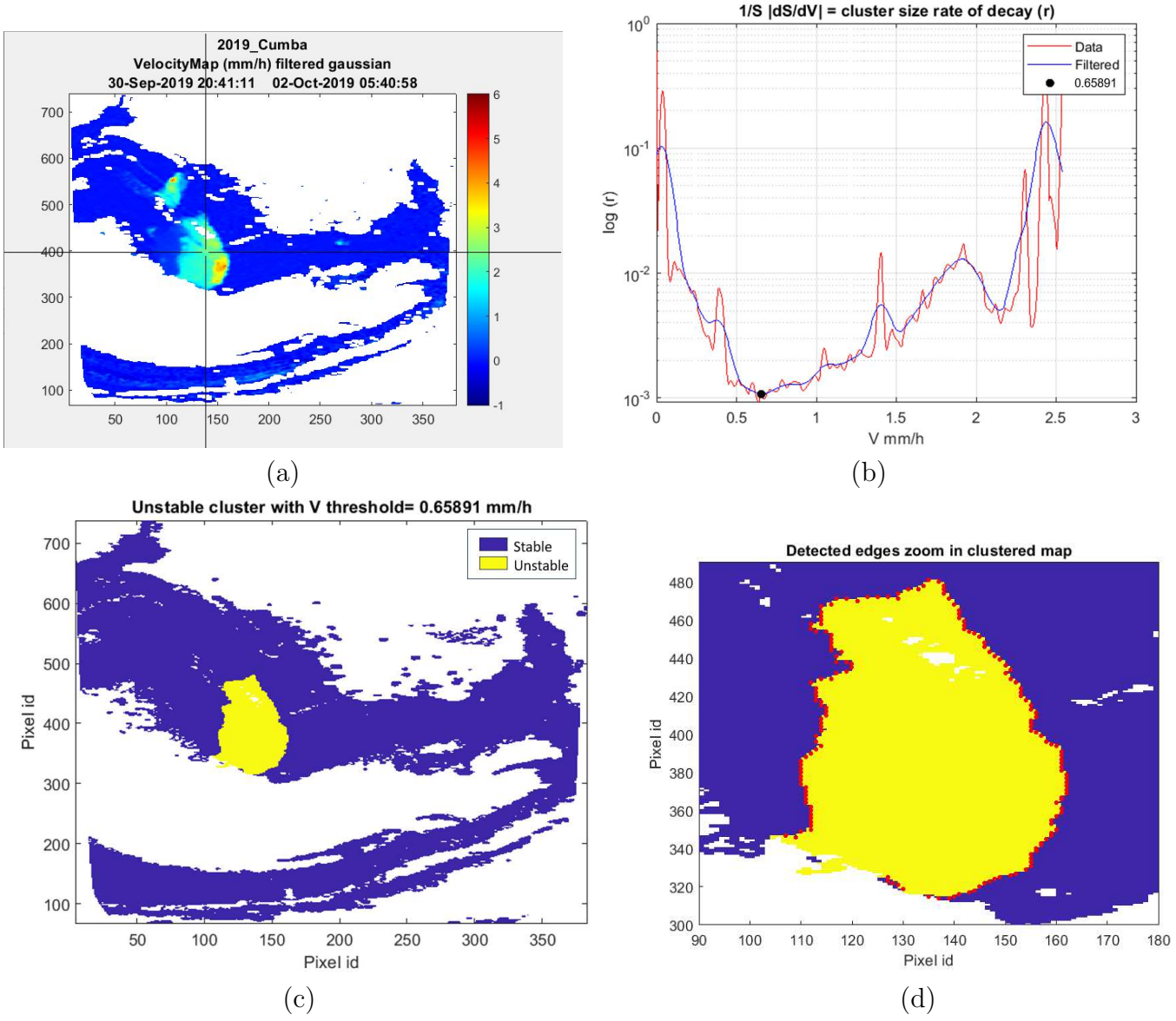

Figure 40: (a) Pixel selected by the user. (b) r rate giving the velocity threshold (c) 2D clustered velocity map (d) Edge detected on the 2D clustered velocity map (Zoom of c). Positive velocity values are approaching the sensor.

The extracted edges were compared on both the raw velocity map and the filtered velocity map, as the velocity clustering was carried out using only the filtered velocity map. (Figure 41). This enabled the verification of the Gaussian filter's effectiveness in smoothing the original data without excessive blurring of the boundaries, ultimately resulting in the accurate placement of the extracted edges.

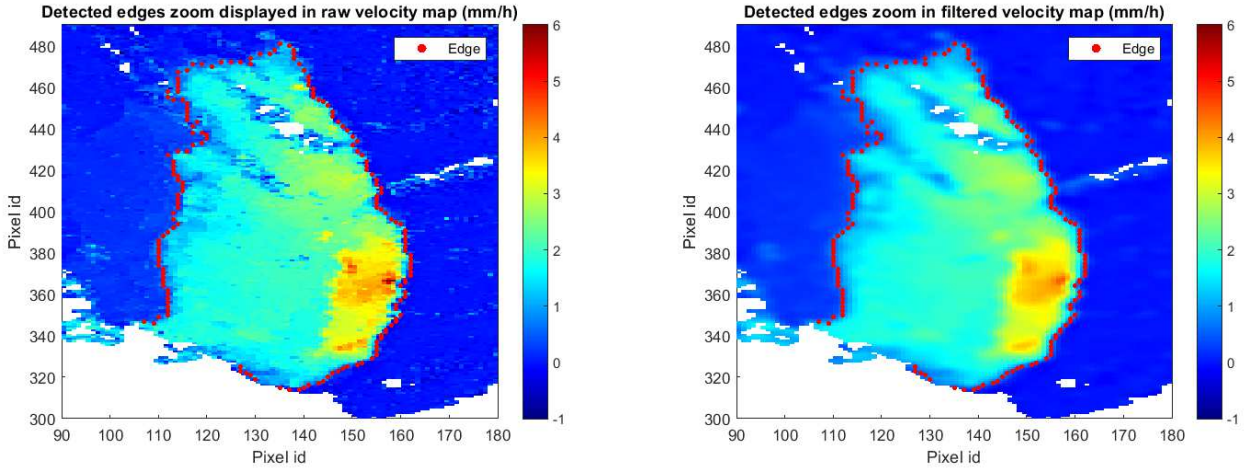

(a) (b)

Figure 41: (a) Edges overlaying the raw velocity map.(b) Edges overlaying the filtered velocity map. Positive values are approaching the sensor.

5.1.3 Geocoding, edge clustering and seed selection

To transform the acquired 2D data into a 3D format, the initial Digital Terrain Model (DTM), which was originally in a grid format with a cell size of 0.88 m, was converted into a triangular mesh format. Using the DTM in the new format, the 2D filtered velocity map and the 2D point set of the extracted edges were geocoded converting them to 3D data as illustrated in Figure 42:

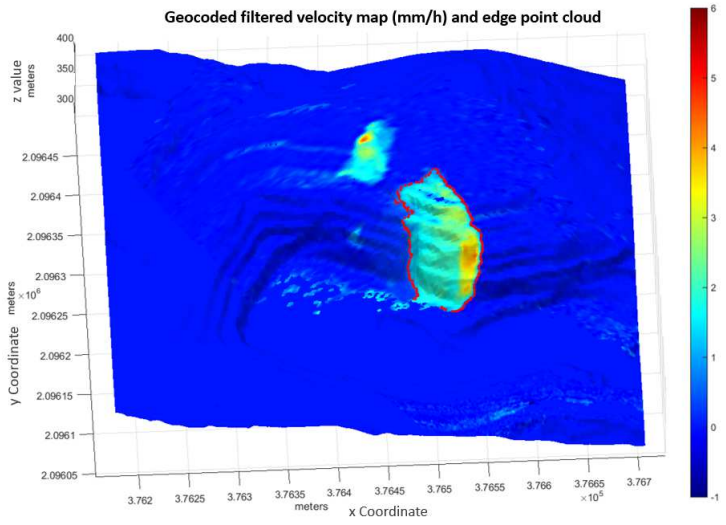

Figure 42: Filtered velocity map and point cloud overlaying the DTM after geocoding.

In accordance with the flow chart of Figure 9, the 3D point cloud of the extracted edges is used as input for the K-means clustering. From this, the point cloud is segmented into 10 clusters (Figure 43a). Then, a plane was fitted for each cluster to select the seed to start the iterative plane fitting algorithm. As shown in Figure 43b the final seed corresponds to the cluster that generated the most perpendicular plane with respect to the surface.

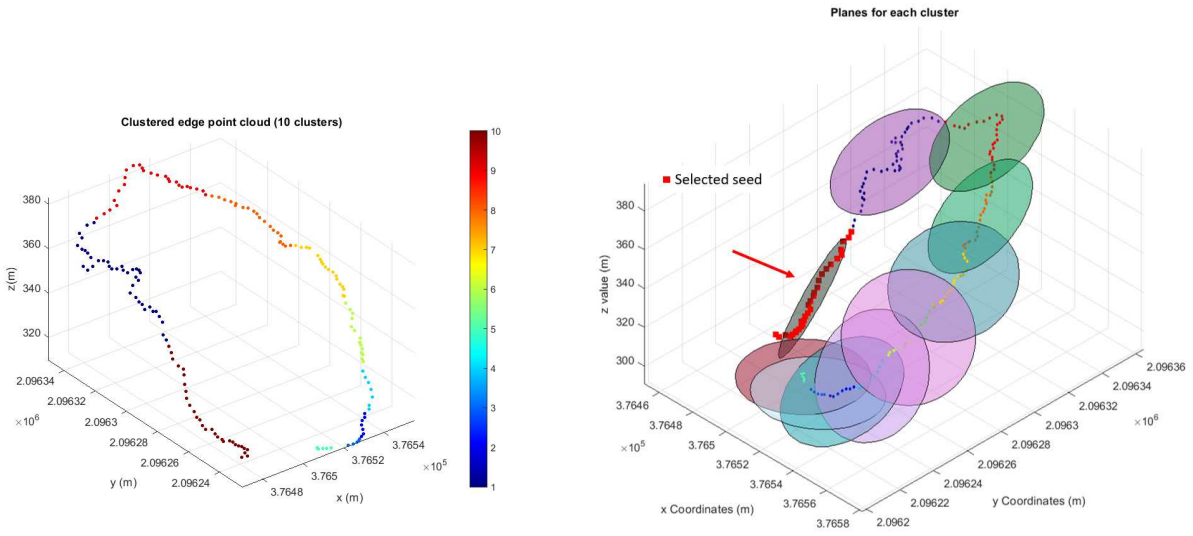

(a) (b)

Figure 43: (a) Clustered edge point cloud.(b) Planes fitted to each cluster. The red arrow points to the selected seed.

5.1.4 Iterative plane fitting results

With the edge point cloud and the selected seed point cloud shown in Figure 43a and b respectively, the iterative process described in the flow chart of Figure 31 was initiated. After running this algorithm, two planes in total were extracted. In Figure 44 the red points are the final consensus of each plane iteration, this means that is the final point cloud that generated the plane. Each plane is defined by the three vectors $\hat{\lambda_1}$ (blue), $\hat{\lambda_2}$ (red) and $\hat{\lambda_3}$ (black) with an amplitude corresponding to their final tolerance (ϵ). Ultimately, the dip direction vector, labeled as "Dip Dir" and displayed in cyan is extracted by following the direction of the steepest inclination of the plane concerning a horizontal plane. The values of the dip angle, dip direction, and number of iterations for each plane are shown in Table 3.

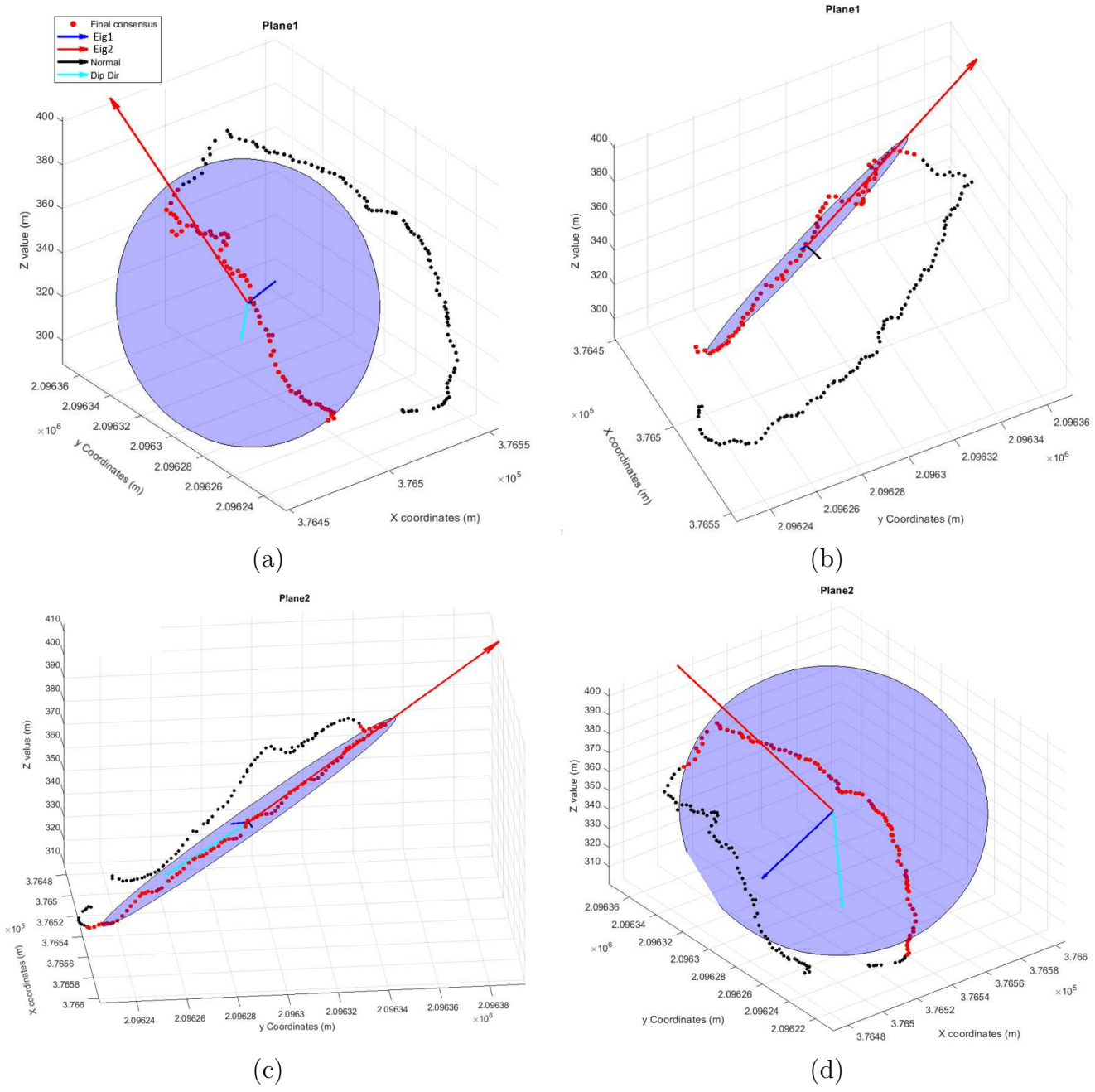

Figure 44: (a)(b) Different views of Plane 1. (c)(d) Different views of Plane 2.

Plane	**Dip angle**	**Dip direction**	**Iterations**
Plane 1	66°	244°	7
Plane 2	39°	211°	15

Table 3: Planes structural information

These two planes were saved in *.xyz* format and imported to the software Guardian to be displayed interactively in 3D along with the edge 3D point cloud.

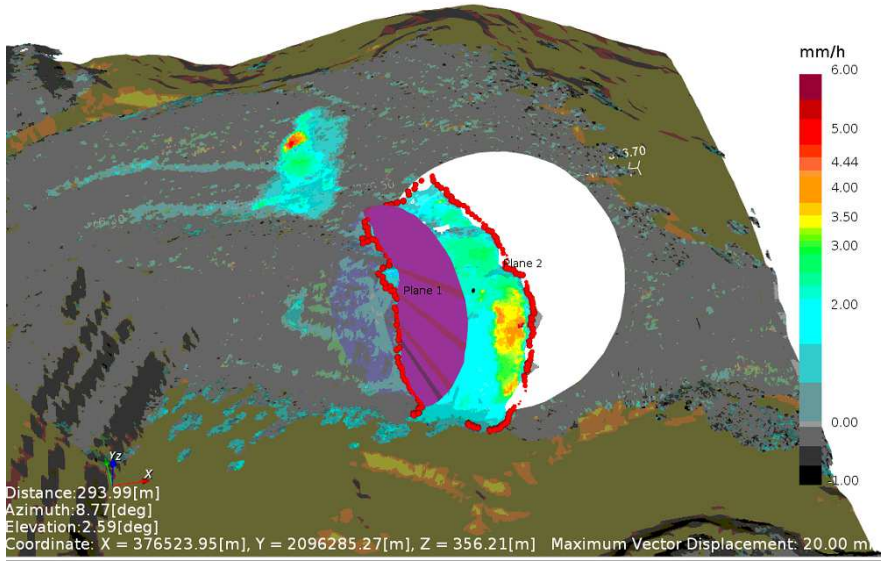

(a)

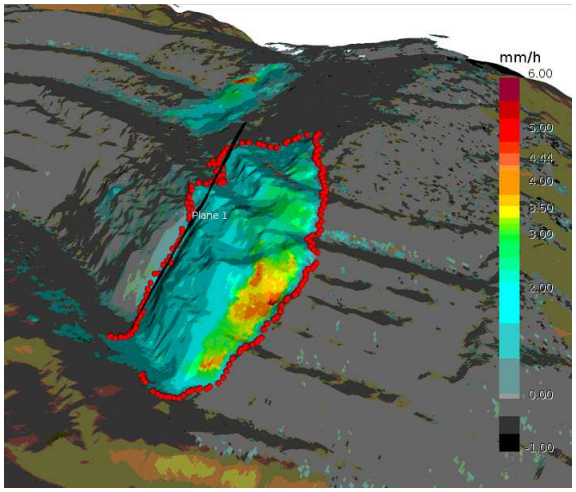

(b)

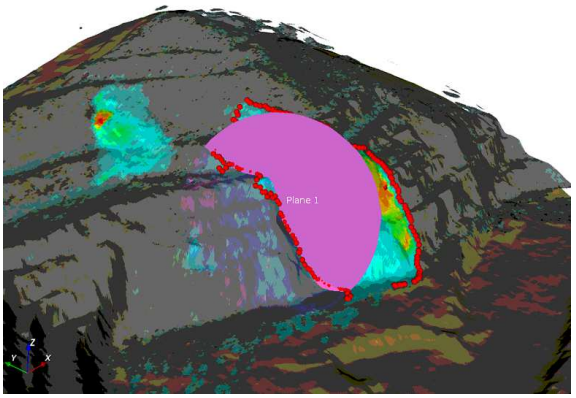

(c)

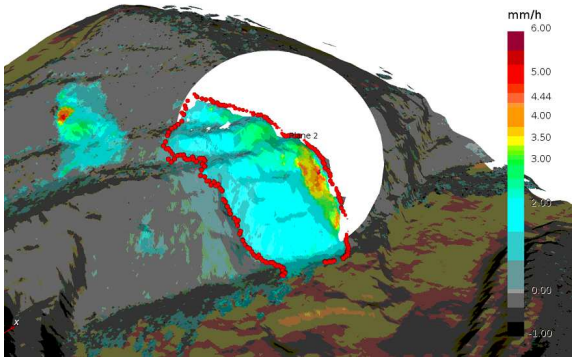

(d)

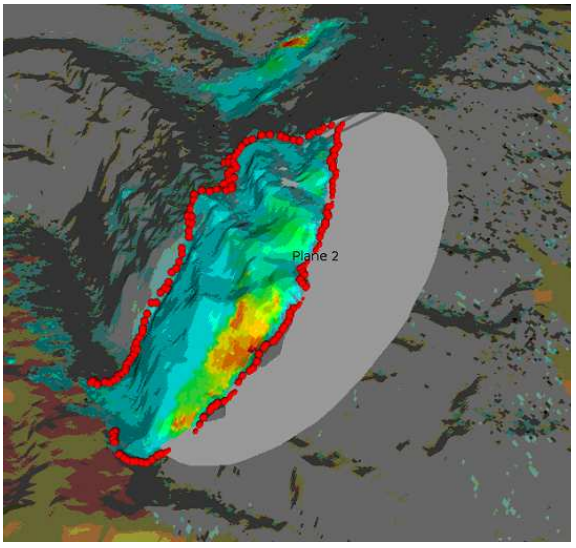

(e)

Figure 45: (a) Planes extracted with the iterative plane fitting displayed in Guardian. View of Plane 1 (b) East and (c) West. View of Plane 2 (d) West and (c) East. Positive velocity values are approaching the sensor

5.2 Montana open pit

In this particular case study, no information regarding the failure surfaces contributing to the slope instability is available due to company confidentiality restrictions. Consequently, only the results obtained through the proposed algorithm will be presented. The processing steps and parameters were the same as the ones used in the previous case of study.

5.2.1 Acquisition of radar images and extraction of velocity map

The Montana pit was monitored using the ArcSAR radar and the software Guardian of the company IDSGeoradar. The device was set on the northern wall at a distance of about 480 m from the slope instability face as shown in Figure 46, where the amplitude of the signal received by the radar overlaps the DTM. The band used was the K_u band with a central wavelength (λ) of 17.43 mm. The radar images selected for the extraction of the geological structures were with a time difference of 122.7 hours starting from 27-October-2022 at 04:37:56 (hh:mm:ss) to 01-November-2022 at 07:20:27.

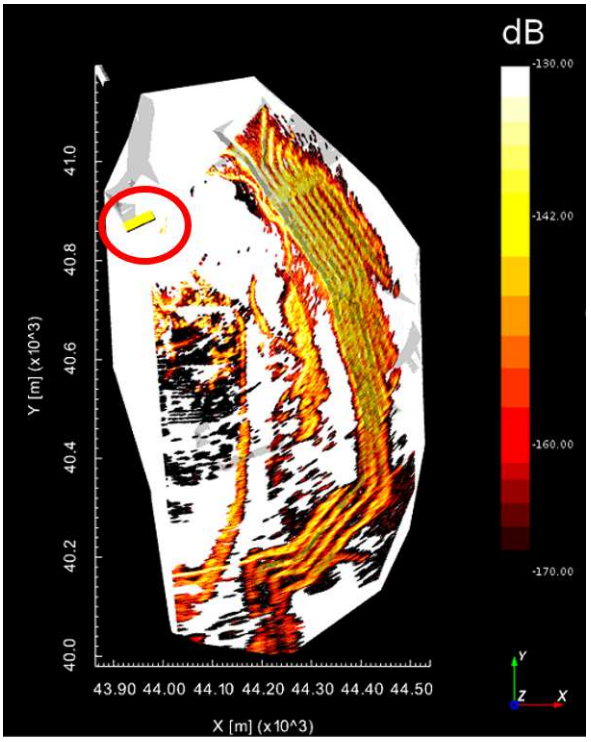

Figure 46: Map of radar amplitude overlapping the DTM (white) of the area of study. The ArcSAR instrument is highlighted in red.

The results of the interferometry between the two mentioned dates are shown in the following figure, where the final output is the filtered velocity 2D map (Figure 47d):

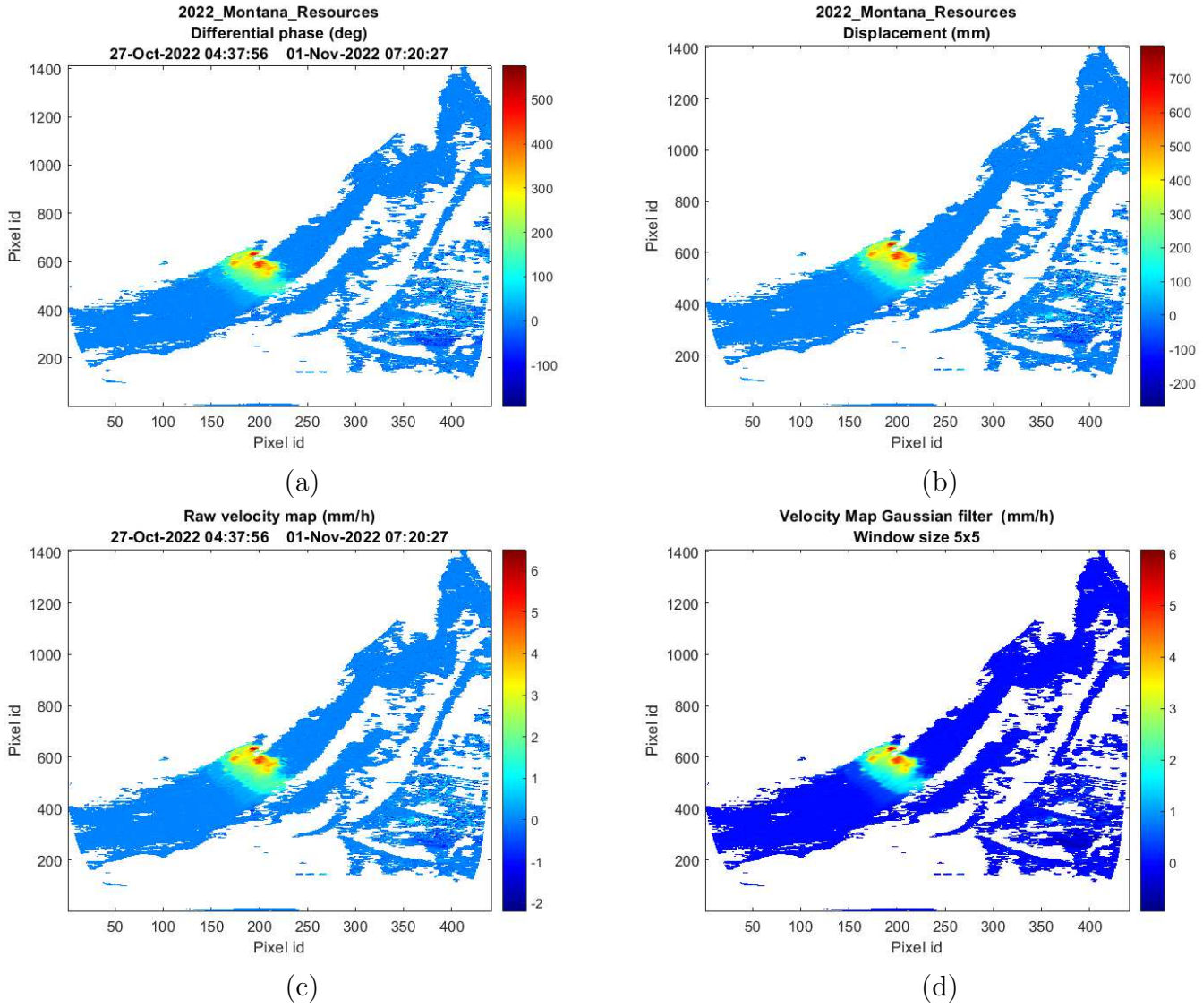

Figure 47: (a) Differential Phase map in degrees. (b) Displacement map (c) Raw velocity map and (d) velocity map after Gaussian filtering.

5.2.2 Velocity threshold clustering and edge detection

The result of the velocity clustering, using as input the final filtered 2D velocity map shown in Figure 47d, is a velocity threshold of $0.79\,\mathrm{mm\,h^{-1}}$ which generated the clustering of the unstable area selected by the user depicted in Figure 48c. Using this clustered map as input for the binary edge detection, the edge displayed in Figure 48d was extracted.

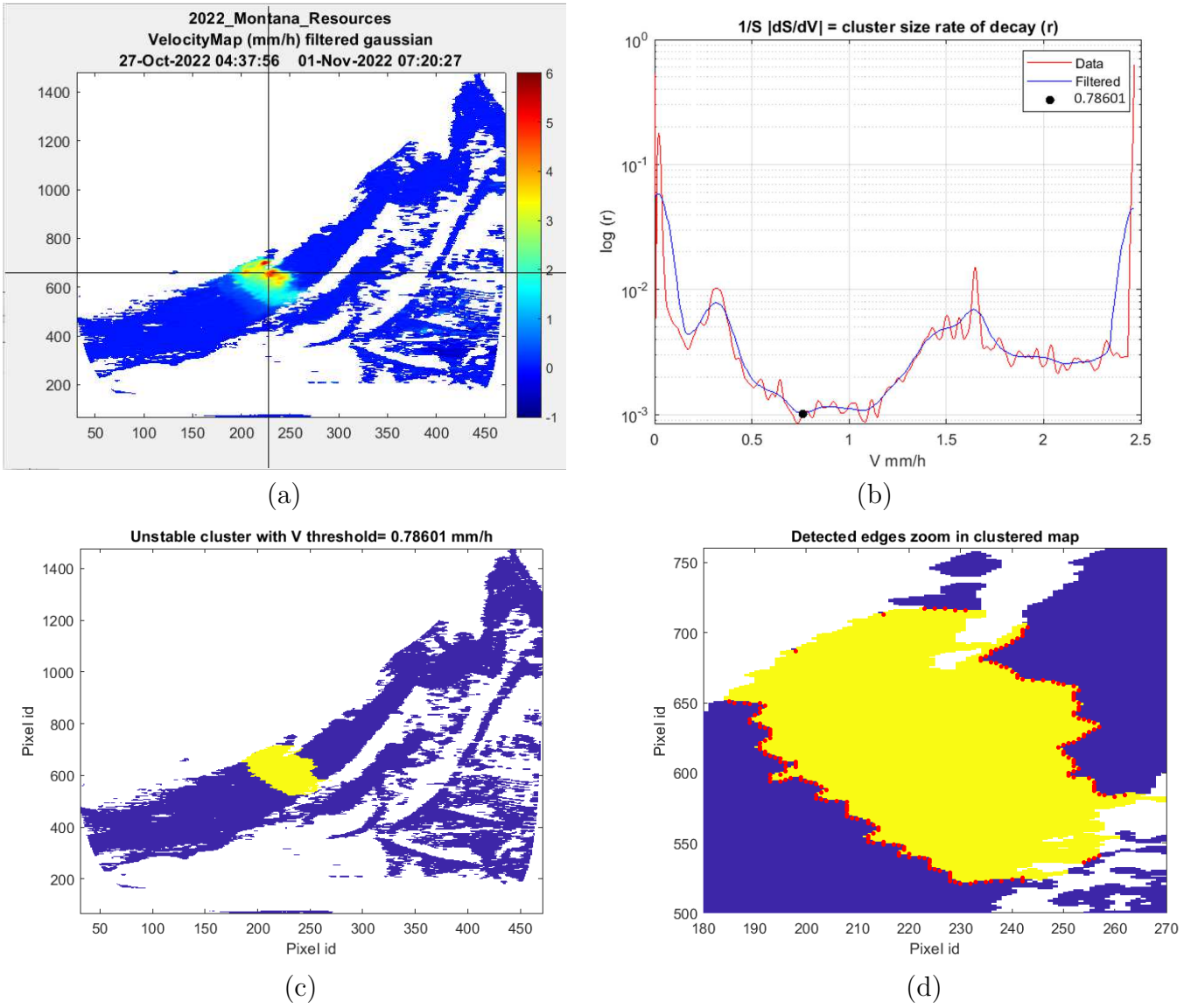

Figure 48: (a) Pixel selected by the user. (b) r rate giving the velocity threshold (c) 2D clustered velocity map (d) Edge detected on the 2D clustered velocity map (Zoom of c).

To validate the filtering and the clustering of the velocity map, the extracted edge was displayed in the raw velocity map and in the filtered velocity map (Figure 49a and b). This confirms that the Gaussian filter and the semi-automatic velocity clustering were appropriate for the delimitation of the unstable area in the Montana open pit.

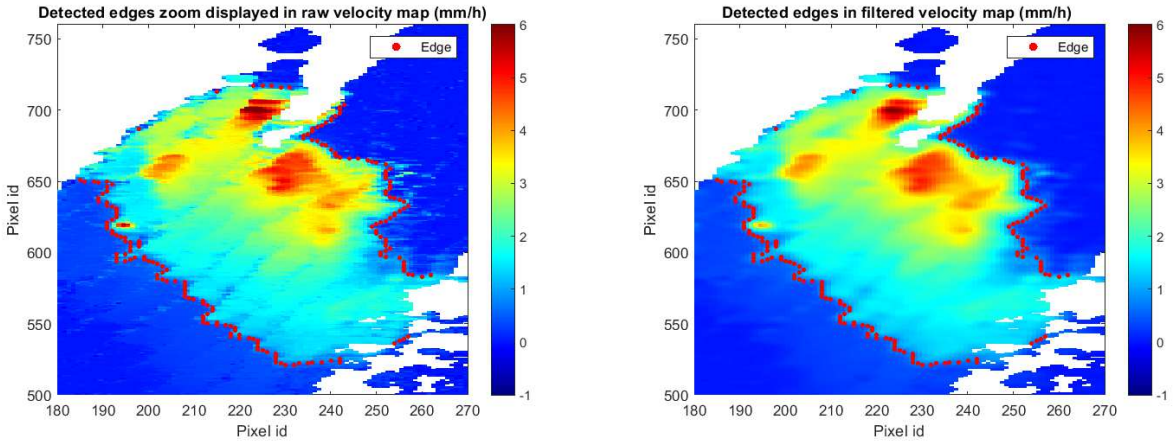

(a) (b)

Figure 49: (a) Extracted edge on the raw velocity map and on the filtered map (b).

5.2.3 Geocoding, edge clustering and seed selection

For the geocoding of the 2D edge pointset and velocity map a DTM originally in a grid format, with a cell size of 1.5 m, was transformed to a triangular mesh. Having the triangular mesh the geocoded was run, obtaining the 3D velocity map and edge point cloud.

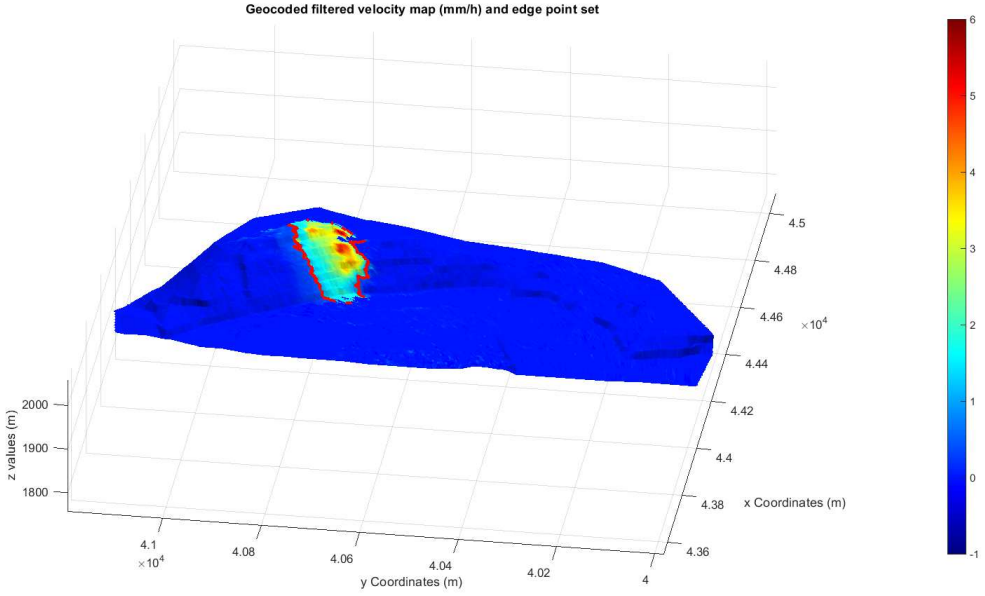

Figure 50: Filtered velocity map and point set of edges geocoded on the triangular DTM. Positive values are approaching the sensor.

The 3D point cloud of the detected edge was clustered as mentioned in chapter 4, resulting in 10 clusters of 3D points. The plane fitting of each cluster and the selection of the best seed are shown in Figure 51b.

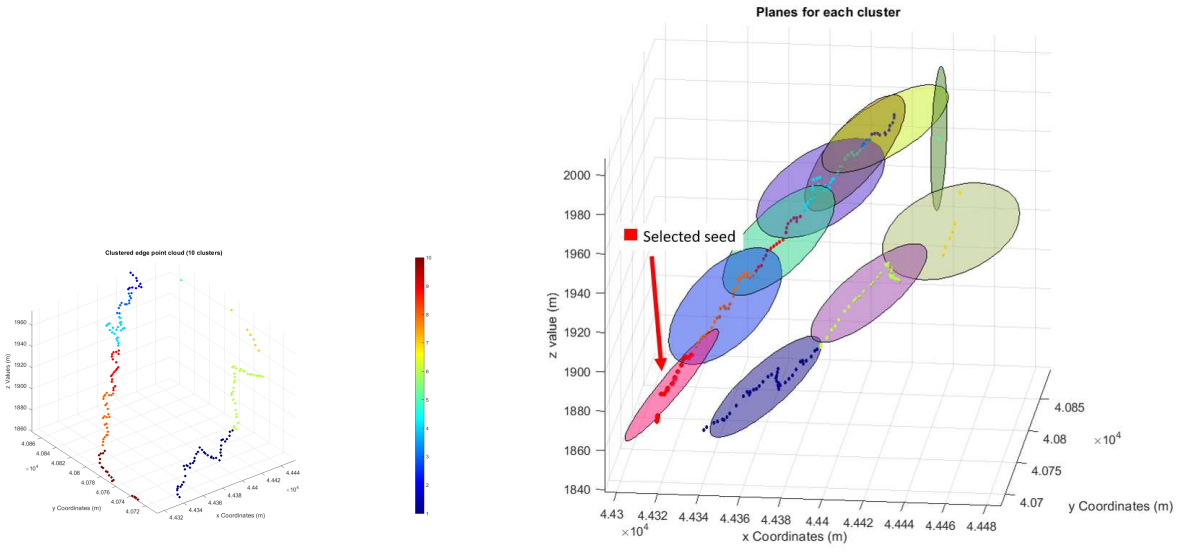

(a) (b)

Figure 51: (a) Edge point cloud k-means clustering with $k = 10$ (b) Plane fitting for each cluster highlighting the selected seed.

5.2.4 Iterative plane fitting results

The iterative plane fitting algorithm initiated with the selected seed highlighted in Figure 51b, gave as outputs four planes. The results are shown in Figure 52 where the red points are the final consensus for each main cycle that were used to fit the planes defined by the eigenvectors $\hat{\lambda_1}$, $\hat{\lambda_2}$ and $\hat{\lambda_3}$ (normal) displayed in red, blue and black vectors, respectively, with an amplitude corresponding to each final tolerance (ϵ). As in the Cumba case, the dip vector is displayed in cyan. The values of the dip angle, dip direction, and number of iterations for each plane are shown in Table 4

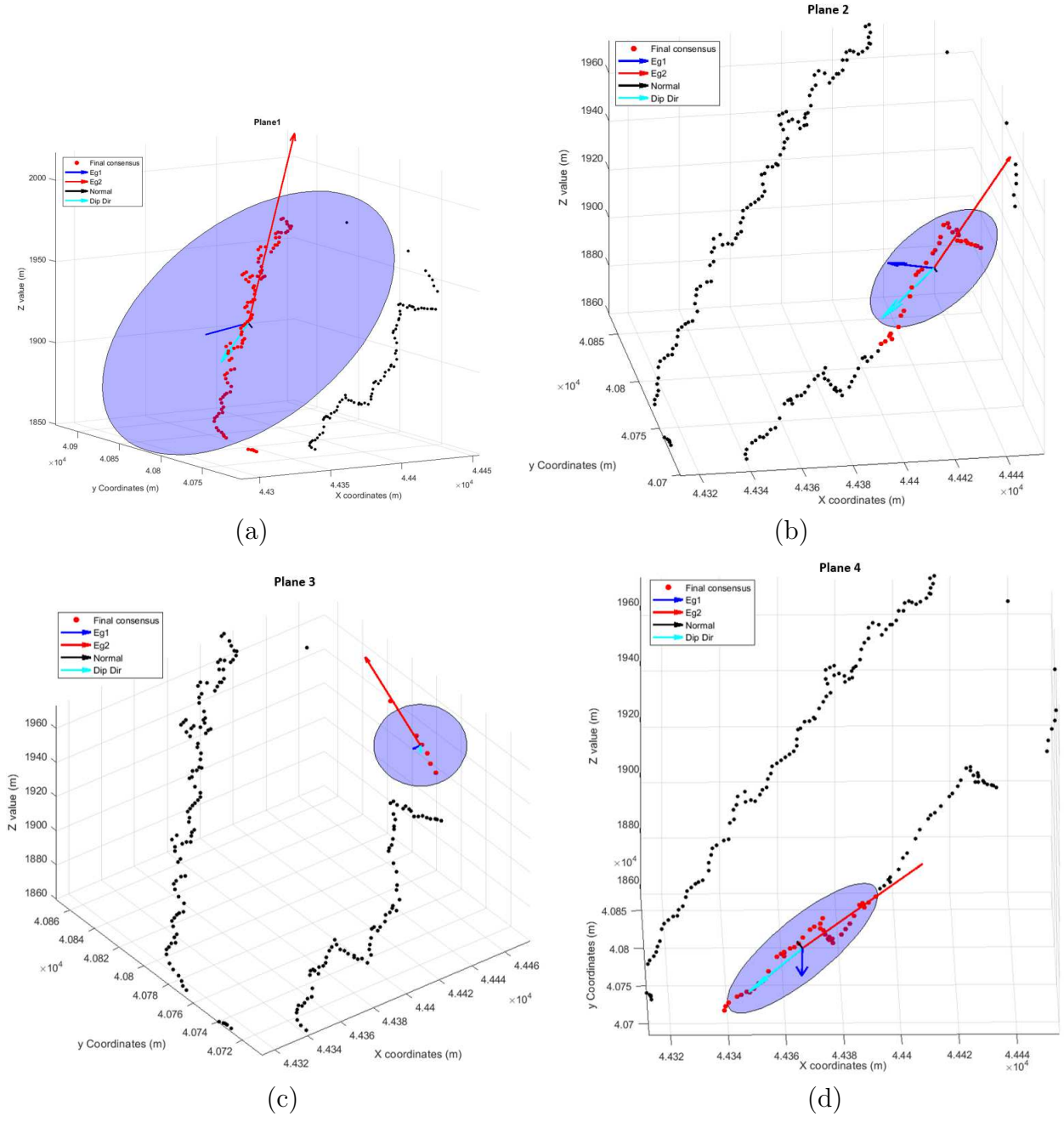

Figure 52: Montana iterative plane fitting results. (a) Plane 1, (b) Plane 2, (c) Plane 3 and (c) Plane 4.

Plane	Dip angle	Dip direction	Iterations
Plane 1	44°	258°	11
Plane 2	38°	255°	4
Plane 3	27°	216°	3
Plane 4	38°	261°	3

Table 4: Planes structural information

The extracted planes were displayed in the software Guardian from IDSGeoradar:

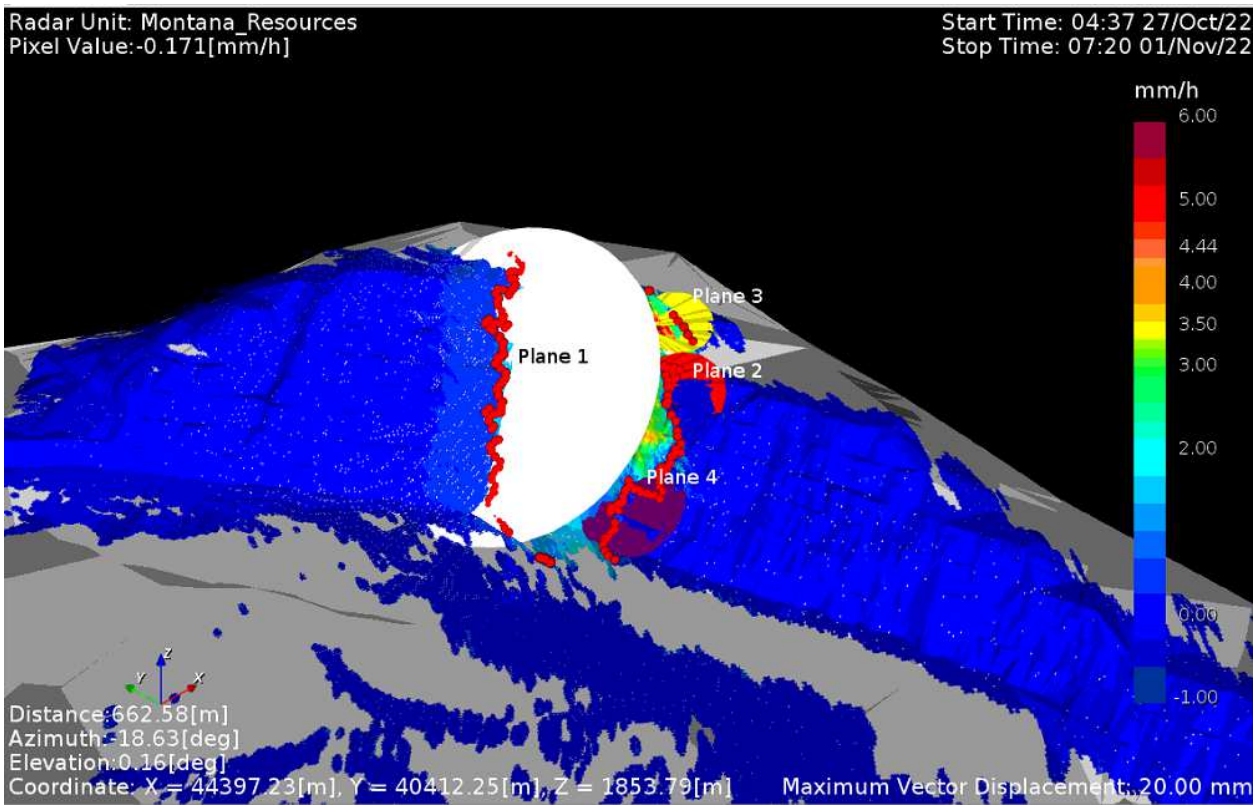

(a)

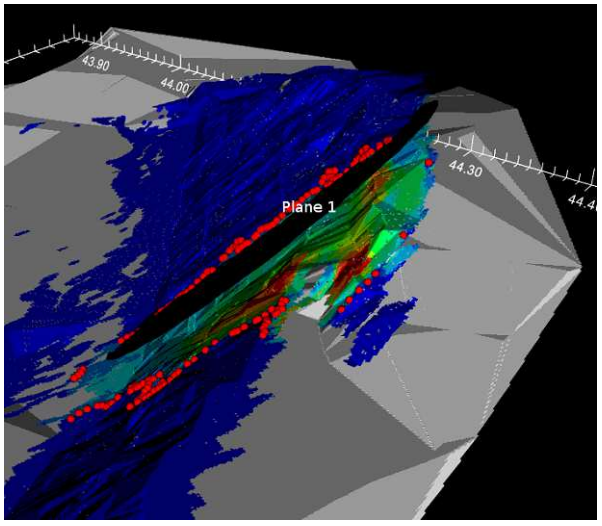

(b)

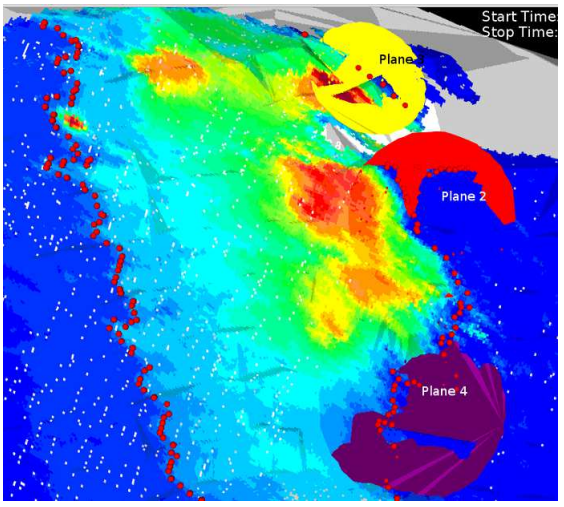

(c)

Figure 53: Montana iterative plane fitting results displayed in Guardian. (a) View of all the extracted planes (b) Zoom of Plane 1, (c) Zoom of plane 2, 3, and 4. Planes overlayed on the raw velocity map. Positive velocity values are approaching the sensor.

6 Discussion

6.1 Cumba slope failure

Comparing the directions of the resultant planes (Table 3) with the planes extracted using medium-resolution (Bar et al. 2023) photogrammetry (PH) (Table 2), it can be suggested that Plane 1 and Plane 2, extracted using the iterative plane fitting algorithm (IPF), have a good fit considering the fault 190916-b (Black) and 190923-a (Blue) in Figure 33. In the case of Plane 2, its angle differences from the PH plane, even have lower values than the results provided by Cawood et al. (2017) where the comparison between LiDAR and the planes measured using compass-clinometer, resulted in a maximum deviation of 5° from the principal direction. Moreover, Plane 1 angle differences from the PH planes, are smaller than the ones of the planes derived from ASfM in Cawood et al. (2017), which have a maximum deviation of 42° from the control planes.

Plane	**Dip**	**Dip direction**
Plane 1	66°	244°
190916-b (Black)	82°	259°
Difference	16°	15°
Plane 2	39°	211°
190923-a (Blue)	42°	215°
Difference	3°	4°

Table 5: Planes modeled with IPF (Plane 1 and Plane 2) and with PH (Black and Blue).

To visualize graphically the difference between the two modeling methods these planes were displayed in Guardian, comparing Plane 1 with the 190916-b (Black) plane, and Plane 2 with the 190923-a (Blue) plane:

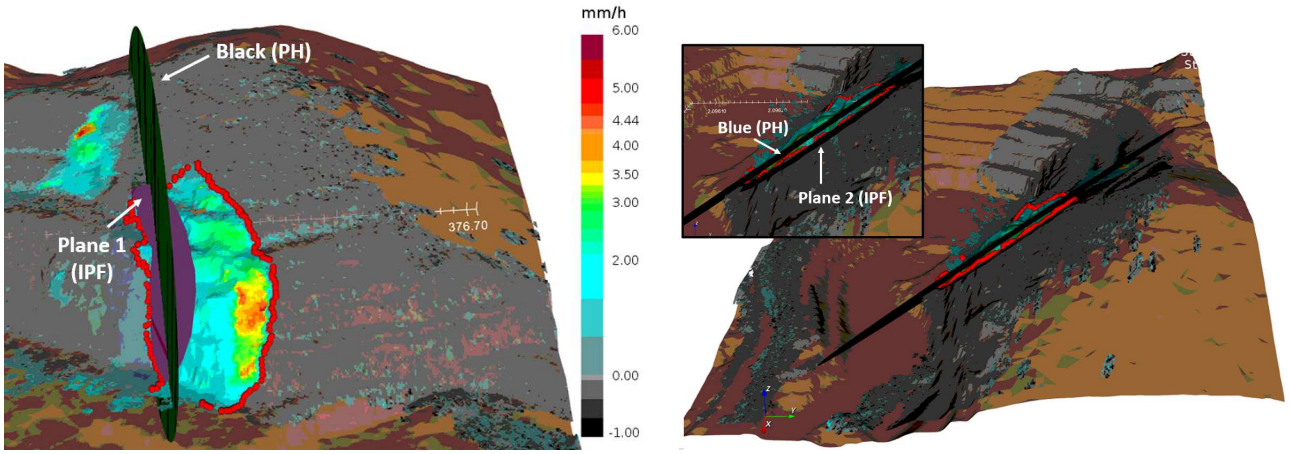

(a) (b)

Figure 54: Plane comparison in Guardian displaying the velocity map (positive values are approaching the sensor). (a) Plane 1 (IPF) and Black plane (PH). (b) Plane 2 (IPF) and Blue plane (PH).

The obtained results allow us to state that the extracted planes using IPF are a good match for the planes using photogrammetry. However, according to the analysis done by the geotechnical team of the Cumba mine detailed in chapter 5.1, from the two planes that were involved in the failure deformation, the IPF algorithm was able to detect only one, the blue plane (PH) as Plane 2 (IPF), where the main displacement occurred according to the modeled deformation. Nevertheless, some considerations must be made to analyze why by using IPF only the blue plane was extracted, and the difference between the two methods. The first consideration is that the radar images used as input for the IPF were acquired on dates posterior to the failure event, while the planes extracted with PH were modeled using aerial photos dated before the failure. Thus, the displacement of the event recorded in the velocity map of Figure 39d indicates the instability of the slope after the main failure, and since the stress conditions vary after the main deformation, it is likely that the structures in which the displacement occur also varied. This possibly explains why the velocity clustering shown in Figure 40b was limited to the Plane 1 and Plane 2 structures, and the red plane in Figure 35 was not detected and therefore not extracted using IPF.

The second consideration is related to the resolution of the photogrammetry, which had a medium resolution, the aerial photos were taken using only a nadir-looking flight with

a high altitude the resultant models can have inaccuracies with respect to the ground-truth. Therefore, the orientation and location of the modeled structures can be affected by this, which means that the difference between the modeled structures with PH and IPF can be derived from this condition. Another source of difference could be the fact that the displacement measured with ArcSAR measured only the LOS component of the real deformation vector, hence it might affect the velocity threshold clustering which is a fundamental step in the extraction of the structures with IPF. To check the validity of both methods it could be useful to take in-situ measurements of the faults, to improve the resolution of the photogrammetry, or to acquire LiDAR data. However, the difference in the measurements between the PH and IPF is small, considering the angle differences, especially in the case of the Blue plane and Plane 2, and thus a validation might not be necessary.

Finally, it is relevant to highlight that the dimension of the IPF-extracted structures is limited by the mapped deformation. Hence the length of the extracted fault planes does not represent the length of the real structure, this can be seen comparing the planes extracted with PH shown in Figure 33 and Figure 45. This means that the relevant information extracted using IPF is the orientation and location of the planes and the deformation boundaries, but not the extent of the fault surfaces.

6.2 Montana Open-pit

As in this case of study, there was no available information about the ground truth of the extracted planes, this case is used to evaluate the applicability of the IPF algorithm in diverse slope instabilities. In this pit, only Plane 1 shows a viable representation of a fault surface, as shown in Figure 52a, since this plane follows the continuous northern edge, however the dip and dip direction cannot be validated. Planes 2, 3, and 4 are discontinuous and do not represent a real surface. The extraction of these planes was problematic since the original radar data contains an area with no values in the southern boundary (Figure 55a) causing the segmentation of the edge between Plane 2 and Plane 3 (Figure 55b).

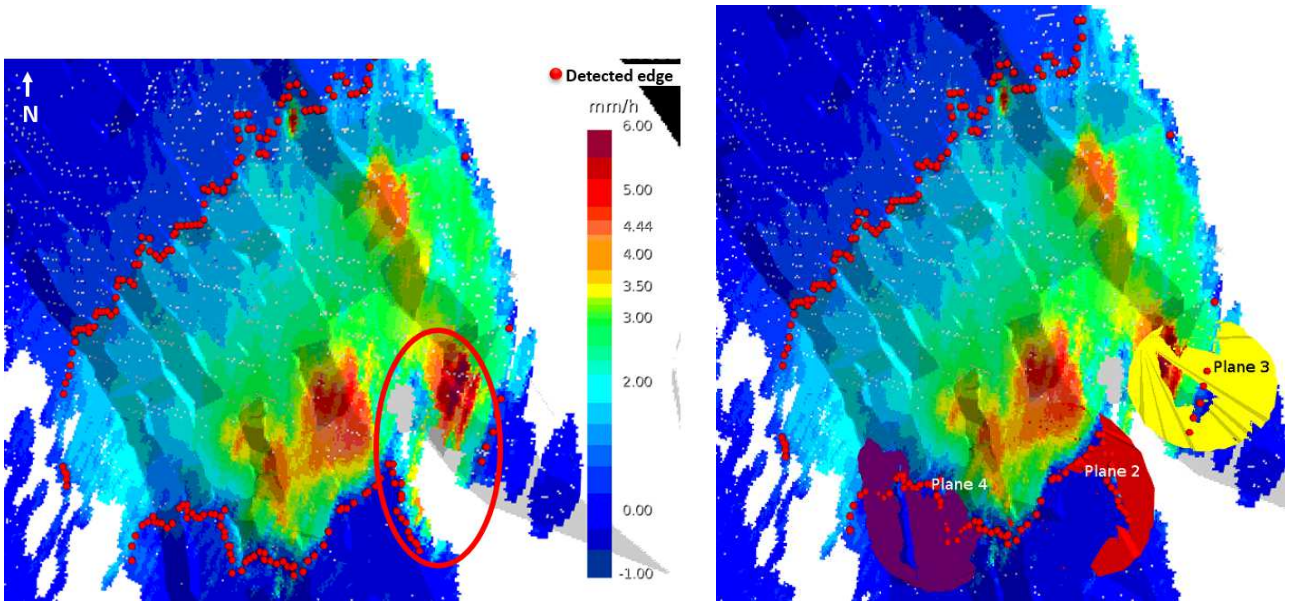

(a) (b)

Figure 55: (a) Plane view showing the gap in the southern edge with the (b) affected planes. Positive velocity values are approaching the sensor.

Moreover, Plane 2 was not able to grow in the west direction towards the points of Plane 4, where the edge was continuous. This could indicate that in this case, the tolerances (ϵ) of the iterative process for including a point in the final consensus (subchapter 4.6.2) should be reviewed since this determines the distance from the plane which will be used to include points in the final model.

Another condition that possibly affects the quality of the extracted edges is the DTM resolution and the geocoding using this DTM. In this case, the original DTM with grid format had a cell resolution of 1.5 m, nevertheless the width of the benches can have values close to the cell resolution, according to the measurements made on the DTM using Guardian (Figure 56).

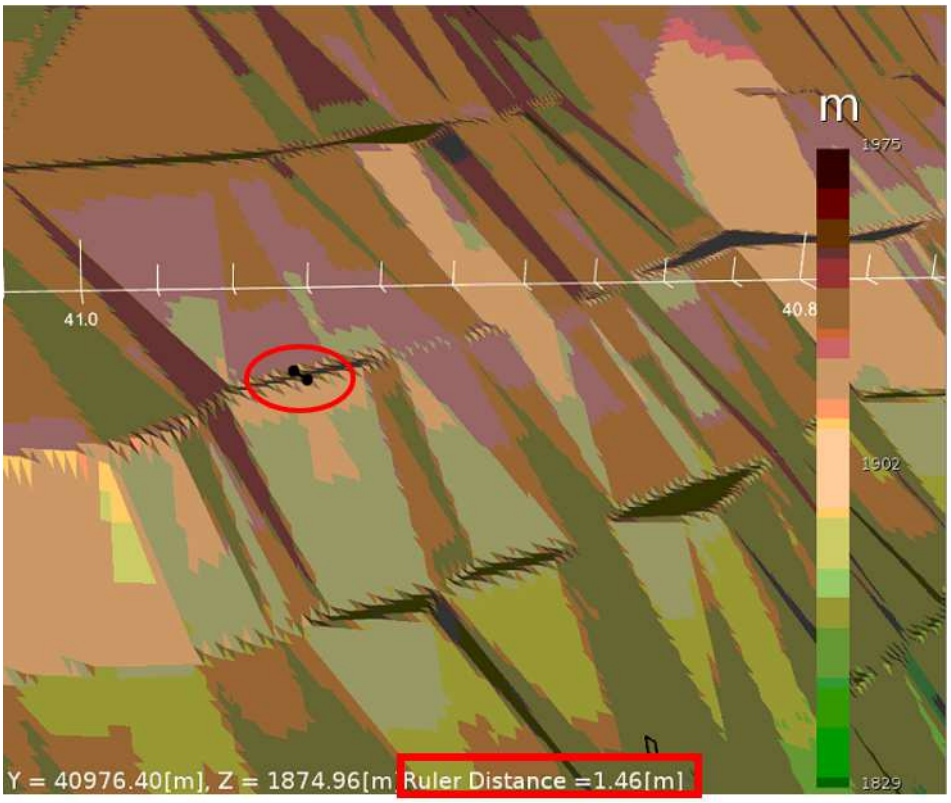

Figure 56: Bench width measurement on the DTM (color bar is the height according to the reference level) using Guardian.

This means that the original DTM resolution is not appropriate for structure extraction since it has a low resolution considering the pit design, since this would also represent a low resolution in the triangulated mesh used in the geocoding process, resulting in a wrong positioning of the edge 3D point cloud and therefore a wrong extraction of the modeled planes. Besides the DTM resolution, the geocoding seems to be affected by other factors, this can be seen in Figure 57 by comparing the geometry of the deformation shown in the velocity map (red lines) and the pit bench faces bench floors (yellow lines) geometry.

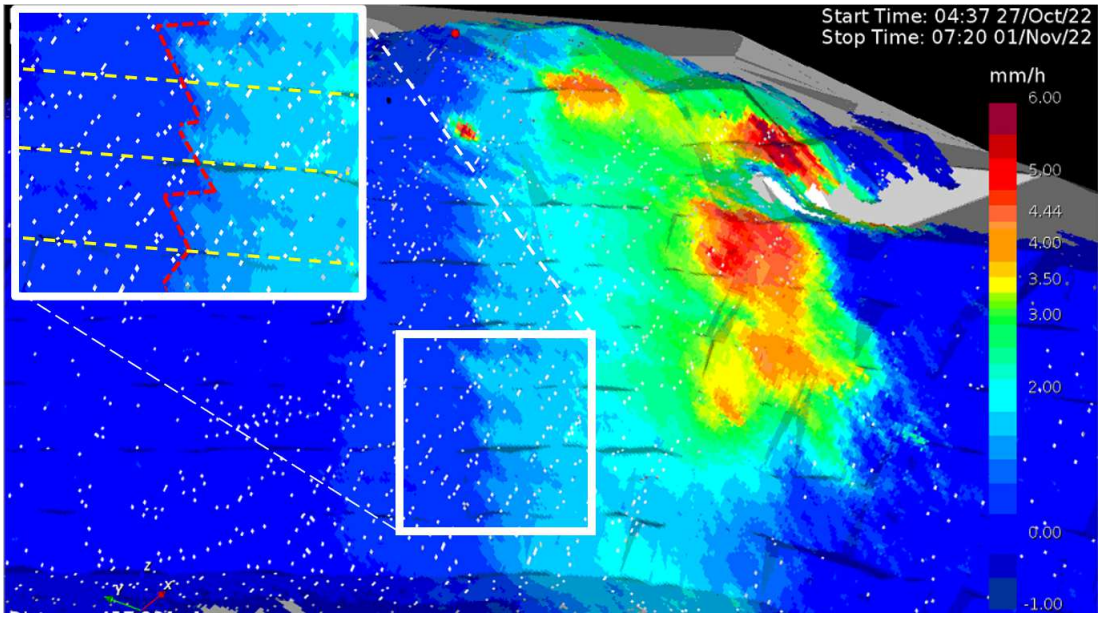

Figure 57: Geocoding detailing the bench floors (yellow dotted line) and the deformation geometry (red dotted line). Positive velocity values are approaching the sensor.

The vertical red lines in Figure 57 "cut" the floor of the benches, in yellow, this means that the geocoding of the velocity map does not represent the right geometry of the deformation on the DTM, since the horizontal red lines should overlap the bench floor lines in the DTM. Using this information it can be stated that none of the extracted fault planes using the IPF algorithm can be used for the characterization of the slope instability or to perform a kinematic analysis since the input data does not have the right resolution and spatial correctness, and therefore the extracted planes would not be a proper representation of the geological structures involved in the slope displacement.

7 Conclusions

The design and modifications of the proposed iterative plane fitting algorithm (IPF), based on the RANSAC method, have proven to be effective in modeling planes that have a geological nature and therefore have special considerations regarding the direction and inclination (dip direction and dip) of the expected planes with respect to the topography. Typical plane fitting algorithms do not take into account these spatial constraints and hence are not always appropriate to extract geological structures. The accuracy of this method has been proven by comparing the planes extracted with IPF and the planes modeled with photogrammetry, showing a small error between the two methods. Additionally, in the two cases of study, the algorithm was able to find converging planes in less than 20 iterations showing good efficiency and thus a suitable potential for a near real-time application during the slope monitoring stage, where the extracted planes could be a relevant input for the mass movement characterization and specially for the stability analysis.

The main contribution of this study was the IFP algorithm for modeling geological structures involved in slope instability. However, another important contribution was the development of the velocity threshold clustering which by itself is a relevant input in the description of a slope instability. To obtain a velocity threshold that clusters the unstable area, using a quantitative process with mathematical considerations is a great advance in the analysis of the GB-SAR data since the delimitation of the unstable area is usually done manually using the display of the velocity or displacement maps, and therefore it depends on the user considerations and even on the color scale used on the graphical representation. With the proposed method the unstable area delimitation is more precise and does not depend on human interpretation. Also, the numerical output of the velocity threshold can be useful for early warning systems by defining the unstable and stable pixels.

Moreover, the limitations of the proposed algorithm are mostly related to the input data, as shown in one of the study cases. Extracting realistic planes from the velocity map depends on the resolution of the DTM, the accuracy of the geocoding, and the

noise on the differential phase map. However, other analyses must be done to determine the applicability of this method, for instance, to establish if it is relevant for other types of failure modes such as toppling or circular mechanisms, and to test its validity on different slope movement geometries according to their morphometric parameters (area, length, width, aspect ratio, slope angle). Another proposed future work is the development of more robust methods for choosing the multiple parameters of the algorithm, for example, the k number of clusters on the edge segmentation and the error tolerances coefficients (ϵ) to add a point to the plane consensus. This could be done by adding a third iterative cycle to test multiple plane models.

It is important to mention that in every slope instability study, multiple methods must be used to improve the precision of the risk management plan. An output of a single method should not be used as a unique estimation of this geological hazard, especially pondering the important implications of a failure event. Therefore, the planes extracted using the proposed algorithm must be considered as one input for the risk analysis that must be supported by other methods, and as GB-SAR is usually used during monitoring, they would be part of the iterative process of the slope instability risk management where, as shown in Figure 1, the outputs obtained during the monitoring stage are used as feedback for the hazard identification and the risk estimation steps. Therefore these planes would be useful to provide a successful risk management to mitigate a potential slope failure event.

References

Abramson, Lee W et al. (2001). *Slope stability and stabilization methods*. John Wiley & Sons.

Adrien Leygue (Dec. 4, 2014). *Plane fit*. Version 1.1.0.0. URL: https://www.mathworks.com/matlabcentral/fileexchange/43305-plane-fit),%20MATLAB%20Central%20File%20Exchange.

Alptekin, Aydın and Murat Yakar (2022). "Software used to extract discontinuity sets from point clouds". In: *Advanced Engineering Days (AED)* 2, pp. 107–109.

Altiti, Awwad H, Rami O Alrawashdeh, and Hani M Alnawafleh (2021). "Open pit mining". In: *Mining Techniques—Past, Present and Future,*

Australian Geomechanics Society (2002). "Landslide risk management concepts and guidelines". In: *Australian Geomechanics: Journal and News of the Australian Geomechanics Society* 37.2, pp. 1–44.

Bar, N et al. (2023). "A geotechnical evaluation of the Cumba Pit Slope Failure, Dominican Republic". In: *IOP Conference Series: Earth and Environmental Science*. Vol. 1124. 1. IOP Publishing, p. 012009.

Battulwar, Rushikesh et al. (2021). "A state-of-the-art review of automated extraction of rock mass discontinuity characteristics using three-dimensional surface models". In: *Journal of Rock Mechanics and Geotechnical Engineering* 13.4, pp. 920–936.

Benjamin Kraus (May 28, 2013). *nanconv*. Version 1.1.0.0. URL: https://it.mathworks.com/matlabcentral/fileexchange/41961-nanconv),%20MATLAB%20Central%20File%20Exchange.

Bruder, J et al. (2003). "IEEE standard for letter designations for radar-frequency bands". In: *IEEE Aerospace & Electronic Systems Society*, pp. 1–3.

Bunn, Michael, Ben Leshchinsky, and Michael J Olsen (2020). "Estimates of three-dimensional rupture surface geometry of deep-seated landslides using landslide inventories and high-resolution topographic data". In: *Geomorphology* 367, p. 107332.

Burger, Wilhelm and Mark J Burge (2022). "Edge-preserving smoothing filters". In: *Digital Image Processing: An Algorithmic Introduction*. Springer, pp. 497–536.

Buyer, Andreas and Wulf Schubert (2017). "Calculation the spacing of discontinuities from 3D point clouds". In: *Procedia engineering* 191, pp. 270–278.

Casagli, Nicola et al. (2023). "Landslide detection, monitoring and prediction with remote-sensing techniques". In: *Nature Reviews Earth & Environment* 4.1, pp. 51–64.

Cawood, Adam J et al. (2017). "LiDAR, UAV or compass-clinometer? Accuracy, coverage and the effects on structural models". In: *Journal of structural geology* 98, pp. 67–82.

Chale, Antonin, Michel Joboyedoff, and Marc-Henri Derron (2023). "A new approach to a Semi-automatic discontinuity sets extraction from point clouds." In: *EGU General Assembly Conference Abstracts*, EGU–12266.

Chao, Baotian et al. (2019). "An Overview of Atmospheric Correction for GB-SAR". In: *2019 IEEE 19th International Conference on Communication Technology (ICCT)*, pp. 1062–1072. DOI: 10.1109/ICCT46805.2019.8947295.

Chen, Jiayao et al. (2023). "A critical review of automated extraction of rock mass parameters using 3D point cloud data". In: *Intelligent Transportation Infrastructure*, liad005.

CRED, Centre for Research on the Epidemiology of Disasters (2023a). *2022 Disasters in numbers*. Retrieved October 24, 2023, https://cred.be/sites/default/files/2022_EMDAT_report.pdf.

— (2023b). *Emergency Events Database (EM-DAT)*. Retrieved June 21, 2023, https://www.emdat.be/database.

Cruden, David M and David J Varnes (1996). "Landslides: investigation and mitigation. Chapter 3-Landslide types and processes". In: *Transportation research board special report* 247.

Dewitte, O and A Demoulin (2005). "Morphometry and kinematics of landslides inferred from precise DTMs in West Belgium". In: *Natural Hazards and Earth System Sciences* 5.2, pp. 259–265.

Ferrero, Anna Maria et al. (2009). "Advanced geostructural survey methods applied to rock mass characterization". In: *Rock mechanics and rock engineering* 42, pp. 631–665.

Fischler, Martin A and Robert C Bolles (1981). "Random sample consensus: a paradigm for model fitting with applications to image analysis and automated cartography". In: *Communications of the ACM* 24.6, pp. 381–395.

Gigli, Giovanni and Nicola Casagli (2011). "Semi-automatic extraction of rock mass structural data from high resolution LIDAR point clouds". In: *International Journal of Rock Mechanics and Mining Sciences* 48.2, pp. 187–198. ISSN: 1365-1609. DOI: https://doi.org/10.1016/j.ijrmms.2010.11.009. URL: https://www.sciencedirect.com/science/article/pii/S136516091000211X.

Glade, Thomas (2003). "Vulnerability assessment in landslide risk analysis". In: *Erde* 134.2, pp. 123–146.

Glade, Thomas, Malcolm G Anderson, and Michael J Crozier (2005). *Landslide hazard and risk*. Vol. 807. Wiley Online Library.

Glastonbury, James (2002). "The pre-and post-failure deformation behaviour of rock slopes". PhD thesis. UNSW Sydney.

Hu, Xie et al. (2020). "Four-dimensional surface motions of the Slumgullion landslide and quantification of hydrometeorological forcing". In: *Nature Communications* 11.1, p. 2792.

Jaboyedoff, Michel et al. (2020). "A review of methods used to estimate initial landslide failure surface depths and volumes". In: *Engineering Geology* 267, p. 105478.

Jakob, Matthias (2022). "Landslides in a changing climate". In: *Landslide hazards, risks, and disasters*. Elsevier, pp. 505–579.

Kong, Deheng, Faquan Wu, and Charalampos Saroglou (2020). "Automatic identification and characterization of discontinuities in rock masses from 3D point clouds". In: *Engineering Geology* 265, p. 105442. ISSN: 0013-7952. DOI: https://doi.org/10.1016/j.enggeo.2019.105442. URL: https://www.sciencedirect.com/science/article/pii/S0013795219305848.

Lato, Matthew J. and Malte Vöge (2012). "Automated mapping of rock discontinuities in 3D lidar and photogrammetry models". In: *International Journal of Rock Mechanics and Mining Sciences* 54, pp. 150–158. ISSN: 1365-1609. DOI: https://doi.org/10.1016/j.ijrmms.2012.06.003. URL: https://www.sciencedirect.com/science/article/pii/S1365160912001207.

Libert, Ludivine, Jan Wuite, and Thomas Nagler (2022). "Automatic delineation of cracks with Sentinel-1 interferometry for monitoring ice shelf damage and calving". In: *The Cryosphere* 16.4, pp. 1523–1542.

Lloyd, Stuart (1982). "Least squares quantization in PCM". In: *IEEE transactions on information theory* 28.2, pp. 129–137.

Long, David and Fawwaz Ulaby (2015). *Microwave radar and radiometric remote sensing*. Artech.

Macciotta, Renato and Michael T Hendry (2021). "Remote sensing applications for landslide monitoring and investigation in western Canada". In: *Remote Sensing* 13.3, p. 366.

Martha, Tapas R et al. (2010). "Characterising spectral, spatial and morphometric properties of landslides for semi-automatic detection using object-oriented methods". In: *Geomorphology* 116.1-2, pp. 24–36.

Mei, Shaohui et al. (2020). "Spatial and spectral joint super-resolution using convolutional neural network". In: *IEEE Transactions on Geoscience and Remote Sensing* 58.7, pp. 4590–4603.

Mercer, KG (2006). "Investigation into time dependent behavior and failure mechanism of unsupported rock slopes based on the interpretation of observed deformation behavior". PhD thesis. PhD Thesis, Faculty of Eng., Univ. of Witwatersrand, SA.

Metternicht, Graciela, Lorenz Hurni, and Radu Gogu (2005). "Remote sensing of landslides: An analysis of the potential contribution to geo-spatial systems for hazard assessment in mountainous environments". In: *Remote Sensing of Environment* 98.2, pp. 284–303. ISSN: 0034-4257. DOI: https://doi.org/10.1016/j.rse.2005.08.004. URL: https://www.sciencedirect.com/science/article/pii/S0034425705002506.

Minerals, Department of and Energy (2018). Mine Health and Safety Inspectorate, pp. 1–1.

Monserrat, O, M Crosetto, and G Luzi (2014). "A review of ground-based SAR interferometry for deformation measurement". In: *ISPRS Journal of Photogrammetry and Remote Sensing* 93, pp. 40–48.

Moreira, Alberto et al. (2013). "A tutorial on synthetic aperture radar". In: *IEEE Geoscience and remote sensing magazine* 1.1, pp. 6–43.

Nichol, Janet E., Ahmed Shaker, and Man-Sing Wong (2006). "Application of high-resolution stereo satellite images to detailed landslide hazard assessment". In: *Geomorphology* 76.1, pp. 68–75. ISSN: 0169-555X. DOI: https://doi.org/10.1016/j.geomorph.2005.10.001. URL: https://www.sciencedirect.com/science/article/pii/S0169555X05003223.

Nikolaeva, Elena et al. (2014). "Landslide observation and volume estimation in central Georgia based on L-band InSAR". In: *Natural Hazards and Earth System Sciences* 14.3, pp. 675–688.

Norrish, Norman I and Duncan C Wyllie (1996). "Landslides: Investigation and Mitigation. Chapter 15-Rock slope stability analysis". In: *Transportation Research Board Special Report* 247.

Parise, Mario and Randall W Jibson (2000). "A seismic landslide susceptibility rating of geologic units based on analysis of characteristics of landslides triggered by the 17 January, 1994 Northridge, California earthquake". In: *Engineering geology* 58.3-4, pp. 251–270.

Partnerships, ISDR-ICL Sendai Landslide (2021). *Partnerships 2015-2025 for Global Promotion of Understanding and Reducing Landslide Disaster Risk*.

Peek, Kenneth E. (2011). "Estimation and compensation of frequency sweep nonlinearity in FMCW radar". In: URL: https://api.semanticscholar.org/CorpusID:32528580.

Piteau, Douglas R and F Lionel Peckover (1978). "Engineering of rock slopes". In: *Landslides-Analysis and control. Nat. Acad. Sci., Washington*, pp. 192–230.

Rimmelin, R and J Vallejos (2020). "Rock mass behaviour of deep mining slopes: a conceptual model and implications". In: *Slope Stability 2020: Proceedings of the 2020 International Symposium on Slope Stability in Open Pit Mining and Civil Engineering*. Australian Centre for Geomechanics, pp. 591–608.

Roccheggiani, Matteo et al. (2018). "Automated detection of surface ruptures associated with the 2016 Central Italy earthquake sequence by Sentinel-1 SAR in-

terferometry data". In: *Proceedings of the 9th International INQUA meeting on Paleoseismology, Active Tectonics and Archeoseismology*, pp. 229–232.

Rödelsperger, Sabine (2011). "Real-time processing of ground-based synthetic aperture radar (GB-SAR) measurements". PhD thesis. Dissertation, Darmstadt, Technische Universität, 2011.

Roncella, Riccardo, Gianfranco Forlani, and Fabio Remondino (2005). "Photogrammetry for geological applications: automatic retrieval of discontinuity orientation in rock slopes". In: *Videometrics VIII*. Vol. 5665. SPIE, pp. 17–27.

Stead, Doug and Andrea Wolter (2015). "A critical review of rock slope failure mechanisms: the importance of structural geology". In: *Journal of Structural Geology* 74, pp. 1–23.

Tian, Yingying et al. (2017). "Geometrical characteristics of earthquake-induced landslides and correlations with control factors: a case study of the 2013 Minxian, Gansu, China, Mw 5.9 event". In: *Landslides* 14, pp. 1915–1927.

Tofani, Veronica et al. (2013). "Use of remote sensing for landslide studies in Europe". In: *Natural Hazards and Earth System Sciences* 13.2, pp. 299–309.

Varnes, David J (1958). "Landslide types and processes". In: *Landslides and engineering practice* 24, pp. 20–47.

— (1978). "Slope movement types and processes". In: *Special report* 176, pp. 11–33.

Voronov, Roman (2013). *nanmedfilt2 version 1.0.0.0*. URL: `https://it.mathworks.com/matlabcentral/fileexchange/41457-nanmedfilt2` (visited on 04/29/2023).

Voyat, Iris et al. (2006). "Advanced techniques for geo structural surveys in modelling fractured rock masses: application to two Alpine sites". In: *ARMA US Rock Mechanics/Geomechanics Symposium*. ARMA, ARMA–06.

Wyllie, Duncan C and Chris Mah (2004). *Rock slope engineering*. CRC Press.

Young, K, A Robotham, and G Virk (2020). "Economic consequences of geotechnical instabilities in open cut coal mines". In: *Slope Stability 2020: Proceedings of the 2020 International Symposium on Slope Stability in Open Pit Mining and Civil Engineering*. Australian Centre for Geomechanics, pp. 145–154.